Part I: Multi-valent Ion Effects on Polyelectrolyte Structure and Thermodynamics
&
Part II: Hydrodynamic Self-Propulsion

Thesis by
Alec Glisman

In Partial Fulfillment of the Requirements for the
Degree of
Doctor of Philosophy in Chemical Engineering

CALIFORNIA INSTITUTE OF TECHNOLOGY
Pasadena, California

2025
Defended July 10, 2024

Alec Glisman
ORCID: 0000–0001–9677–1958

ACKNOWLEDGEMENTS

I am indebted to many friends, family, and colleagues for their support throughout my time at Caltech. Graduate school has been a challenging and rewarding experience, and I am lucky to have shared it with so many wonderful people. I will always be grateful to my advisor, Professor Zhen-Gang Wang, for his guidance and mentorship throughout the last few years. Zhen-Gang made it a point to support me and my research, even when I was unsure of my abilities. His enthusiasm for science and research is infectious, and I am grateful to have had the opportunity to learn from him.

I would like to thank Prof. John Brady, Prof. David Tirrell, Prof. William Goddard, and Prof. Zhen-Gang Wang for serving on my thesis committee. Prof. Melany Hunt and Prof. Tim Colonius served on my candidacy committee and provided valuable feedback on my research. Their feedback and questions have helped me to improve my research and consider the broader impact of my work. A special thanks to John Brady for advising me for my first two years at Caltech. His ability to distill complex models into key physical ideas and relate them to others has amazed me in both research and the classroom.

The Chemical Engineering Department at Caltech has been a great place to learn and grow, in large part due to the faculty and staff. Dr. Michael Vicic provided many resources and opportunities to explore my interests outside of academia. Allison Kinard and Dr. Mi Kyung Kim guided me through the administrative process of graduate school and were always available to answer my questions. Suresh Guptha was instrumental in helping our group to develop and maintain our computing infrastructure.

Dow Chemical Company provided financial support for my research through a University Partnership Initiative (UPI) grant. I benefitted greatly from the project management and direction of Decai Yu and Thomas Kalantar, and I am grateful for their support and encouragement. Our experimental collaborators at Dow, Scott Backer, Eric Paul Wasserman, Christopher Tucker, Larisa Reyes, and Meng Jing provided valuable real world context for our simulations and were always available to answer my questions.

I would like to thank all past and present members of the Brady group for helping me to start my graduate career on the right foot. Dr. Camilla Kjeldbjerg not only had great scientific ideas but always had something fun to discuss. Dr. Hyeongjoo Row and Dr. Zhiwei Peng were superb teaching assistants in my core graduate courses and contributed significantly to my academic success. Dr. Stewart Mallory and Dr. Edmond Zhou were wonderful mentors for advancing my skills in scientific computing and developing independent codebases. Most notably, I would like to thank Dr. Austin Dulaney. His support and concern kept me motivated, especially as I felt overwhelmed balancing research and coursework in my first year as a graduate student. Austin's support continued throughout my time at Caltech, and I am grateful to have had him as a friend and colleague.

The members of the Wang group welcomed me into their group and made me feel at home, even as I started working with them well into my graduate career. The postdoctoral fellows, Dr. Yasemin Basdogan, Dr. Shensheng Chen, Dr. Alejandro Gallegos, broadened my scientific horizons and provided valuable feedback on my research. I enjoyed working with Dr. Chris Balzer, Dorian Bruch, Alexandros Tsamopoulos, Benjamin Ye, Sam Varner, Pierre Walker, Jihoon Oh, and Christopher Stewart on both research and coursework. I would like to especially thank Dr. Sriteja Mantha. Sriteja is an excellent scientist and mentor who has propelled my research forward in ways I could not have imagined, and I would have been truly lost without his help. Dr. Tridip Das provided valuable feedback on my research and lent his expertise in electronic structure calculations to our work.

My former advisor, Prof. Kranthi Mandadapu at UC Berkeley, first taught me the importance of scientific rigor and the value of a good mentor. Kranthi is in many ways the reason I am in graduate school, and I am grateful for his guidance and support. Prof. Amaresh Sahu mentored me during my undergraduate research and first gave me confidence in my ability to do research.

My friends outside of the lab have been a constant source of support and encouragement, especially when research was not going well. Ravi Lal continually challenges my views of both science and the world, and living with him is one of the highlights of my time at Caltech. Ishaan Dev and his last-minute adventures have been a welcome distraction from the stress of graduate school. I greatly enjoyed Eric Tran going out of his way to come to Pasadena

and spend quality time with me. Tuesday trivia nights with Ojas Pradhan, Grace Holbrook, Benjamin Ye, and Ravi Lal were a great way to balance work and fun during the week. It was an honor to first teach transport phenomena to Sam Varner and Vignesh Bhethanabotla, and later to learn from them as they taught me about field theory and molecular dynamics. Officiating the wedding of my friends, Maria Krasilnikov and Thomas McClave, was one of the highlights of my life. Maria has been a wonderful friend and confidant throughout my time at Caltech and Berkeley. Michael Russell has been an amazing friend for the last decade, and I am grateful for his support and encouragement throughout my life. I would also like to thank Pallavi, Karan, and the entire Chadha family for their support through undergraduate and graduate school.

My family has provided me with unconditional love and a strong foundation to explore my interests. My mother and father have sacrificed immensely throughout their lives to allow me to pursue my dreams. Their support throughout my life is the reason I am where I am today, and for that I am forever grateful. My sister, Hannah, has kept me grounded and provided a much-needed perspective on life outside of graduate school. I am proud of her accomplishments and look forward to seeing what she does next. Elizabeth Panora welcomed me into her family with open arms, and I could not have asked for a kinder or more supportive mother-in-law.

My fiancée, Kayla Panora has been my rock throughout graduate school. She has supported me through the ups and downs of graduate school and has always been there to listen to my frustrations and celebrate my successes, no matter how small. Kayla brings incredible amounts of love and joy into my life, even waving bye to me every morning as I leave for work. I will never be able to thank her enough for her love and support.

I am grateful for those listed above and so many others throughout my life.

ABSTRACT

Part I: Polyelectrolytes are a class of charged polymers that have found widespread utility in water treatment, drug delivery, and scale inhibition, among other applications. For many of these applications, it is crucial to control the phase stability of the polyelectrolyte solution. The long-ranged nature of the electrostatic interactions in polyelectrolyte solutions and the polyelectrolyte's connectivity lead to a rich phase behavior that can be challenging to study, especially in the presence of other ions or surfaces. In scale inhibition applications, polyelectrolytes such as poly(acrylic acid) (PAA) are used to prevent the dissolution of sparingly soluble salts, such as calcium carbonate, in water. While the significant influence of small ions on polyelectrolyte solution phase behavior is recognized, the precise molecular mechanisms driving the resulting phase stability remain largely elusive.

Polyelectrolyte theory suggests that a polyelectrolyte's behavior and adsorption properties in solution are strongly tied to the polymer chain conformation and charge distribution, which in turn is influenced by solution ionic strength and ionic valency. Consequently, we expect the polyelectrolyte performance to be highly dependent on the solution conditions and the molecular features of the polyelectrolyte. Previous computational studies have studied general polyelectrolytes in solution with coarse-grained and implicit solvent models and provided insights into the chain conformational transitions. However, they disagree on the mechanisms underlying aqueous polyelectrolytes salting out of suspension and are unable to yield chemically specific insights. We seek to better understand the antiscalant mechanisms of polyelectrolytes using all-atom molecular dynamics to capture solvation and polymer chemistry effects on the mechanisms of polyelectrolytes preventing scale nucleation and slowing growth.

The current work investigates the structure and thermodynamics of polyelectrolytes in bulk solution and at crystalline interfaces with added multi-valent ions. The presence of multi-valent ions, such as Ca^{2+}, can significantly influence polyelectrolyte conformation via ion bridging non-neighboring charged monomers as well as screening the electrostatic interactions. We employ all-atom molecular dynamics simulations to investigate the binding modes of Ca^{2+} onto a PAA chain, Ca^{2+}–PAA complex aqueous stability, and PAA adsorp-

tion onto a crystalline $CaCO_3$ surface. In each of these cases, we find that the balance between ion bridging, electrostatic screening, and water-mediated interactions plays a crucial role in determining the polyelectrolyte's behavior in solution and at an interface.

Part II: Active bodies undergo self-propulsive motion in a fluid medium and span a broad range of length and time scales. Many active systems spontaneously self-organize into visually striking structures: fish schooling, birds flocking, and bacterial colonies growing. Current models of this emergent behavior in the inertial regime are mainly phenomenological and lack consideration of the fluid-mediated interactions between bodies.

To address this limitation, we seek to advance physics-based models of swimmers by explicitly incorporating the fluid mechanical interactions between bodies. We aim to discern the fluid medium's role in group dynamics and determine whether it can reproduce the observed emergent phenomenon without resorting to phenomenologically based interaction rules. To that end, we focus specifically on swimming in high Reynolds number flows, where inertial forces dominate, and draw comparisons to the well-studied low Reynolds number (Stokes) regime. We begin by deriving the equations of motion for a collection of unconstrained spherical particles in potential flow and extend the model to include viscous dissipation and rigid body motion constraints for many bodies with arbitrary kinematics.

We then consider the case of a single swimmer consisting of three linked spheres in potential flow. Through this, we find self-propulsion without needing external forces or momentum transfer via vortex shedding. We compare the inertial swimmer to an identical swimmer in the Stokes regime—where fluid inertia is neglected—and find that the structure of the equations of motion is identical in both flow regimes. Notably, the Stokes hydrodynamics are longer-ranged at leading order, leading to a more significant net displacement of the swimmer after one period of articulation. Finally, our study provides analytical insight into the swimming of a deformable body through an expansion of the non-linear spatial dependence of the hydrodynamic interactions.

PUBLISHED CONTENT AND CONTRIBUTIONS

1. Glisman, A. *et al.* Adsorption isotherm and mechanism of Ca^{2+} binding to polyelectrolyte. *Langmuir* **40,** 6212–6219 (2024). https://doi.org/10.1021/acs.langmuir.3c03640
2. Glisman, A. *et al.* Binding modes and water-mediation of polyelectrolyte adsorption to a neutral surface. *Manuscript in Preparation* (2024).
3. Glisman, A. *et al.* Multi-valent ion-mediated polyelectrolyte association and structure. *Macromolecules* **57,** 1941–1949 (2024). https://doi.org/10.1021/acs.macromol.3c02437
4. Glisman, A. & Brady, J. F. Swimming in potential flow. *Journal of Fluid Mechanics* **962,** 11. https://doi.org/10.1017/jfm.2022.946 (Nov. 2022).

In each of the above, A.G. participated in the conception of the project, conducted calculations, analyzed data, and participated in the writing of the manuscript.

TABLE OF CONTENTS

LIST OF ILLUSTRATIONS

LIST OF TABLES

Part I

Multi-valent Ion Effects on Polyelectrolyte Structure and Thermodynamics

Chapter 1

INTRODUCTION

This introductory chapter provides an overview of polyelectrolytes, their application in mineralization, and open questions related to multi-valent ion and polyelectrolyte interactions. The subsequent chapters present our molecular dynamics simulations of polyelectrolyte solutions in an aqueous bulk and at crystalline interfaces to understand the various molecular mechanisms through which polyelectrolytes influence mineralization.

This chapter includes content from our previously published articles:

1. Glisman, A. *et al.* Adsorption isotherm and mechanism of Ca^{2+} binding to polyelectrolyte. *Langmuir* **40,** 6212–6219 (2024).
2. Glisman, A. *et al.* Multi-valent ion-mediated polyelectrolyte association and structure. *Macromolecules* **57,** 1941–1949 (2024).
3. Glisman, A. *et al.* Binding modes and water-mediation of polyelectrolyte adsorption to a neutral surface. *Manuscript in Preparation* (2024).

1.1 Polyelectrolyte Structure and Thermodynamics

Polyelectrolytes (PEs) are a class of charged polymers that have found widespread utility in diverse fields, including water treatment [1], drug delivery [2], and scale ($CaCO_3$) inhibition [3, 4], among others. For many of these applications, controlling the phase behavior of an aqueous polyelectrolyte solution is crucial for achieving the desired functionality. These polymers are both intriguing and challenging to study due to their complex topology, charge density, and the strong electrostatic interactions that govern their structure and dynamics. This complexity makes property prediction and design difficult [5–8].

In solution, a single polyelectrolyte chain exhibits an extended conformation due to electrostatic repulsion between its charged monomers, in contrast to the Gaussian conformation of a neutral polymer chain [8, 9]. The addition of salt to the solution screens these electrostatic interactions, resulting in a more compact conformation, as illustrated in Figure 1.1.

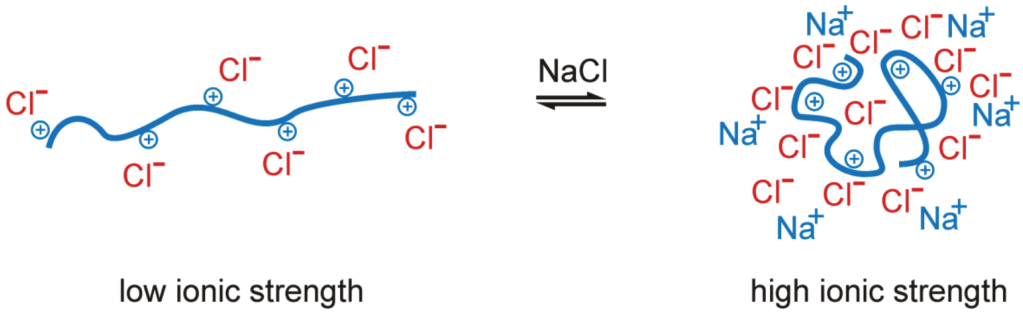

Figure 1.1: The conformation of a polyelectrolyte chain in aqueous solution without added salt (left) and with high ionic strength (right). Reproduced from Gensel [10].

The long-ranged nature of the electrostatic interactions in polyelectrolyte solutions leads to a rich phase behavior, including the formation of polyelectrolyte–ion precipitates, complex coacervates, and gels [11–15]. Additional interactions, such as hydrogen bonding, adsorption of small ions, and solvation effects, further complicate the conformations of polyelectrolytes [8], as shown in Figure 1.2. This complexity makes it challenging to predict the behavior of polyelectrolytes in solution, especially in the presence of other ions or surfaces. However, the multi-faceted behavior of polyelectrolytes yields many design opportunities via the manipulation of multiple solution conditions, such as pH and ionic strength in addition to polyelectrolyte chemistry, to tailor the properties of the polyelectrolyte solution.

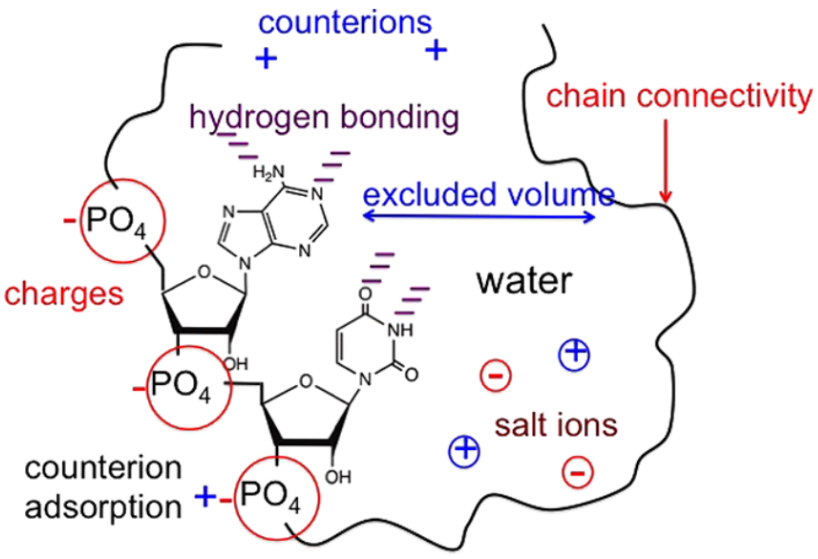

Figure 1.2: Sketch of a sample polyelectrolyte: ribonucleic acid (RNA). Chain connectivity, charges on the polymer, counterions, salt ions, excluded volume effects, hydrogen bonding, and structure of water contribute to the structures and functions of such polyelectrolytes. Reproduced from Muthukumar [8].

1.2 Polyelectrolyte Effects on Mineralization

The precipitation of sparingly soluble salts, such as calcium carbonate ($CaCO_3$), is a common problem in industrial processes, and biological systems [3, 16–22]. The ion pairs (Ca^{2+} and $CO_3{}^{2-}$) readily associate, precipitate out of solution, and form solid deposits (scale). Scale formation presents challenges to residential and industrial piping systems, restricting the fluid flow and fouling components [23–25].

Polyelectrolytes, such as poly(acrylic acid) (PAA), are commonly employed to mitigate scale formation [16, 26–29]. Although it is not fully understood what makes an effective antiscalant polyelectrolyte, a few mechanisms for scale prevention have been proposed: (1) chelation of Ca^{2+} ions from solution, (2) modification of crystal growth by preferential adsorption of polyelectrolyte to certain crystal surfaces, (3) passivation of the crystal surface by preferential adsorption of polyelectrolyte, and (4) interparticle crystal repulsion by preferential adsorption of polyelectrolyte to the crystal surface [30], as shown in Figure 1.3.

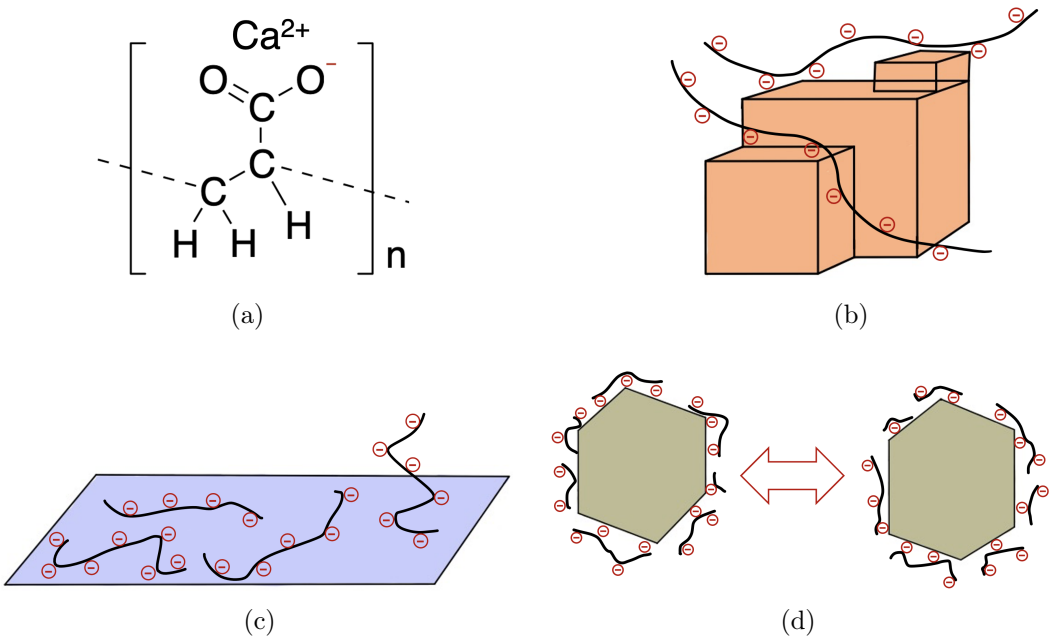

Figure 1.3: Four mechanisms by which polyelectrolytes may inhibit $CaCO_3$ crystallization. (a) Chelation of Ca^{2+} ions from solution. (b) Modification of crystal growth by preferential adsorption of polyelectrolyte to certain crystal surfaces. (c) Passivation of the crystal surface by preferential adsorption of polyelectrolyte. (d) Interparticle crystal repulsion by preferential adsorption of polyelectrolyte to the crystal surface.

However, the exact mechanisms through which polyelectrolytes modify mineralization and the relative importance of each of the above pathways are not known. In particular, it is unclear how the proposed mechanisms may be affected by the molecular features of the polymer and corresponding solution conditions. Polyelectrolyte theory suggests that a polyelectrolyte's behavior and adsorption properties in solution are strongly tied to the polymer chain conformation and charge distribution, which in turn is influenced by solution ionic strength and valency [7, 8, 11, 31–37]. However, the charge and size of a polymer are strongly influenced by the solution pH and salt concentration [34]. Consequently, we anticipate that the microscopic environment, and hence the molecular features of the polyelectrolyte, strongly dictate the polyelectrolyte's role in $CaCO_3$ mitigation.

As we are interested in understanding the molecular principles that govern the interaction between polyelectrolytes and Ca^{2+} ions, we employ all-atom molecular dynamics (MD) simulations to investigate the chelation of Ca^{2+}

ions by polyelectrolytes in solution and the adsorption of polyelectrolytes on crystalline surfaces. MD simulations provide a unique opportunity to study molecular-level interactions with chemical specificity, which are challenging to probe experimentally. In the following sections, we will discuss the current understanding of polyelectrolyte–ion interactions and the adsorption of polyelectrolytes on crystalline surfaces based on experimental, computational, and theoretical studies.

Ion Chelation by Polyelectrolytes

The solution behavior of polyelectrolytes in multi-valent salt solutions poses important challenges in designing polyelectrolytes with enhanced antiscalant activity, as the polyelectrolyte–ion complex itself can precipitate and lead to further scale deposition [8, 38–48]. The effectiveness of PAA and other scale inhibitors relies heavily on the polymer's capacity to simultaneously bind numerous Ca^{2+} ions while preserving polyelectrolyte–ion complex solubility. By carefully tuning the ionic strength and valency, intriguing phenomena known as "salting out" and "salting in" can be induced, leading to the precipitation or re-dissolution of polyelectrolytes, respectively [49–53]. Salting out can be seen experimentally by the precipitation of polyelectrolyte–Ca^{2+} complexes at high Ca^{2+} concentrations, as shown in Figure 1.4 for a poly(vinylphosphonic acid-co-acrylic acid) (PVPA-co-AA) copolymer. While the polymer is able to effectively chelate Ca^{2+} ions at low Ca^{2+} concentrations, the formation of inter-polymer complexes at high Ca^{2+} concentrations leads to the precipitation of the polymer–Ca^{2+} complex. It is hypothesized that the inter-polymer complexes form due to the bridging of Ca^{2+} ions between polyelectrolyte chains, which leads to the precipitation of the polymer–Ca^{2+} complex [30].

Past experimental studies, such as those by Huber [54] and Schweins & Huber [55], have demonstrated that the addition of Ca^{2+} induces a transition in polymer conformation from an extended coil to a collapsed chain, which results in the precipitation of ion–PE complexes once the polymer's binding capacity is exceeded. Subsequent work conducted by Sinn *et al.* [56] found that a simple, screened-Coulomb ion–polyelectrolyte interaction model could not explain the observed precipitation phenomenon, which suggests a more complex understanding of Ca^{2+}-mediated interactions is necessary. Coarse-grained theoretical models have captured the addition of multi-valent ions leading to chain

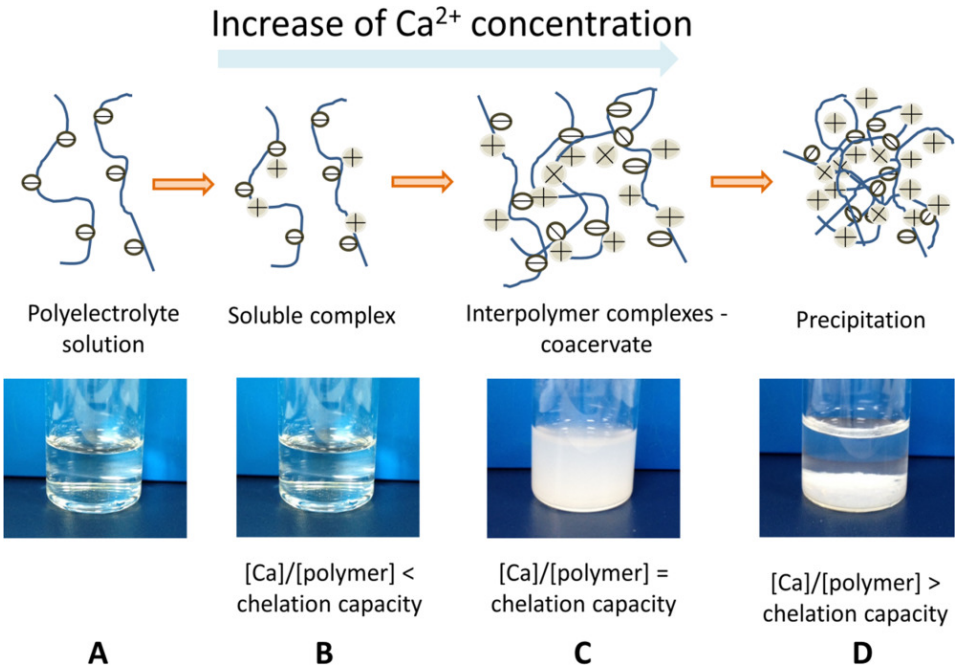

Figure 1.4: Calcium chelation mechanism of the PVPA-co-AA polymer. (A) PVPA-co-AA copolymer dissolves in aqueous solution to form a negatively-charged polyelectrolyte. (B) PVPA-co-AA can bind to divalent calcium ions. (C) Inter-polymer complexes can form at high calcium concentrations, resulting in a cloudy solution. (D) Precipitation of polymer-calcium complex at very high calcium concentrations. Reproduced from Wang *et al.* [30].

collapse. However, precipitation has been attributed to differing mechanisms, including correlations between chelated ions, ion-bridging between chains, or charge neutralization of the polymer [12, 57–59].

While theory and experiments predict precipitation of polyelectrolyte–Ca^{2+} complexes at certain conditions, to design novel polyelectrolytes that stay soluble in aqueous solution, one needs to understand the molecular principles that govern the Ca^{2+} induced association between like-charged polyelectrolytes. With all-atom resolution, we construct an adsorption isotherm to describe the binding behaviors of Ca^{2+} ions to a PAA chain and determine the different binding modes accessible for Ca^{2+} binding to the chain and quantify their impact on the adsorption isotherm in Chapter 2. We then address questions related to Ca^{2+} ion-mediated association between multiple polyelectrolyte chains and the resulting effect on the precipitation concentration of the polyelectrolyte in solution in Chapter 3.

Polyelectrolyte Adsorption on Crystalline Surfaces

Polyelectrolyte additives have also been shown to inhibit the growth of $CaCO_3$ crystals and dramatically alter the morphology of the resulting crystals [18, 60, 61], as demonstrated in Figure 1.5. The adsorption of PAA to $CaCO_3$ surfaces has also been shown to promote the formation of vaterite over calcite, which is the thermodynamically stable phase at room temperature. From X-ray diffraction (XRD), Fourier-transform infrared (FTIR) spectroscopy, and pyrolysis experiments, it is thought that the polyelectrolyte adsorption on the crystal surface is limited to an interfacial layer and does not penetrate the bulk crystal even as the surface continues to grow [62, 63].

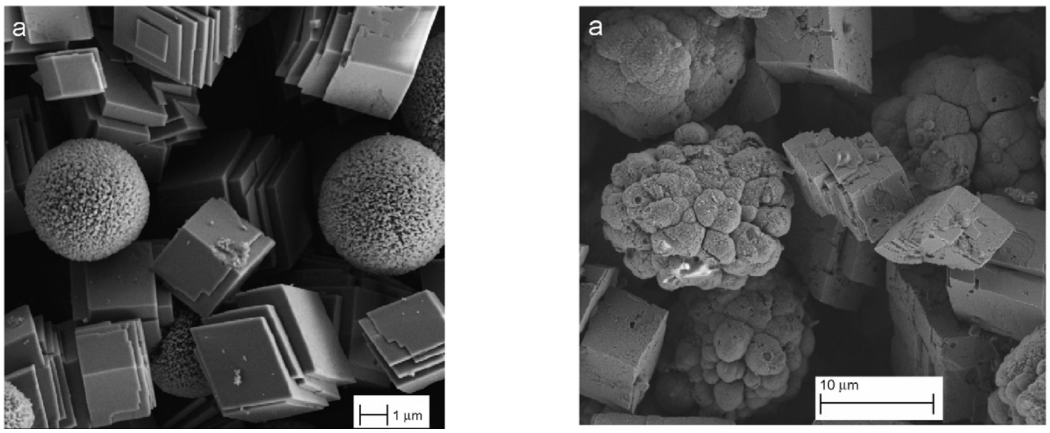

(a) (b)

Figure 1.5: Scanning electron microscopy (SEM) backscattered images of $CaCO_3$ particles synthesized at 25 °C. The calcite crystals appear as rhombohedral particles, and the vaterite crystals are spherical particles. (a) Precipitation of $CaCO_3$ particles without PAA in the system. (b) Precipitation of $CaCO_3$ particles with PAA in the system. Reproduced from Ouhenia *et al.* [18].

The binding of a polyelectrolyte on a given crystal plane will depend on the Ca^{2+} and $CO_3{}^{2-}$ surface morphology and the water structure in the interface, as well as the charge state of the polymer and the solution ionic strength. The exact mechanisms of polyelectrolyte adsorption and the associated dominant binding modes are unclear, as well as how the adsorption process may affect the $CaCO_3$ surface free energy. Previous molecular dynamics simulations have hinted that the adsorption of PAA on $CaCO_3$ surfaces may be entropically driven, with the polyelectrolyte destroying the highly ordered water structure at the interface [61, 64–67]. Nevertheless, the effects of water-mediated inter-

actions in the adsorption of polyelectrolytes on $CaCO_3$ surfaces have not been quantified, and the relative importance of the various proposed mechanisms remains unclear. In Chapter 4, we investigate the adsorption PAA on a $CaCO_3$ surface and probe the effect of chain length, charge density, and solution ionic strength. We also quantify the interfacial water structure and find that the polyelectrolyte alters its conformation to facilitate hydrogen bonding with the water molecules at the interface.

1.3 Computational Challenges

The strength of the long-ranged electrostatic interactions between polyelectrolytes and conformational chain flexibility lead to the rich observed phase behavior of polyelectrolytes in solution but also present significant computational challenges. For example, chelated ions can remain bound to the polyelectrolyte chain for microseconds and longer timescales, leading to slow relaxation times, which can outstrip the timescales accessible to conventional molecular dynamics simulations. Multiple ion binding modes and their coupling to the polyelectrolyte conformation further complicates the simulation of polyelectrolytes in solution as equilibrium statistics require all metastable states to be sampled adequately to reconstruct the free energy landscape [68].

Previous studies have employed limited simulation box sizes and integration timescales, which may not be sufficient to capture the full range of polyelectrolyte conformations and ion binding modes [69–71]. Recent advances in computational hardware (e.g., graphics processing units) [72], generalized force fields [73–81], and importance sampling algorithms [82–92] have enabled the simulation of rare events and long timescales, providing new insights into the behavior of polyelectrolytes in solution.

To address these challenges, we employ a combination of multiple state-of-the-art enhanced sampling algorithms and machine learning techniques to study the phase behavior of polyelectrolytes in solution and at interfaces. One of the most widely used enhanced sampling techniques is metadynamics, which has been successfully applied to study the free energy landscapes of complex systems [83–85, 93, 94]. Metadynamics can be used to enhance the sampling of rare events and explore the free energy landscape by iteratively adding a bias potential to the system based on a set of collective variables (CVs) that describe the key features of the system [83]. The bias potential encourages the system to

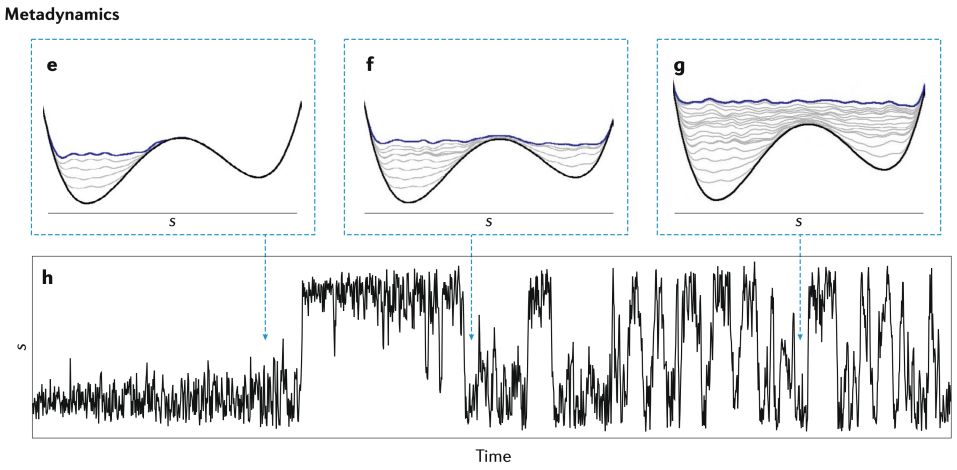

Figure 1.6: Schematic of the metadynamics simulation technique. The collective variables (CVs) as a function of time. (e–g) The sum of the free energy and of the metadynamics bias potential at three different times is marked by arrows (h), along with the free energy (black lines). (h) The CVs as a function of time in a metadynamics simulation. The free energy surface is sampled by adding a bias potential to the system. The bias potential is updated at each time step to encourage the system to explore new regions of phase space. Reproduced from Bussi & Laio [93].

explore new regions of the CV phase space and is updated intermittently with a Gaussian-shaped potential addition, as shown in Figure 1.6. Over sufficient timescales, the bias potential flattens the free energy landscape, allowing for faster diffusive sampling of the system's phase space along the chosen CVs. Given a converged metadynamics simulation, the free energy landscape can be reconstructed from the accumulated bias potential, providing insights into the system's thermodynamics and structure. Importantly, the presence of the bias potential alters the system's dynamics and kinetics, which are not representative of the unbiased system dynamics.

The choice of CVs is highly system-dependent and nontrivial, as CVs should be able to describe the system's slow degrees of freedom and distinguish between different metastable states [95, 96]. In practice, the selection of CVs is often guided by prior knowledge of the system, such as the presence of specific interactions or slow relaxation processes. However, the choice of CVs can be challenging, especially for complex systems with many degrees of freedom. Numerous variants of metadynamics have been developed to address the limitations of the original metadynamics algorithm with CV selection and

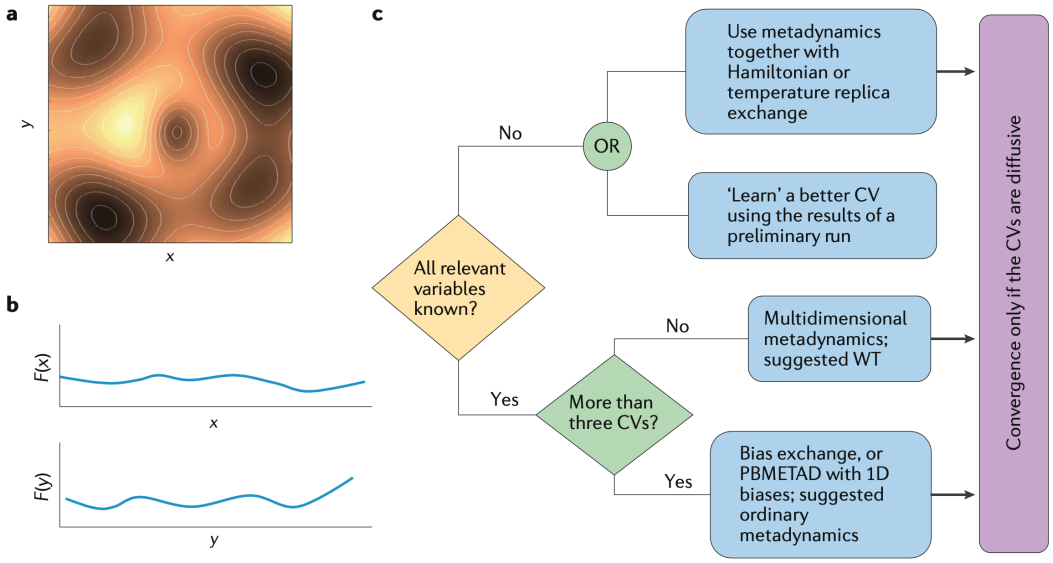

Figure 1.7: Workflow to select the optimal collective variables and metadynamics technique. (a, b) An example of a potential energy landscape characterized by the presence of deep minima (a), but whose free energy F as a function of two variables (x and y) is approximately flat (b). This situation is rather common in practical applications. (c) A decision tree for choosing the most appropriate version of metadynamics. CV, collective variable; PBMETAD, parallel-bias metadynamics; WT, well-tempered. The free energy surface is sampled by adding a bias potential to the system. The bias potential is updated at each time step to encourage the system to explore new regions of phase space. Reproduced from Bussi & Laio [93].

machine learning techniques have been developed to learn the optimal CVs, as illustrated in Figure 1.7 for a simplified two-dimensional potential energy landscape [93, 97–102].

The choice of CVs can significantly impact the efficiency and accuracy of the metadynamics simulations. A suboptimal set of CVs can lead to slow convergence or incorrect free energy landscapes due to "hidden" slow CVs that are not explicitly included in the simulation. Additional simulation replicas can be used to enhance the sampling of non-CVs and improve the convergence of the metadynamics simulations, but this increase in general sampling efficiency comes at a significant increase in computational cost [91, 92]. In our work, we employ a combination of metadynamics variants, machine learning techniques, and multiple replicas to study the behavior of polyelectrolytes in solution and at interfaces with high accuracy and efficiency.

1.4 Outline

In the remainder of Part I, we discuss our molecular dynamics simulations of polyelectrolytes and multi-valent ions in solution. Chapter 2 presents our study of the adsorption isotherm and mechanism of Ca^{2+} binding to PAA chains, where we find a coupled site-binding and conformational transition mechanism. In Chapter 3, we extend our study to the association between polyelectrolyte chains in the presence of Ca^{2+} ions to understand the role of bridging in the formation of polyelectrolyte complexes. Finally, Chapter 4 highlights the adsorption of polyelectrolytes on crystalline surfaces where indirect interactions between the polyelectrolyte and the surface are mediated by highly ordered interfacial water layers.

References

1. Bolto, B. & Gregory, J. Organic polyelectrolytes in water treatment. *Water Research* **41,** 2301–2324 (2007).

2. Lankalapalli, S. & Kolapalli, V. Polyelectrolyte complexes: A review of their applicability in drug delivery technology. *Indian Journal of Pharmaceutical Sciences* **71,** 481 (2009).

3. Reddy, M. M. & Hoch, A. R. Calcite crystal growth rate inhibition by polycarboxylic acids. *Journal of Colloid and Interface Science* **235.** Publisher: Academic Press Inc., 365–370. ISSN: 00219797 (Mar. 2001).

4. Amjad, Z., Zuhl, R. W. & Zibrida, J. F. *Factors Influencing the Precipitation of Calcium-Inhibitor Salts in Industrial Water Systems Carbosperse K-700 Water Treatment Polymers* tech. rep. Volume: 17 (ZIBEX, Inc, 2003).

5. Manning, G. S. Polyelectrolytes. *Annual Review of Physical Chemistry* **23,** 117–140 (1972).

6. Rubinstein, M., Colby, R. H. & Dobrynin, A. V. Dynamics of semidilute polyelectrolyte solutions. *Physical Review Letters* **73,** 2776 (1994).

7. Liu, S., Ghosh, K. & Muthukumar, M. Polyelectrolyte solutions with added salt: A simulation study. *The Journal of Chemical Physics* **119,** 1813–1823 (2003).

8. Muthukumar, M. 50th Anniversary Perspective: A Perspective on Polyelectrolyte Solutions. *Macromolecules* **50,** 9528–9560. ISSN: 0024-9297, 1520-5835. `https://pubs.acs.org/doi/10.1021/acs.macromol.7b01929` (2022) (Dec. 2017).

9. Wang, Z. G. 50th Anniversary Perspective: Polymer Conformation — A Pedagogical Review. *Macromolecules* **50,** 9073–9114. ISSN: 15205835 (2017).

10. Gensel, J. *Polyelectrolyte Coatings with Internal Hierarchy* PhD thesis (University of Bayreuth, 2013).

11. De La Cruz, M. O. *et al.* Precipitation of highly charged polyelectrolyte solutions in the presence of multivalent salts. *The Journal of Chemical Physics* **103,** 5781–5791. ISSN: 0021-9606, 1089-7690. `https://pubs.aip.org/jcp/article/103/13/5781/293715/Precipitation-of-highly-charged-polyelectrolyte` (2023) (Oct. 1995).

12. Wittmer, J., Johner, A. & Joanny, J. F. Precipitation of Polyelectrolytes in the Presence of Multivalent Salts. *Journal de Physique II* **5,** 635–654. ISSN: 1155-4312, 1286-4870. `http://www.edpsciences.org/10.1051/jp2:1995154` (2023) (Apr. 1995).

13. Ermoshkin, A. V. & Olvera De La Cruz, M. Polyelectrolytes in the Presence of Multivalent Ions: Gelation Versus Segregation. *Physical Review Letters* **90,** 125504. ISSN: 0031-9007, 1079-7114. https://link.aps.org/doi/10.1103/PhysRevLett.90.125504 (2023) (Mar. 2003).

14. Holm, C. *et al. Polyelectrolyte Theory* (Springer, 2004).

15. Statt, A., Casademunt, H., Brangwynne, C. P. & Panagiotopoulos, A. Z. Model for disordered proteins with strongly sequence-dependent liquid phase behavior. *The Journal of Chemical Physics* **152** (2020).

16. Yu, J., Lei, M., Cheng, B. & Zhao, X. Effects of PAA additive and temperature on morphology of calcium carbonate particles. *Journal of Solid State Chemistry* **177,** 681–689. https://doi.org/10.1016/j.jssc.2003.08.017 (Mar. 2004).

17. Gebauer, D., Völkel, A. & Cölfen, H. Stable Prenucleation Calcium Carbonate Clusters. *Science* **322,** 1819–1822. ISSN: 0036-8075, 1095-9203. https://www.science.org/doi/10.1126/science.1164271 (2022) (Dec. 2008).

18. Ouhenia, S., Chateigner, D., Belkhir, M., Guilmeau, E. & Krauss, C. Synthesis of calcium carbonate polymorphs in the presence of polyacrylic acid. *Journal of Crystal Growth* **310,** 2832–2841 (2008).

19. Picker, A., Kellermeier, M., Seto, J., Gebauer, D. & Cölfen, H. The multiple effects of amino acids on the early stages of calcium carbonate crystallization. *Zeitschrift für Kristallographie - Crystalline Materials* **227,** 744–757. ISSN: 2194-4946. https://www.degruyter.com/document/doi/10.1524/zkri.2012.1569/html (2022) (Nov. 2012).

20. Keller, H. & Plank, J. Mineralisation of CaCO3 in the presence of polycarboxylate comb polymers. *Cement and Concrete Research* **54,** 1–11. ISSN: 00088846 (2013).

21. Demichelis, R. *et al.* Simulation of Crystallization of Biominerals. *Annual Review of Materials Research* **48.** https://doi.org/10.1146/annurev-matsci-070317- (2018).

22. Jafar Mazumder, M. A. A review of green scale inhibitors: Process, types, mechanism and properties. *Coatings* **10.** Publisher: MDPI AG, 1–29. ISSN: 20796412 (Oct. 2020).

23. Antony, A. *et al.* Scale formation and control in high pressure membrane water treatment systems: A review. *Journal of Membrane Science* **383,** 1–16. https://doi.org/10.1016/j.memsci.2011.08.054 (Nov. 2011).

24. Tijing, L. D., Kim, H. Y., Lee, D. H., Kim, C. S. & Cho, Y. I. Physical water treatment using RF electric fields for the mitigation of CaCO3 fouling in cooling water. *International Journal of Heat and Mass Transfer* **53,** 1426–1437. https://doi.org/10.1016/j.ijheatmasstransfer.2009.12.009 (Mar. 2010).

25. Muryanto, S., Bayuseno, A., Ma'mun, H., Usamah, M. & Jotho. Calcium Carbonate Scale Formation in Pipes: Effect of Flow Rates, Temperature, and Malic Acid as Additives on the Mass and Morphology of the Scale. *Procedia Chemistry* **9,** 69–76. https://doi.org/10.1016/j.proche.2014.05.009 (2014).

26. Huang, S.-C., Naka, K. & Chujo, Y. Effect of Molecular Weights of Poly(acrylic acid) on Crystallization of Calcium Carbonate by the Delayed Addition Method. *Polymer Journal* **40,** 154–162. https://doi.org/10.1295/polymj.pj2007162 (Dec. 2007).

27. Sinn, C. G., Dimova, R. & Antonietti, M. Isothermal Titration Calorimetry of the Polyelectrolyte/Water Interaction and Binding of Ca^{2+}: Effects Determining the Quality of Polymeric Scale Inhibitors. *Macromolecules* **37,** 3444–3450. https://doi.org/10.1021/ma030550s (Apr. 2004).

28. Aschauer, U., Spagnoli, D., Bowen, P. & Parker, S. C. Growth modification of seeded calcite using carboxylic acids: Atomistic simulations. *Journal of Colloid and Interface Science* **346,** 226–231. https://doi.org/10.1016/j.jcis.2010.02.057 (June 2010).

29. Backer, S., Creamer, M., Pulukkody, R. & Ferrieux, S. Patent number: US20210324304. https://patents.google.com/patent/US20210324304A1/en?oq=US2021-0324304 (2024)(2021).

30. Wang, Q. G. *et al.* The unique calcium chelation property of poly(vinyl phosphonic acid-co-acrylic acid) and effects on osteogenesis *in vitro*: Calcium chelation property of PVPA-co-AA. *Journal of Biomedical Materials Research Part A* **106,** 168–179. ISSN: 15493296. https://onlinelibrary.wiley.com/doi/10.1002/jbm.a.36223 (2023) (Jan. 2018).

31. Manning, G. S. Counterion binding in polyelectrolyte theory. *Accounts of Chemical Research* **12,** 443–449 (1979).

32. De la Cruz, M. O. *et al.* Precipitation of highly charged polyelectrolyte solutions in the presence of multivalent salts. *The Journal of Chemical Physics* **103,** 5781–5791. https://doi.org/10.1063/1.470459 (Oct. 1995).

33. Barrat, J.-L. & Joanny, J.-F. *Theory of Polyelectrolyte Solutions* en. arXiv:cond-mat/9601022. Jan. 1996. http://arxiv.org/abs/cond-mat/9601022 (2023).

34. Castelnovo, M., Sens, P. & Joanny, J.-F. Charge distribution on annealed polyelectrolytes. *European Physical Journal E* **1,** 115–125. ISSN: 1292-8941. http://link.springer.com/10.1007/PL00014591 (2022) (Feb. 2000).

35. Huang, C.-I. & Olvera de La Cruz, M. Polyelectrolytes in multivalent salt solutions: Monomolecular versus multimolecular aggregation. *Macromolecules* **35,** 976–986 (2002).

36. Kundagrami, A. & Muthukumar, M. Theory of competitive counterion adsorption on flexible polyelectrolytes: Divalent salts. *The Journal of Chemical Physics* **128** (2008).

37. Lee, C.-L. & Muthukumar, M. Phase behavior of polyelectrolyte solutions with salt. *The Journal of Chemical Physics* **130** (2009).

38. Schweins, R. & Huber, K. Collapse of sodium polyacrylate chains in calcium salt solutions. *The European Physical Journal E* **5,** 117–126. https://doi.org/10.1007/s101890170093 (May 2001).

39. Schweins, R., Lindner, P. & Huber, K. Calcium Induced Shrinking of NaPA Chains: A SANS Investigation of Single Chain Behavior. *Macromolecules* **36,** 9564–9573. https://doi.org/10.1021/ma0347722 (Nov. 2003).

40. Michaeli, I. Ion binding and the formation of insoluble polymethacrylic salts. *Journal of Polymer Science* **48,** 291–299. https://doi.org/10.1002/pol.1960.1204815027 (Dec. 1960).

41. Schweins, R., Goerigk, G. & Huber, K. Shrinking of anionic polyacrylate coils induced by Ca^{2+}, Sr^{2+} and Ba^{2+}: A combined light scattering and ASAXS study. *The European Physical Journal E* **21,** 99–110. https://doi.org/10.1140/epje/i2006-10047-7 (Oct. 2006).

42. Yethiraj, A. Liquid State Theory of Polyelectrolyte Solutions. *The Journal of Physical Chemistry B* **113,** 1539–1551. https://doi.org/10.1021/jp8069964 (Nov. 2008).

43. Park, S., Zhu, X. & Yethiraj, A. Atomistic Simulations of Dilute Polyelectrolyte Solutions. *The Journal of Physical Chemistry B* **116,** 4319–4327. https://doi.org/10.1021/jp208138t (Apr. 2012).

44. Mantha, S. & Yethiraj, A. Conformational Properties of Sodium Polystyrenesulfonate in Water: Insights from a Coarse-Grained Model with Explicit Solvent. *The Journal of Physical Chemistry B* **119,** 11010–11018. https://doi.org/10.1021/acs.jpcb.5b01700 (June 2015).

45. Chialvo, A. A. & Simonson, J. M. Solvation Behavior of Short-Chain Polystyrene Sulfonate in Aqueous Electrolyte Solutions: A Molecular Dynamics Study. *The Journal of Physical Chemistry B* **109,** 23031–23042. https://doi.org/10.1021/jp053512e (Nov. 2005).

46. Dobrynin, A. V. Effect of Counterion Condensation on Rigidity of Semiflexible Polyelectrolytes. *Macromolecules* **39,** 9519–9527. https://doi.org/10.1021/ma061030a (Dec. 2006).

47. Prabhu, V. M. Counterion structure and dynamics in polyelectrolyte solutions. *Current Opinion in Colloid & Interface Science* **10,** 2–8. https://doi.org/10.1016/j.cocis.2005.04.002 (Aug. 2005).

48. Duan, C. & Wang, R. Association of two polyelectrolytes in salt solutions. *Soft Matter* **18,** 6934–6941. https://doi.org/10.1039/d2sm00839d (2022).

49. Arakawa, T. & Timasheff, S. N. Mechanism of protein salting in and salting out by divalent cation salts: Balance between hydration and salt binding. *Biochemistry* **23,** 5912–5923 (1984).

50. Allahyarov, E., D'Amico, I. & Löwen, H. Attraction between Like-Charged Macroions by Coulomb Depletion. *Physical Review Letters* **81,** 1334–1337. ISSN: 0031-9007, 1079-7114. https://link.aps.org/doi/10.1103/PhysRevLett.81.1334 (2023) (Aug. 1998).

51. Curtis, R. A., Ulrich, J., Montaser, A., Prausnitz, J. M. & Blanch, H. W. Protein-protein interactions in concentrated electrolyte solutions. *Biotechnology and Bioengineering* **79,** 367–380. ISSN: 0006-3592, 1097-0290. https://onlinelibrary.wiley.com/doi/10.1002/bit.10342 (2023) (Aug. 2002).

52. Saluja, A. *et al.* Anion Binding Mediated Precipitation of a Peptibody. *Pharmaceutical Research* **26,** 152. ISSN: 0724-8741, 1573-904X. http://link.springer.com/10.1007/s11095-008-9722-0 (2023) (Jan. 2009).

53. Li, Y., Girard, M., Shen, M., Millan, J. A. & Olvera De La Cruz, M. Strong attractions and repulsions mediated by monovalent salts. *Proceedings of the National Academy of Sciences of the United States of America* **114,** 11838–11843. ISSN: 0027-8424, 1091-6490. https://pnas.org/doi/full/10.1073/pnas.1713168114 (2023) (Nov. 2017).

54. Huber, K. Calcium-induced shrinking of polyacrylate chains in aqueous solution. *The Journal of Physical Chemistry* **97,** 9825–9830 (1993).

55. Schweins, R. & Huber, K. Collapse of sodium polyacrylate chains in calcium salt solutions. *European Physical Journal E* **5,** 117–126 (2001).

56. Sinn, C. G., Dimova, R. & Antonietti, M. Isothermal Titration Calorimetry of the Polyelectrolyte/Water Interaction and Binding of Ca^{2+} : Effects Determining the Quality of Polymeric Scale Inhibitors. *Macromolecules* **37,** 3444–3450. ISSN: 0024-9297, 1520-5835. https://pubs.acs.org/doi/10.1021/ma030550s (2022) (May 2004).

57. Ha, B.-Y. & Liu, A. J. Counterion-Mediated Attraction between Two Like-Charged Rods. *Physical Review Letters* **79,** 1289–1292. ISSN: 0031-9007, 1079-7114. https://link.aps.org/doi/10.1103/PhysRevLett.79.1289 (2023) (Aug. 1997).

58. Arenzon, J., Stilck, J. & Levin, Y. Simple model for attraction between like-charged polyions. *European Physical Journal B* **12,** 79–82. ISSN: 1434-6028. http://link.springer.com/10.1007/s100510050980 (2023) (Oct. 1999).

59. Solis, F. J. & De La Cruz, M. O. Collapse of flexible polyelectrolytes in multivalent salt solutions. *The Journal of Chemical Physics* **112,** 2030–2035 (2000).

60. Gower, L. & Tirrell, D. Calcium carbonate films and helices grown in solutions of poly(aspartate). *Journal of Crystal Growth* **191,** 153–160. ISSN: 00220248. https://linkinghub.elsevier.com/retrieve/pii/S0022024898000025 (2022) (July 1998).

61. Aschauer, U., Spagnoli, D., Bowen, P. & Parker, S. C. Growth modification of seeded calcite using carboxylic acids: Atomistic simulations. *Journal of Colloid and Interface Science* **346,** 226–231. ISSN: 00219797. https://linkinghub.elsevier.com/retrieve/pii/S0021979710002614 (2022) (2010).

62. Huang, S.-C., Naka, K. & Chujo, Y. A carbonate controlled-addition method for amorphous calcium carbonate spheres stabilized by poly (acrylic acid)s. *Langmuir* **23,** 12086–12095 (2007).

63. Huang, S.-C., Naka, K. & Chujo, Y. Effect of molecular weights of poly (acrylic acid) on crystallization of calcium carbonate by the delayed addition method. *Polymer Journal* **40,** 154–162 (2008).

64. De Leeuw, N. H. & Parker, S. C. *Surface Structure and Morphology of Calcium Carbonate Polymorphs Calcite, Aragonite, and Vaterite: An Atomistic Approach* tech. rep. (1998).

65. Sparks, D. J. *et al.* Adsorption of poly acrylic acid onto the surface of calcite: An experimental and simulation study (SUPPLEMENTAL). *Physical Chemistry Chemical Physics* **17,** 27357–27365. ISSN: 1463-9076, 1463-9084. http://xlink.rsc.org/?DOI=C5CP00945F (2022) (2015).

66. Chun, B. J., Lee, S. G., Choi, J. I. & Jang, S. S. Adsorption of carboxylate on calcium carbonate (10 1 4) surface: Molecular simulation approach. *Colloids and Surfaces A: Physicochemical and Engineering Aspects* **474.** Publisher: Elsevier B.V., 9–17. ISSN: 18734359 (June 2015).

67. Zhu, B., Xu, X. & Tang, R. Hydration layer structures on calcite facets and their roles in selective adsorptions of biomolecules: A molecular dynamics study. *The Journal of Chemical Physics* **139,** 234705. ISSN: 0021-9606, 1089-7690. `http://aip.scitation.org/doi/10.1063/1.4848696` (2022) (Dec. 2013).

68. Glisman, A. *et al.* Adsorption isotherm and mechanism of Ca^{2+} binding to polyelectrolyte. *arXiv preprint arXiv:2311.11404* (2023).

69. Molnar, F. & Rieger, J. "Like-Charge Attraction" between Anionic Polyelectrolytes: Molecular Dynamics Simulations. *Langmuir* **21,** 786–789. ISSN: 0743-7463, 1520-5827. `https://pubs.acs.org/doi/10.1021/la048057c` (2023) (Jan. 2005).

70. Bulo, R. E. *et al.* "Site Binding" of Ca^{2+} Ions to Polyacrylates in Water: A Molecular Dynamics Study of Coiling and Aggregation. *Macromolecules* **40,** 3437–3442. ISSN: 0024-9297, 1520-5835. `https://pubs.acs.org/doi/10.1021/ma0624671` (2022) (May 2007).

71. Tribello, G. A., Liew, C. & Parrinello, M. Binding of Calcium and Carbonate to Polyacrylates. *The Journal of Physical Chemistry B* **113,** 7081–7085. ISSN: 1520-6106, 1520-5207. `https://pubs.acs.org/doi/10.1021/jp900283d` (2022) (May 2009).

72. Kutzner, C. *et al.* More bang for your buck: Improved use of GPU nodes for GROMACS 2018. *Journal of Computational Chemistry* **40,** 2418–2431 (2019).

73. Wang, J., Wolf, R. M., Caldwell, J. W., Kollman, P. A. & Case, D. A. Development and testing of a general amber force field. *Journal of Computational Chemistry* **25,** 1157–1174 (2004).

74. He, X., Man, V. H., Yang, W., Lee, T.-S. & Wang, J. A fast and high-quality charge model for the next generation general AMBER force field. *The Journal of Chemical Physics* **153** (2020).

75. Sprenger, K., Jaeger, V. W. & Pfaendtner, J. The general AMBER force field (GAFF) can accurately predict thermodynamic and transport properties of many ionic liquids. *The Journal of Physical Chemistry B* **119,** 5882–5895 (2015).

76. Jo, S., Kim, T., Iyer, V. G. & Im, W. CHARMM-GUI: A web-based graphical user interface for CHARMM. *Journal of Computational Chemistry* **29,** 1859–1865 (2008).

77. Vanommeslaeghe, K. *et al.* CHARMM general force field: A force field for drug-like molecules compatible with the CHARMM all-atom additive biological force fields. *Journal of Computational Chemistry* **31,** 671–690 (2010).

78. Kaminski, G. A., Friesner, R. A., Tirado-Rives, J. & Jorgensen, W. L. Evaluation and reparametrization of the OPLS-AA force field for proteins via comparison with accurate quantum chemical calculations on peptides. *The Journal of Physical Chemistry B* **105,** 6474–6487 (2001).

79. Vassetti, D., Pagliai, M. & Procacci, P. Assessment of GAFF2 and OPLS-AA general force fields in combination with the water models TIP3P, SPCE, and OPC3 for the solvation free energy of druglike organic molecules. *Journal of Chemical Theory and Computation* **15,** 1983–1995 (2019).

80. Duboué-Dijon, E., Javanainen, M., Delcroix, P., Jungwirth, P. & Martinez-Seara, H. A practical guide to biologically relevant molecular simulations with charge scaling for electronic polarization. *The Journal of Chemical Physics* **153.** https://doi.org/10.1063/5.0017775 (Aug. 2020).

81. Leontyev, I. & Stuchebrukhov, A. Accounting for electronic polarization in non-polarizable force fields. *Physical Chemistry Chemical Physics* **13,** 2613. https://doi.org/10.1039/c0cp01971b (2011).

82. Torrie, G. M. & Valleau, J. P. Nonphysical sampling distributions in Monte Carlo free-energy estimation: Umbrella sampling. *Journal of Computational Physics* **23,** 187–199 (1977).

83. Laio, A. & Parrinello, M. Escaping free-energy minima. *Proceedings of the National Academy of Sciences of the United States of America* **99.** www.pnas.orgcgidoi10.1073pnas.202427399 (Oct. 2002).

84. Laio, A. & Gervasio, F. L. Metadynamics: A method to simulate rare events and reconstruct the free energy in biophysics, chemistry and material science. *Reports on Progress in Physics* **71,** 126601. ISSN: 0034-4885, 1361-6633. https://iopscience.iop.org/article/10.1088/0034-4885/71/12/126601 (2022) (Dec. 2008).

85. Tiwary, P. & Parrinello, M. From Metadynamics to Dynamics. *Physical Review Letters* **111,** 230602. ISSN: 0031-9007, 1079-7114. https://link.aps.org/doi/10.1103/PhysRevLett.111.230602 (2022) (Dec. 2013).

86. Invernizzi, M. & Parrinello, M. Rethinking Metadynamics: From Bias Potentials to Probability Distributions. *The Journal of Physical Chemistry Letters* (2020).

87. Invernizzi, M., Piaggi, P. M. & Parrinello, M. Unified approach to enhanced sampling. *Physical Review X* **10,** 041034 (2020).

88. Rizzi, V., Aureli, S., Ansari, N. & Gervasio, F. L. OneOPES, a Combined Enhanced Sampling Method to Rule Them All. *Journal of Chemical Theory and Computation,* acs.jctc.3c00254. ISSN: 1549-9618, 1549-9626. https://pubs.acs.org/doi/10.1021/acs.jctc.3c00254 (2023) (Aug. 2023).

89. Ribeiro, J. M. L., Bravo, P., Wang, Y. & Tiwary, P. Reweighted autoencoded variational Bayes for enhanced sampling (RAVE). *The Journal of Chemical Physics* **149,** 072301. ISSN: 0021-9606, 1089-7690. https://pubs.aip.org/jcp/article/149/7/072301/1059173/Reweighted-autoencoded-variational-Bayes-for (2024) (Aug. 2018).

90. Wang, D. & Tiwary, P. State predictive information bottleneck. *The Journal of Chemical Physics* **154,** 134111. ISSN: 0021-9606, 1089-7690. https://pubs.aip.org/jcp/article/154/13/134111/1013207/State-predictive-information-bottleneck (2024) (Apr. 2021).

91. Wang, L., Friesner, R. A. & Berne, B. J. Replica Exchange with Solute Scaling: A More Efficient Version of Replica Exchange with Solute Tempering (REST2). *The Journal of Physical Chemistry B* **115,** 9431–9438. https://doi.org/10.1021/jp204407d (July 2011).

92. Bussi, G. Hamiltonian replica exchange in GROMACS: A flexible implementation. *Molecular Physics* **112,** 379–384. https://doi.org/10.1080/00268976.2013.824126 (Aug. 2013).

93. Bussi, G. & Laio, A. Using metadynamics to explore complex free-energy landscapes. *Nature Reviews Physics* **2,** 200–212 (2020).

94. Barducci, A., Bussi, G. & Parrinello, M. Well-tempered metadynamics: A smoothly converging and tunable free-energy method. *Physical Review Letters* **100.** arXiv: 0803.3861. ISSN: 00319007 (Jan. 2008).

95. *Biomolecular Simulations: Methods and Protocols* (eds Bonomi, M. & Camilloni, C.) http://link.springer.com/10.1007/978-1-4939-9608-7 (2022) (Springer New York, New York, NY, 2019).

96. Bussi, G. & Tribello, G. A. en. in *Biomolecular Simulations* (eds Bonomi, M. & Camilloni, C.) Series Title: Methods in Molecular Biology, 529–578 (Springer New York, New York, NY, 2019). http://link.springer.com/10.1007/978-1-4939-9608-7_21 (2022).

97. Dorfer, M., Kelz, R. & Widmer, G. *Deep Linear Discriminant Analysis* arXiv:1511.04707 [cs]. Feb. 2016. http://arxiv.org/abs/1511.04707 (2023).

98. Mardt, A., Pasquali, L., Wu, H. & Noé, F. VAMPnets for deep learning of molecular kinetics. *Nature Communications* **9,** 5. ISSN: 2041-1723. https://www.nature.com/articles/s41467-017-02388-1 (2023) (Jan. 2018).

99. Bonati, L., Piccini, G. & Parrinello, M. Deep learning the slow modes for rare events sampling. *Proceedings of the National Academy of Sciences* **118,** e2113533118. ISSN: 0027-8424, 1091-6490. https://pnas.org/doi/full/10.1073/pnas.2113533118 (2023) (Nov. 2021).

100. Wang, D., Qiu, Y., Beyerle, E., Huang, X. & Tiwary, P. *An Information Bottleneck Approach for Markov Model Construction* arXiv:2404.02856 [physics]. Apr. 2024. http://arxiv.org/abs/2404.02856 (2024).

101. Glielmo, A. *et al.* Unsupervised Learning Methods for Molecular Simulation Data. *Chemical Reviews* **121,** 9722–9758. ISSN: 0009-2665, 1520-6890. https://pubs.acs.org/doi/10.1021/acs.chemrev.0c01195 (2023) (Aug. 2021).

102. Mehdi, S., Smith, Z., Herron, L., Zou, Z. & Tiwary, P. *Enhanced Sampling with Machine Learning: A Review* arXiv:2306.09111 [cond-mat, physics:physics]. June 2023. http://arxiv.org/abs/2306.09111 (2023).

Chapter 2

ADSORPTION ISOTHERM AND MECHANISM OF CA^{2+} BINDING TO POLYELECTROLYTES

Polyelectrolytes, such as polyacrylic acid (PAA), can effectively mitigate $CaCO_3$ scale formation. Despite their success as antiscalants, the underlying mechanism of Ca^{2+} binding to polyelectrolyte chains remains unresolved. Through all-atom molecular dynamics simulations, we construct an adsorption isotherm of Ca^{2+} binding to sodium polyacrylate (NaPAA) and investigate the associated binding mechanism. We find that the number of calcium ions adsorbed $[Ca^{2+}]_{ads}$ to the polymer saturates at moderately high concentrations of free calcium ions $[Ca^{2+}]_{aq}$ in the solution. This saturation value is intricately connected with the binding modes accessible to Ca^{2+} ions when they bind to the polyelectrolyte chain. We identify two dominant binding modes: the first involves binding to at most two carboxylate oxygens on a polyacrylate chain, and the second, termed the high binding mode, involves binding to four or more carboxylate oxygens. As the concentration of free calcium ions $[Ca^{2+}]_{aq}$ increases from low to moderate levels, the polyelectrolyte chain undergoes a conformational transition from an extended coil to a hairpin-like structure, enhancing the accessibility to the high binding mode. At moderate concentrations of $[Ca^{2+}]_{aq}$, the high binding mode accounts for at least a third of all binding events. The chain's conformational change and its consequent access to the high binding mode is found to increase the overall Ca^{2+} ion binding capacity of the polyelectrolyte chain.

This chapter includes content from our previously published article:

1. Glisman, A. *et al.* Adsorption isotherm and mechanism of Ca^{2+} binding to polyelectrolyte. *Langmuir* **40,** 6212–6219 (2024).

2.1 Introduction

Divalent metal ions, such as Ca^{2+}, exhibit a pronounced affinity for dissolved anions like carbonate (CO_3^{2-}) in an aqueous solution. The ion pairs, which readily associate, precipitate out of solution and form solid deposits (scale) due to their low solubility limit. Scale formation presents challenges to residential and industrial piping systems, restricting the fluid flow and fouling components [1–3]. These metal ions also form complexes with household products, such as detergents, and disrupt their efficacy.

Polyelectrolytes, such as polyacrylic acid (PAA), are commonly employed to mitigate scale formation [4–8]. Although it is not fully understood what makes an effective antiscalant polyelectrolyte, a few mechanisms for scale prevention have been proposed. The polyelectrolytes could prevent nucleation via chelating metal ions from the solution [5, 9]. The chelation reduces the concentration of metal ion and the likelihood of their association with the dissolved anions. Simultaneously, polyelectrolytes could also adsorb onto the surfaces of scale crystals and prevent further growth or deposition [6, 7, 10, 11].

The solution behavior of polyelectrolytes in divalent salt solutions poses important challenges in designing polyelectrolytes with enhanced antiscalant activity, as the polyelectrolyte–ion complex itself can precipitate and lead to further scale deposition [12–23]. Cloud point measurements revealed instances of phase separation into a polymer-poor (supernatant) liquid and a polymer-rich liquid with addition of divalent ions [24]. Boisvert *et al.* performed osmotic pressure measurements and showed that the solution behavior of polyelectrolytes in divalent salt solutions is primarily influenced by a proposed site-binding mechanism of divalent cations [25]. The site-binding mechanism facilitates bridging of non-adjacent repeat units by the divalent cations. Through a Fourier Transform Infrared (FTIR) dialysis technique, [26] Fantinel *et al.* identified monodentate, bidentate, and bridging modes when Ca^{2+} ions bind to carboxylate groups of a polyacrylate chain. However, the relative importance of each of these binding modes—particularly that of the bridging mode—on the ability of polyelectrolyte to chelate Ca^{2+} ion has not been elucidated. Furthermore, the influence of Ca^{2+} ion concentration on these binding modes remains elusive.

Mean-field theories have shed light on the solution behavior of polyelectrolytes in divalent salt solutions [27–34]. In addition to establishing conditions for the precipitation behaviors, these theoretical models have predicted a large reduction in polymer size with addition of divalent ions [35], beyond what is expected from electrostatic screening. The chain collapse was primarily attributed to ion bridging between non-neighboring repeat units. Coarse-grained implicit solvent molecular simulations, employing generic models for polyelectrolyte chains and ions, have confirmed the chain collapse and attributed it to the bridging capability of divalent ions [35–37]. All-atom molecular dynamics simulations have gone a step further by explicitly treating solvent molecules to investigate the molecular principles that govern the binding of divalent cations to the polyelectrolyte chain [38–44]. These investigations have each reported that the Ca^{2+} ion is strongly coordinated with the polyelectrolyte chain, resulting in highly coiled conformations with a chain rigidity reminiscent of crystal-like structures. Due to the strong Ca^{2+}–polyelectrolyte interactions and the number of Ca^{2+} ions binding to the polyelectrolyte chain, these models hint at the overcharging of the Ca^{2+}–polyelectrolyte complex. However, recent potentiometric titration assays [9] suggest that only $\frac{1}{3}$ of the binding sites are occupied before a fully charged polyelectrolyte chain reaches its saturated value of Ca^{2+}-binding capacity.

The saturation value in the adsorption isotherm, which describes the maximum amount of Ca^{2+} that can be bound to a polyelectrolyte chain, reflects the chelating capacity of the polyelectrolyte chain. However, the molecular principles that govern the corresponding adsorption isotherm have not been addressed. Specifically, the interplay between the site-binding nature of Ca^{2+}–polyelectrolyte interactions and the conformational transitions of the polyelectrolyte, aimed at enhancing both the chelating capacity and the solubility of the Ca^{2+}–polyelectrolyte complex, has not been explored.

In this study, we address the mechanism of Ca^{2+} adsorption onto a polyacrylate chain. We construct an adsorption isotherm to describe the binding behaviors of Ca^{2+} ions to polyacrylate. We then determine the different binding modes accessible for Ca^{2+} binding to the chain and quantify their impact on the adsorption isotherm. In our follow-up manuscript [45], we address questions related to Ca^{2+} ion-mediated association between polyelectrolyte chains. The rest of the manuscript is organized as follows. First, we present a

Label	**Ca^{2+}**	**Cl^{-}**	**Na^{+}**	**Water**
$0CaCl_2$	0	0	32	56,448
$4CaCl_2$	4	8	32	56,436
$8CaCl_2$	8	16	32	56,424
$16CaCl_2$	16	32	32	56,400
$32CaCl_2$	32	64	32	56,352
$64CaCl_2$	64	128	32	56,256
$96CaCl_2$	96	192	32	56,160
$128CaCl_2$	128	256	32	56,064

Table 2.1: Composition of the cubic simulation box with an edge length of 12 nm, containing a single sodium polyacrylate chain with 32 repeat units, and at various numbers of $CaCl_2$ in water.

Hamiltonian Replica Exchange Molecular Dynamics (HREMD) protocol to selectively bias Ca^{2+}-polyelectrolyte interactions and efficiently sample the configurational space. We then introduce a free energy perturbation approach coupled with molecular dynamics to compute the adsorption isotherm describing Ca^{2+} binding to the polyelectrolyte chain. We discuss the results of these calculations and present the conclusions.

2.2 Models

We investigated the mechanism of calcium ion binding to polyacrylate chain using all-atom molecular dynamics (MD) simulations. Our simulation system consists of a single polyacrylic acid (PAA) chain with 32 repeat units, solvated in a cubic water box with an edge length of 12 nm. All repeat units on the polymer are charged, consistent with the solution conditions for antiscalant activity(i.e., solution pH $\sim$ 10). Sodium ions were added for electroneutrality. The average end-to-end distance of such a polymer was $\sim$ 5 nm. We chose our box dimensions so that the polymer does not interact with its periodic image. In Table 2.1, we report compositions of different systems studied in this work.

Force field choice and the importance of solvent electronic polarization: We employed the Generalized AMBER Force Field (GAFF) with the SPC/E water model, which had been rigorously tested by Mintis *et al.* for modeling the polyacrylate chain [46]. During our modeling of calcium ions, we observed that the "full" electrostatic charge force field parameters overestimated calcium ion binding to carboxylate groups on the polyacrylate chain,

resulting in a charge inversion of the polymer chain inconsistent with experimental reports (see Figure S2 in the Supporting Information). Duboué-Dijon *et al.*, who investigated calcium ion binding to insulin, reported that such an overestimation was due to inadequate treatment of electronic dielectric screening when using full charges on ions with non-polarizable forcefields [47]. The correct energetics of ion-pair formation could be captured by molecular models with explicit polarization [48]. However, a general-purpose force field with explicit polarization, tested to reproduce the properties of polyacrylates, was not readily available, and polarizeable force fields introduce large computational expense.

Alternatively, in our models, we included electronic dielectric screening by uniformly scaling the charges of all solute atoms. This approach, known as the electronic continuum charge correction (ECC), is a mean-field method that attempts to mimic charge-carrying species within an electronic dielectric continuum [49, 50]. While the ECC scheme is a physically meaningful concept, it is primarily used as an *ad hoc* solution to incorporate electronic polarization into an otherwise non-polarizable force field. ECC schemes tend to fail in systems with a discontinuity in the high-frequency dielectric constant [51]. Moreover, force field parameterizations implicitly account for electronic polarization effects to some extent. Introducing additional ECC correction may overly compensate for electronic polarization effects, resulting in a significant underestimation of cohesive energy density and leading to unphysical solution behavior [52]. Nevertheless, the ECC scheme yields meaningful observations in common electrolyte systems where the high-frequency dielectric constant remains uniform throughout.

Within the scope of our study, the interactions of interest involve calcium ions and carboxylate groups on the polyacrylate chain. Biomolecular systems with the same carboxylate-calcium ion pair have shown success with ECC schemes [53–56]. We particularly employ the ECC scheme reported by Jungwirth and coworkers, who provided parameters for modeling calcium and other ions in an aqueous solution [54]. In their work, the authors uniformly scaled the charges on ions by a factor of 0.75. Lennard-Jones parameters describing dispersion interactions of corresponding ions were optimized to reproduce *ab initio* molecular dynamics results for ion-pairing and neutron scattering experiments. Such a parameter set accurately described the properties of calcium

ions in an aqueous solution and their association with carboxylate groups on amino acids. We used the same parameter set to model calcium and other ions in our simulation system. Although the ECC scheme is tailored to the specific requirements of modeling the polyacrylate–Ca^{2+}system of interest in this work, the underlying rationale—addressing electronic polarization to correct for electrostatic sources of overestimated binding affinities—is a principle that governs modeling a broad class of polyelectrolyte systems.

When modeling the electronic polarization effects of the polyacrylate chain in an aqueous solution, we scaled the partial charges of all the atoms on the polyacrylate chain by 0.75 and used Lennard-Jones parameters reported by Mintis *et al.* [46] to describe dispersion interactions. Although our approach is a commonly accepted practice [56], we emphasize that it is not rigorous. However, different properties of polymers strongly depend on their chain length, and finding the right strategy to optimize their dispersion interaction parameters is not obvious.

Since the "full-charge" parameters by Mintis *et al.* [46] reproduce the structural properties of the polyacrylate chain in a salt-free solution, we validated the predictions of the "scaled-charge" model against the former. Even though we did not re-optimize the Lennard-Jones interaction parameters of the polyelectrolyte chain, the conformational flexibility of a polyelectrolyte chain in a salt-free solution did not change. Additionally, we observed identical distributions for structural properties when compared to the "full-charge" model (see Figure S3 in the Supporting Information).

Simulation methodology: We used GROMACS 2022.3 [57–59] patched with PLUMED 2.8.1 [60–62] and employed the following protocol to conduct our molecular dynamics simulations of the systems reported in Table 2.1. First, we minimized the energy of the system using the steepest descent algorithm until the maximum force on any atom in the system was smaller than 100 kJ mol^{-1} nm^{-1}. Next, we equilibrated the system at constant NPT conditions with pressure and temperature set to 1 atm and 300 K, respectively. While fluctuations in the energy and box size minimized within a few nanoseconds of the equilibration run, it took tens of nanoseconds to equilibrate the chain structure. We used the Berendsen barostat [63] with the velocity-rescaling stochastic thermostat during the first 10 ns of the equilibration. For the remainder of the equilibration run, we switched to the Parrinello–Rahman baro-

stat [64] with the Nosé–Hoover chain thermostat for the accurate reproduction of the thermodynamic properties of the system [65, 66]. Following the equilibration run, we conducted production MD simulations of these systems in the NVT ensemble using the Nosé–Hoover chain thermostat.

We employed the leap-frog time integration algorithm with a finite time step of 2 fs to integrate the equations of motion. Additionally, we utilized the LINCS constraint algorithm to convert all bonds with hydrogen atoms into constraints [67]. We applied periodic boundary conditions along all three spatial axes and used the particle mesh Ewald (PME) method with a minimum Fourier spacing of 0.12 nm to calculate the long-ranged electrostatic interactions [68, 69]. We applied a cutoff distance of 1.2 nm for computing van der Waals interactions. We used the same distance as the real-space cut-off value while computing the PME electrostatics.

Need for enhanced sampling molecular simulations: Although the ECC scheme with the non-polarizable force field greatly reduced the PAA–Ca^{2+} binding/unbinding relaxation times, regular MD simulations were unable to efficiently sample the polymer conformational space in an aqueous $CaCl_2$ solution. Even a microsecond long trajectory was not sufficient to sample polymer conformations in any of the systems listed in Table 2.1 with calcium numbers higher than 4 Ca ions. We direct readers to Figures S4 and S5 in the Supporting Information for the relevant data and discussion.

To address the challenges associated with polymer conformational sampling in an aqueous $CaCl_2$ solution, we employed Hamiltonian Replica Exchange Molecular Dynamics (HREMD) [70, 71]. Our HREMD framework is based on the flexible implementation of the REST2 variant [70], as previously reported by Bussi [71]. We introduced a parameter λ to selectively bias the interactions between the polymer and ions, as well as the dihedral potential components of the Hamiltonian. The charges of the ions and the polymer were scaled by a factor of $\sqrt{\lambda}$, while their Lennard-Jones interaction parameter (ϵ) was scaled by λ. Similarly, the polymer dihedral potential was also scaled by λ. With this scheme for λ-parameterized Hamiltonian, $\lambda = 1$ corresponds to the system of interest with full-scale interactions. We determined that the parameterized Hamiltonian with $\lambda = 0.67$ rapidly sampled the polymer conformational space. Coordinate exchange between neighboring replicas were attempted every 500 steps. We utilized 16 replicas, with λ values ranging

from 1 to 0.67 (geometrically spaced), to simulate polymer conformations in an aqueous solution containing 8 $CaCl_2$ or 16 $CaCl_2$. For higher Ca^{2+} numbers, we increased the number of replicas to 24. This combination of number of replicas and the λ-range yielded acceptable exchange probabilities (~ 0.3) between neighboring replicas. All the relevant results reported in the subsequent sections were obtained by averaging over a 250 ns production HREMD run, conducted at constant volume and a temperature of 300 K. Our specific choice of λ-parameterization and the number of replicas in the HREMD setup was driven by the unique challenges posed by the polyacrylate-Ca^{2+} system, due to long ion pair relaxation and resulting inefficiencies in sampling polymer backbone conformations. Nevertheless, the conceptual approach of employing replica exchange variants to overcome sampling bottlenecks in polymer conformational sampling is broadly applicable to other polyelectrolyte-multivalent ion complexes [18].

Computing ion adsorption isotherm from molecular dynamics simulations: The primary objective of the current work is to investigate Ca^{2+} chelation onto a model polyacrylate chain. In an aqueous $CaCl_2$ solution containing a polyacrylate chain, a dynamic equilibrium exists between calcium ions that are freely dispersed in the solution ($Ca^{2+}_{\text{aq.free}}$) and the calcium ions adsorbed per monomer of the polyacrylate chain ($AA - Ca^{2+}$).

$$AA + Ca^{2+}_{\text{aq.free}} \rightleftharpoons AA - Ca^{2+} \tag{2.1}$$

Here, AA represents the concentration of repeat units on the polymer chain that are not bound to any calcium ions. An adsorption isotherm, quantifying Equation (2.1), describes calcium ion chelating ability of a model polyacrylate chain. We constructed the isotherm by plotting the number of calcium ions adsorbed per monomer ($AA - Ca^{2+}$) against the concentration of calcium ions that are freely dispersed in the solution ($Ca^{2+}_{\text{aq.free}}$).

Computing $AA - Ca^{2+}$ from the simulation trajectory is straightforward. We calculated the number of calcium ions that are within 0.7 nm (see SI) of the polymer atoms at each frame. This quantity was then divided by the number of repeat units per chain (i.e., 32 in this case) and ensemble averaged over the trajectory.

We determined $Ca^{2+}_{aq.free}$ by equating the chemical potential of the Ca^{2+} ions in the system ($\mu^{System}_{CaCl_2}$) with that of a pure $CaCl_2$ aqueous suspension ($\mu^{Solution}_{CaCl_2}$). This required conducting simulations of two separate sets of systems: one containing a polyacrylate chain to determine $\mu^{System}_{CaCl_2}$, and the other without a polyacrylate chain for $\mu^{Solution}_{CaCl_2}$. We employed the procedure laid out by Panagiotopoulos and coworkers to determine the chemical potentials via free energy perturbation approach [72–75].

In brief, μ_{CaCl_2} represents the change in free energy when adding (or removing) a unit of $CaCl_2$, This is expressed in Equation (2.2) as the sum of the corresponding ideal gas component ($\mu^{id}_{CaCl_2}$) and the residual component ($\mu^{R}_{CaCl_2}$).

$$\begin{aligned}
\mu_{CaCl_2} &= \mu^{id}_{CaCl_2} + \mu^{R}_{CaCl_2} \\
\mu^{id}_{CaCl_2} &= \mu^{0}_{Ca^{2+}} + 2\mu^{0}_{Cl^-} + 3RT \ln\left(\frac{\sqrt[3]{4} N_{CaCl_2} k_B T}{P^0 \langle V \rangle}\right) \\
\mu^{R}_{CaCl_2} &= \mu^{R}_{vdw} + \mu^{R}_{coul}
\end{aligned} \tag{2.2}$$

Here, $\mu^{0}_{Cl^-}$ and $\mu^{0}_{Ca^{2+}}$ are the respective chemical potentials of Cl^- and Ca^{2+} at the reference pressure of 1 bar. We used the tabulated value of $\mu^{0}_{Cl^-}$ from the NIST-JANAF thermochemical tables [76]. Moučka *et al.* estimated the value for $\mu^{0}_{Ca^{2+}}$ [77], and we employed the same value in our calculations. N_{CaCl_2} represents the number of $CaCl_2$ units in the simulation box, k_B denotes the Boltzmann constant, $P^0 = 1, \text{bar}$ is the reference pressure, and $\langle V \rangle$ stands for the average volume obtained from NPT simulations of a system with a specific composition.

To calculate $\mu^{R}_{CaCl_2}$, we gradually decoupled a Ca^{2+} and two Cl^- from the system. The initial configuration for this study came from the most probable polymer conformation identified from the previously described enhanced sampling simulations. We then tagged a Ca^{2+} ion that was adsorbed onto the polymer backbone. In a solution without the polyacrylate chain, a randomly selected Ca^{2+} ion served as the tagged ion, and a comparison point between the two systems. Regardless of the system, two randomly chosen Cl^- ions were tagged.

The electrostatic interactions of the tagged Ca^{2+} ion with other particles in the system were gradually turned off in 11 stages ($\phi = 1, 0.9, \ldots, 0$). Here, $\phi = 1$ represents the system with fully activated electrostatic interactions of

the tagged calcium ion, while $\phi = 0$ corresponds to complete deactivation. Each stage consisted of a series of molecular dynamics simulation steps, beginning with energy minimization, followed by 5 ns of equilibration and a 10 ns production simulation run at a pressure of 1 bar and a temperature of 300 K. The output from the production step of the ith stage (ϕ_i) served as the initial configuration for the MD simulation steps of the $(i+1)$th stage (ϕ_{i+1}). The same methodology was then applied to deactivate the electrostatic interactions of each tagged chloride ion and also the van der Waals interactions of the tagged calcium ion and the two tagged chloride ions. We then used the Bennett Acceptance Ratio (BAR) [78, 79] approach, natively implemented in the GROMACS MD package [57], to estimate the residual chemical potential ($\mu^{\mathrm{R}}_{\mathrm{CaCl_2}}$) from these different stages of MD simulations. Notably, given the position-dependent nature of the unbinding free energy of a Ca^{2+} ion from the polymer backbone, we calculated the unbinding free energy for each adsorbed Ca^{2+} ion individually and used their average to estimate $\mu^{\mathrm{R}}_{\mathrm{CaCl_2}}$.

2.3 Results and Discussion

The ability of a polyacrylate chain to sequester Ca^{2+} ions is intricately tied to the bulk solution concentration of Ca^{2+}, denoted as $\left[\mathrm{Ca}^{2+}_{\mathrm{aq.free}}\right]$. In Figure 2.1, we present the adsorption isotherm and describe the extent of Ca^{2+} binding onto a 32-mer polyacrylate chain as a function of $\left[\mathrm{Ca}^{2+}_{\mathrm{aq.free}}\right]$. At low Ca^{2+} concentrations, most of the binding sites on the polyacrylate chain are available, and an increase in $\left[\mathrm{Ca}^{2+}_{\mathrm{aq.free}}\right]$ results in a rapid increase in the number of Ca^{2+} ions sequestered by the polyacrylate chain. However, at moderate concentrations, the accessible binding sites become occupied, and the polyacrylate chain saturates with Ca^{2+}.

From the plateau in the adsorption isotherm, we note that the maximum binding capacity of a model polyacrylate chain is 0.40 ± 0.05 Ca^{2+} ions per monomer, which aligns with recent potentiometric titration experiments [9]. Although the adsorption isotherm bears some resemblance to a Langmuir model, we observe that the Ca^{2+} binding does not obey the model assumptions. Notably, the conformational flexibility of the polyelectrolyte chain results in distinct chemical environments around each binding site, rendering the binding sites non-equivalent.

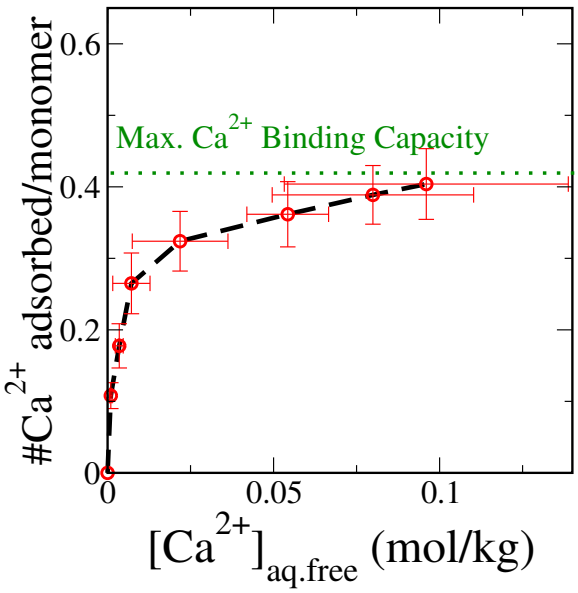

Figure 2.1: Isotherm describing Ca^{2+} ion binding to a polyacrylate chain with 32 repeat units. Error bars represent one standard deviation around the sample mean. Note: The apparent positive slope of the last two data points is a consequence of large uncertainties in determining corresponding solution concentration of free Ca^{2+} in the system. The differences in their vertical axis values are very minimal. (See Figure S8 and accompanying discussion in the Supporting Information.)

We demonstrate this phenomenon in a polyelectrolyte solution corresponding to $Ca^{2+}_{aq.free} = 0.026$ mol/kg. First, we identify the system configuration that corresponds to the polymer chain with the most probable radius of gyration. Then, we independently unbind each of the bound Ca^{2+} ions. We employ the free energy perturbation approach to compute the unbinding free energy, and report the corresponding values in Figure 2.2b.

The unbinding free-energies of the 11 Ca^{2+} ions broadly fall into two classes. We categorize these binding sites into a "low" binding mode ($\leq$ 818 kJ/mol) and "high" binding mode ($>$ 818 kJ/mol). From the binding sites depicted in Figure 2.2a along with the accompanying free energies in Figure 2.2b, we identify that the high binding mode is approximately 5–10 kJ/mol energetically more favorable than the low binding mode and facilitates a Ca^{2+} ion-bridge between non-neighboring carboxylate groups on the polyacrylate chain.

The various binding modes and their coupling to polyelectrolyte conformation could impact the number of Ca^{2+} ions sequestered. We determine a binding mode by tracking the number of carboxylate oxygen atoms that are around a Ca^{2+} ion. From the radial distribution of carboxylate oxygen atoms around

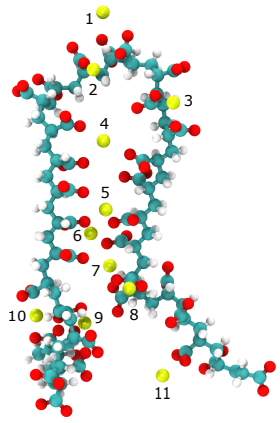

(a)

Label	ΔF [kJ/mol]
1	814 ± 1
2	815 ± 1
3	814 ± 1
4	818 ± 2
5	818 ± 2
6	821 ± 3
7	821 ± 3
8	815 ± 1
9	828 ± 2
10	823 ± 1
11	817 ± 1
Average	818 ± 5

(b)

Figure 2.2: Ca^{2+} ion binding modes to a 32-mer polyacrylate chain. (a) Conformation of a 32-mer polyacrylate chain with the most probable radius of gyration in a solution corresponding to $\left[Ca^{2+}\right]_{\text{aq.free}} = 0.026$ mol/kg and (b) free energies of unbinding a Ca^{2+} ion that is adsorbed to the polyacrylate chain.

a Ca^{2+} ion, we identify that their most probable separation is about 0.35 nm (see Supporting Information). We compute the probability of finding a varying number of carboxylate oxygen atoms within 0.35 nm from a Ca^{2+} ion and report this as a function of $Ca^{2+}_{\text{aq.free}}$ in Figure 2.3.

We observe that the low binding mode, in which two carboxylate oxygen atoms bind to a given Ca^{2+} ion, remains dominant at all concentrations of $Ca^{2+}_{\text{aq.free}}$ studied. However, with an increase in $Ca^{2+}_{\text{aq.free}}$, the high binding mode corresponding to ion-bridging becomes more favorable. Interestingly, when $Ca^{2+}_{\text{aq.free}}$ exceeds 2.18×10^{-2} mol/kg, this trend reverses: further increases in $Ca^{2+}_{\text{aq.free}}$ promote the low binding mode once more. We hypothesize that this non-monotonic trend in the population of different binding modes arises from the enhanced electrostatic screening at higher Ca^{2+} concentrations.

Nevertheless, at moderate and high concentrations of $\left[Ca^{2+}_{\text{aq.free}}\right]$, nearly $\frac{1}{3}$ of the binding events are due to the high binding mode. This high coordination binding environment is seen to have a large impact on the polymer size and

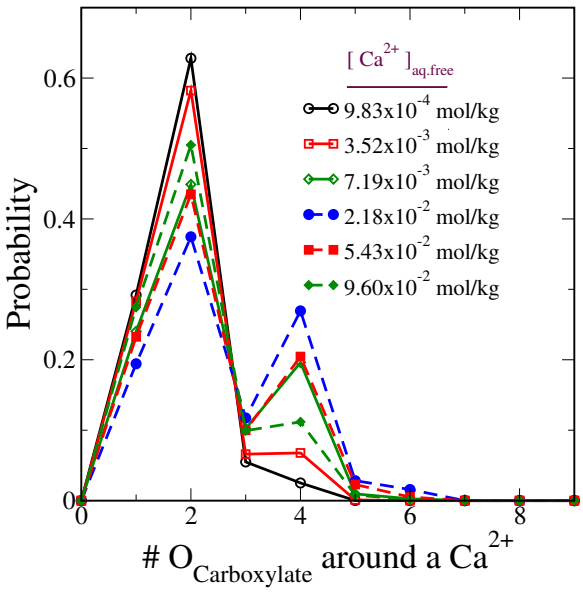

Figure 2.3: Probability of finding certain number of carboxylate oxygen atoms ($O_{Carboxylate}$) on a 32-mer polyacrylate chain around a Ca^{2+} ion.

conformation. We investigate the coupling between the binding modes and the polyelectrolyte chain conformation by tracking the chain radius of gyration (R_g) as a function of $Ca^{2+}_{aq.free}$. We report these results in Figure 2.4.

We note from Figure 2.4(a) that at low concentrations of $Ca^{2+}_{aq.free}$, where the population of the high binding mode is insignificant, the polymer chain adopts an extended conformation with an R_g of approximately 1.65–1.9 nm (Figure 2.4(b)). At these concentrations, Ca^{2+} ions bind to at most one carboxylate group on the polyacrylate chain. As $Ca^{2+}_{aq.free}$ increases and the population of high coordination binding sites subsequently increases, the polymer conformation transitions to a hairpin-like state (Figure 2.4(c)). Here, the high coordination binding sites, which bridge two strands of the polyelectrolyte chain, are nearly as prominent as the low coordination binding sites located on the solvent-exposed side of each strand. Intriguingly, in solutions with high concentrations of Ca^{2+} ions, although some of the bridging events are disrupted, the conformation of a polyelectrolyte chain still resembles that of a hairpin-like state (Figure 2.4(d)). The disruption of the bridging events due to enhanced screening from the other ions in the system increases the conformational flexibility and hence the average chain size.

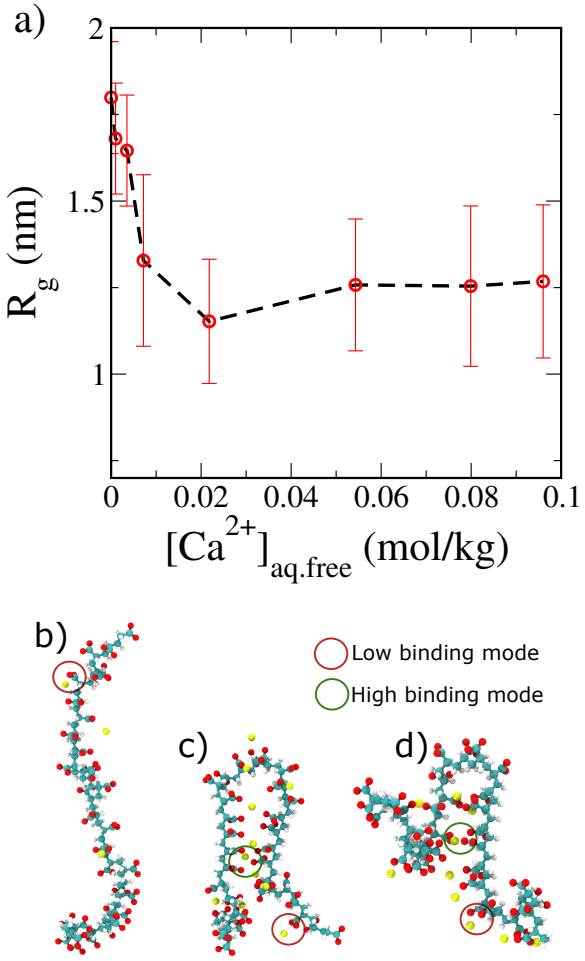

Figure 2.4: Conformational changes in a 32-mer polyacrylate chain due to Ca^{2+} ion. (a) Radius of gyration of 32-mer polyacrylate chain at different concentrations of $\left[Ca^{2+}_{aq.free}\right]$. The large values of standard deviation indicate chain conformational flexibility. Panels (b), (c), and (d) illustrate the dominant binding modes at low, moderate, and high $\left[Ca^{2+}\right]_{aq.free}$ concentrations, respectively. The conformation in panel (c) corresponds to the R_g minimum in panel (a), indicating a hairpin-like compact state of the polyacrylate chain at moderate calcium concentrations.

Since the high coordination binding sites are energetically more favorable, we anticipate that access to a larger population of these binding sites would enhance the ability of a polyelectrolyte chain to sequester Ca^{2+} ions. To explore this, we investigate the inverse problem; we limit the polyelectrolyte chain to only binding sites with low coordination environments and construct the adsorption isotherm. We achieve this by first identifying the polymer conformation that corresponds to the most probable R_g in a system with no added Ca^{2+} ions. Utilizing this chain conformation, with harmonic restraints imposed, we prepare polyelectrolyte solutions with added Ca^{2+} ions. We compute the Ca^{2+} adsorption isotherm from these systems and compare it to that obtained from unrestrained simulations reported earlier. We show these results in Figure 2.5.

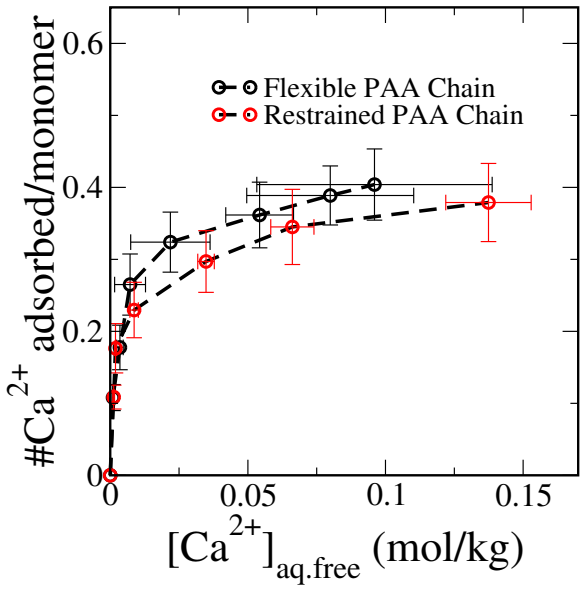

Figure 2.5: Ca^{2+} ion binding isotherm to a polyacrylate chain with 32 repeat units restrained to an extended coil conformation and unrestricted.

We find that at low concentrations, the number of Ca^{2+} ions adsorbed on the polyacrylate chain in both the restrained and unrestrained simulations is indistinguishable. This is because, at lower concentrations of Ca^{2+} ions in the solution, unrestrained polyelectrolyte chains can only access the low coordination binding sites. However, we see a noticeable difference at moderate and high concentrations, where the unrestrained polyacrylate chain favors the high coordination binding sites. The restrained simulations, which do not have access to high binding modes, consistently adsorb fewer Ca^{2+} ions per chain when compared to the unrestrained simulations.

These observations indicate that a polyelectrolyte chain's ability to efficiently chelate Ca^{2+} ions is impacted by its access to a large number of high coordination binding sites. These sites are energetically more favorable for ion binding, and as such, they provide a more stable environment for the ions, leading to a more effective sequestration. This insight could prove useful in applications where selective and efficient ion capture is paramount, such as in water treatment processes or biomedical applications.

2.4 Conclusions

Using all-atom molecular simulations coupled with a free energy perturbation approach, we constructed an adsorption isotherm to describe the binding of Ca^{2+} ions to a model polyacrylate chain. Analysis of the adsorption isotherm revealed that the per-monomer Ca^{2+} ion binding capacity of a fully charged polyelectrolyte chain saturates at a value of 0.40 ± 0.05. This saturation value correlates with the binding modes accessible to Ca^{2+} ions as they bind to the polyelectrolyte chain. Two predominant binding modes were identified: one mode involves Ca^{2+} ions binding to at most two carboxylate oxygen atoms on a polyacrylate chain, and the other involves Ca^{2+} ions binding to four or more carboxylate oxygen atoms.

The population of low binding mode sites remains high across all concentrations of Ca^{2+} in the solution. Nevertheless, at least one-third of the binding events at moderate and high concentrations of Ca^{2+} ions in the solution are defined by the high binding mode events. These binding events, while responsible for enhancing the Ca^{2+} ion binding capacity of a polyelectrolyte chain, also lead to the collapse of the polyelectrolyte chain's conformation to a hairpin-like state. The solution concentration of Ca^{2+} ions corresponding to the conformational transition falls within the range close to the supernatant (polymer-poor) side of the phase behavior reported by Sabbagh *et al.* [24] The adsorption isotherm constructed in this study suggests that, at these concentrations, the hairpin-like polyelectrolyte chain had attained the saturation value of the Ca^{2+} binding capacity.

The collapse of a polyelectrolyte chain into a hairpin-like conformation, with all available binding sites saturated, may indicate the onset of putative phase separation. This observation carries important implications for the chelating capacity of a polyelectrolyte towards Ca^{2+} ions, and consequently, for its

antiscalant activity. Yet, polyelectrolyte-divalent ion complex falling out of equilibrium is inherently a multi-chain problem. In our follow up work [45], we investigate the importance of different binding modes of Ca^{2+}, identified in the current work, on the association between like-charged polyelectrolyes and establish the conditions under which a polyelectrolyte in a divalent salt solution falls out of equilibrium.

2.5 Appendix

Electronic Continuum Corrected Partial Atomic Charges of a Polyacrylate Chain

Our molecular model for the polyacrylate chain is based on the GAFF force field parameters as reported by Mintis *et al.* [46]. In order to account for polarization effects, we apply electronic continuum correction by scaling only the partial charges found in the Mintis *et al.* report by 0.75. As commonly practiced, we leave the corresponding Lennard-Jones interaction parameters untouched.

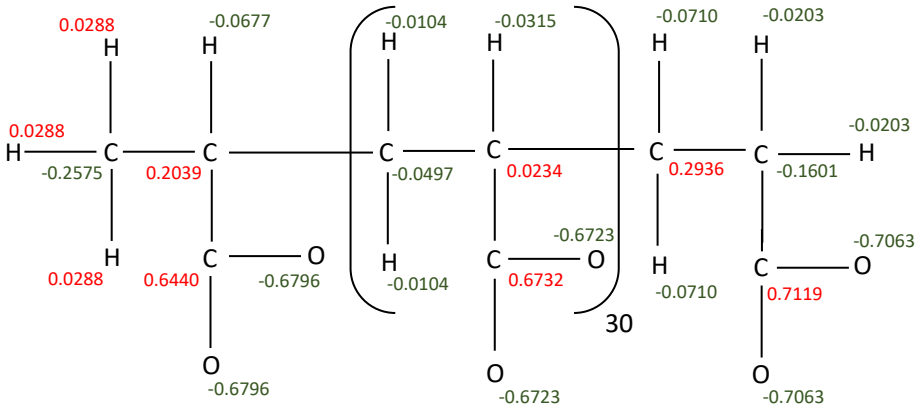

Figure 2.6: Scaled partial charges on all the atoms in a 32-mer polyacrylate.

Overcharging of Polyelectrolyte–Ion Complex in Models with Full Ion Charges

Molecular dynamics simulations, which utilize non-polarizable force fields with "full charge" models for ions, tend to overestimate the binding of dissolved ions to the polyelectrolyte chain. We demonstrate this in Figure 2.7(a) for a fully charged polyacrylate with 32 monomers per chain and sodium ions added to

balance the charge on the polymer, in an aqueous $CaCl_2$ solution. In the figure, we report the net charge of the polyacrylate-ion complex as a function of the number of Ca^{2+} ions in the system. From the radial distribution of Ca^{2+} ions around a backbone carbon on the polyacrylate chain (see Figure 2.7(b)), we identify that the Ca^{2+} ions are most likely to be found at a separation of 0.7 nm from the polymer carbon. We identify all the ions (Ca^{2+}, Na^{+}, Cl^{-}) that are located within 0.7 nm from the polymer backbone and label them as condensed ions. The net charge of the polyacrylate-ion complex is calculated by summing the partial charges of the condensed ions.

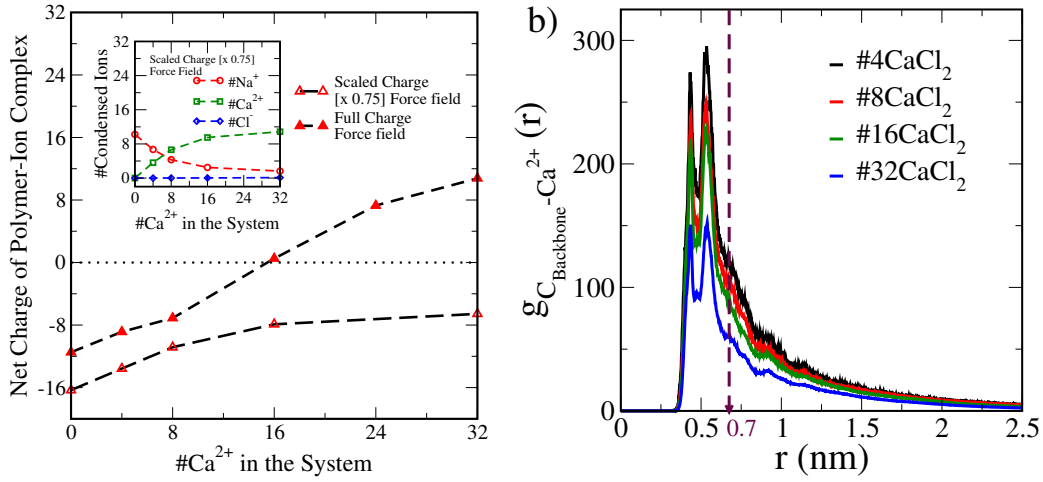

Figure 2.7: Ca^{2+} ion binding number and distribution around a polyacrylate chain. (a) Net charge of a polyelectrolyte-condensed ion complex: a comparison between results from a full charge and scaled charge force field. (b) Radial distribution of Ca^{2+} ions around a backbone carbon on the polyacrylate chain computed from simulations using a scaled charge force field.

We observe from Figure 2.7(a) that simulations with the "full charge" model yield a shift in the net charge of the polyacrylate-ion complex from negative to positive with an increase in Ca^{2+} concentration in the system. In contrast, the "scaled charge" models described in Section 2 predict an increase in the net charge, which eventually plateaus at a negative value for higher Ca^{2+} concentrations. This observation from the "scaled charge" model aligns with recent potentiometric titrations conducted by Gindele *et al.* [9].

Validating Scaled Charge Forcefield for Modeling Polyelectrolyte Conformations

It is not clear beforehand whether the scaled charge-corrected polyacrylate chain spans the desired conformational space. Mintis *et al.* [46] rigorously tested their full charge models against experimentally determined properties of polyacrylate chains in salt-free solutions. We hypothesize that if the scaled charge model for the polyacrylate chain spans the same conformational space, then it will not significantly alter their structural properties. We confirm this observation through the data presented in Figure 2.8.

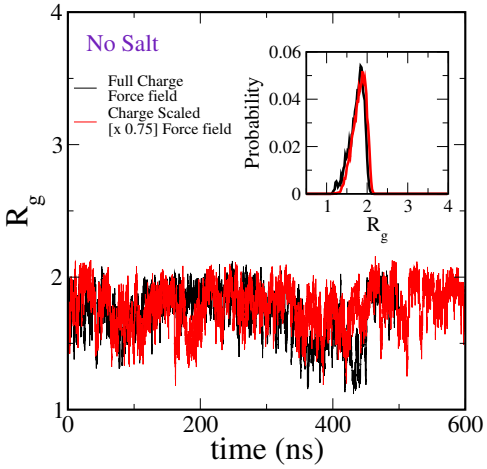

Figure 2.8: Temporal variation of the radius of gyration (R_g) of a polyacrylate chain in an aqueous solution without any added salt.

In the figure, we present the temporal variation of the radius of gyration (R_g) of the polyacrylate chain in a salt-free aqueous solution. We observe that the range of R_g values covered by both the full charge models and the scaled charge models are very similar. This observation is further supported by the R_g probability distribution shown in the inset of the figure.

Meaningful Sampling with Electronic Continuum Correction and Hamiltonian Replica-Exchange Molecular Simulations

Charge scaling has significantly improved the binding/unbinding relaxation times of polyacrylate-Ca^{2+} interactions. Figure 2.9(a) illustrates the decay of the ion-pair survival probability autocorrelation function [80] to zero within the time scales achievable in molecular simulations using modern GPU architecture. However, a trajectory spanning 500 ns proved inadequate for sampling the conformational space with statistical certainty. The temporal variation

of R_g, as reported in Figure 2.9(b), indicates that the conformational space explored by polyelectrolyte chains in an aqueous solution with a concentration equal to or greater than $8CaCl_2$ is not representative of an equilibrium distribution.

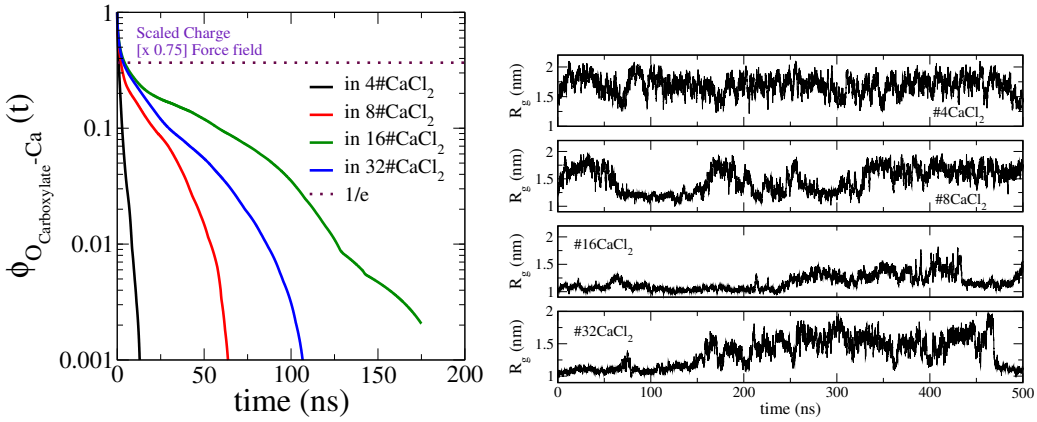

Figure 2.9: Slow relaxation modes of the studied systems. (a) Binding/unbinding relaxation of a carboxylate oxygen–Ca^{2+} ion pair with the scaled charge force field. The function $\phi(t)$ represents the autocorrelation function depicting ion-pair survival probability [80]. (b) Temporal variation of the radius of gyration (R_g) of a polyacrylate chain in an aqueous solution with varying concentrations of $CaCl_2$.

Estimating the required length of a simulation trajectory to generate an equilibrium distribution is challenging. To overcome this issue, we use a Hamiltonian replica Exchange protocol described in Section 2 that specifically biases polyacrylate-Ion interactions in the system. In Figure 2.10, we present the temporal evolution of the radius of gyration of a fully charged PAA-32mer chain at different Ca^{2+} concentrations in the system, computed from the HREMD simulation. A 100 ns trajectory already demonstrates that the simulations have explored many possible chain conformations under given system conditions.

Determining $\left[Ca^{2+}\right]_{aq.free}$ from the Equivalence of $\mu^{system}_{CaCl_2}$ and $\mu^{solution}_{CaCl_2}$

$\left[Ca^{2+}\right]_{aq.free}$ represents the concentration of free Ca^{2+} ions in the solution that are in equilibrium with those adsorbed on a polyacrylate chain. We determined $\left[Ca^{2+}\right]_{aq.free}$ by equating the chemical potential of $CaCl_2$ in the system with the polyacrylate chain ($\mu^{system}_{CaCl_2}$) to the chemical potential without the polyacrylate chain ($\mu^{solution}_{CaCl_2}$). We report these chemical potentials in Figure 2.11 and establish their equivalence conditions.

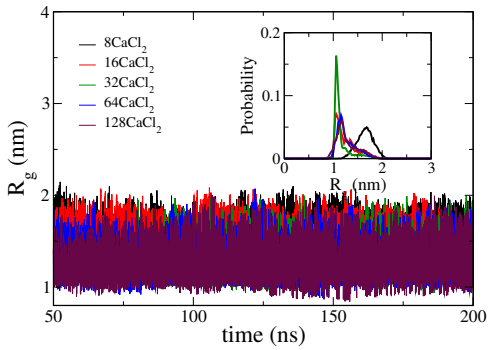

Figure 2.10: Predictions for the radius of gyration (R_g) of a polyacrylate chain in an aqueous solution with varying concentrations of $CaCl_2$, computed using Hamiltonian Replica Exchange simulations with a scaled charge force field.

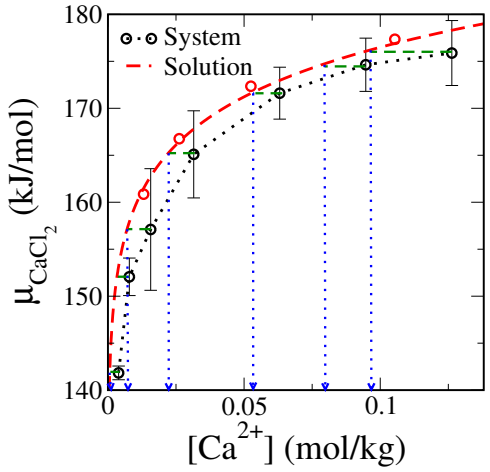

Figure 2.11: The chemical potential of $CaCl_2$ is computed from both the system with the polyacrylate chain and the solution without the polyacrylate chain. The horizontal green dashed lines indicate the equivalence of the $CaCl_2$ chemical potential between the System and the Solution. The vertical blue dotted lines indicate the concentration of free calcium ions in the solution that are in equilibrium with the system of interest.

We note that the lowest $[CaCl_2]_{aq}$, without polyacrylate chain, we simulated in this work is 0.013 mol/kg. As practiced by Pangiotopolous *et al.* [74], we assumed this concentration of $[CaCl_2]_{aq} = 0.013$ mol/kg to be sufficiently low for Debye-Huckle limiting law for electrolyte solutions to hold true. For any concentrations of $[CaCl_2]_{aq} < 0.013$ mol/kg, we used Debye-Huckle limiting law to compute $\mu^{solution}_{CaCl_2}$.

Role of Water in Ca^{2+} Binding to Polyacrylate Chain

Multivalent ions such as Ca^{2+} bear a strong solvation shell. When a Ca^{2+} ion, freely dispersed in the solution, approaches the polyacrylate chain to bind with the carboxylate oxygen on the polymer backbone, a restructuring of the solvation shell is anticipated to facilitate Ca^{2+} binding to the polymer chain.

We find that Ca^{2+} ions bind directly to the carboxylate oxygen, without mediation by water molecules. This is evidenced by the strong first peak in the radial distribution of Ca^{2+} around a carboxylate oxygen located at 0.25 nm (see Figure 2.12(a)). Intriguingly, a free Ca^{2+} sheds about two water molecules as it approaches the polyacrylate chain and binds to a carboxylate oxygen. As illustrated in the Figure 2.12(b), such a phenomenon is invariant to the concentration of Ca^{2+} in the solution. While the corresponding exchange dynamics would facilitate a deeper understanding of the adsorption/desorption of Ca^{2+} from the polymer chain, the HREMD method in our study obscures any real-time dynamics.

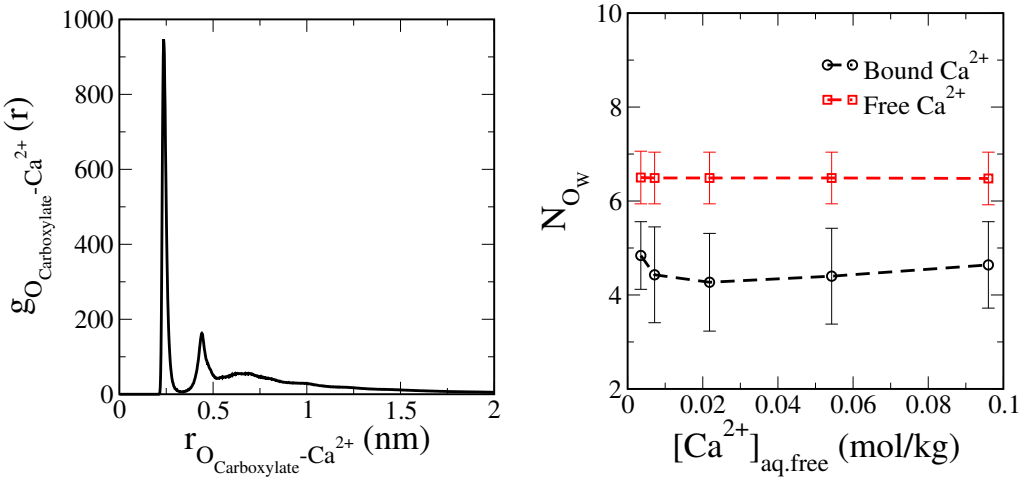

Figure 2.12: The role of water in Ca^{2+} binding to a polyacrylate chain: (a) Radial distribution of Ca^{2+} around a carboxylate oxygen ($O_{Carboxylate}$) on a PAA-32mer in an aqueous solution with $[Ca^{2+}]_{aq.free} = 2.18 \times 10^{-2}$ mol/kg. (b) Number of water oxygens (N_{O_W}) within the first solvation shell of Ca^{2+}. A bound Ca^{2+} ion is defined as one that is bound to any of the carboxylate oxygens. A free Ca^{2+} ion is one that is not bound to a carboxylate and is freely dispersed in the solution.

Additional Notes on Ca^{2+} Adsorption to Polyacrylate Chain

The number of Ca^{2+} ions adsorbed on the PAA chain reaches a saturation value within an error margin at moderate to high concentrations of Ca^{2+} in the system. This becomes evident when we plot the number of Ca^{2+} ions adsorbed on the polyacrylate chain as a function of the number of Ca^{2+} ions added to the system, as demonstrated in Figure 2.13.

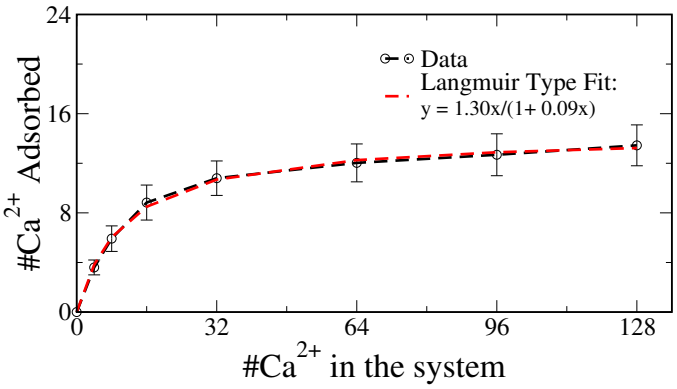

Figure 2.13: Number of Ca^{2+} ions adsorbed on a PAA-32mer as a function of the number of Ca^{2+} ions added to the simulation system. (Note: The fit to the Langmuir model is included only to serve as a visual aid for the saturation in the number of Ca2+ ions adsorbed on a PAA-32mer. It is not intended to indicate the adsorption mechanism.)

The same observation may not be apparent in Figure 2.1, where we plotted the number of Ca^{2+} ions adsorbed per monomer as a function of the solution concentration of Ca^{2+}, due to uncertainties in determining the latter. These uncertainties likely reflect the different binding environments that are accessible for Ca^{2+} binding to the polyelectrolyte chain (and hence their chemical potential), particularly at moderate to high concentrations of Ca^{2+} ions in the solution.

References

1. Antony, A. *et al.* Scale formation and control in high pressure membrane water treatment systems: A review. *Journal of Membrane Science* **383,** 1–16. https://doi.org/10.1016/j.memsci.2011.08.054 (Nov. 2011).

2. Tijing, L. D., Kim, H. Y., Lee, D. H., Kim, C. S. & Cho, Y. I. Physical water treatment using RF electric fields for the mitigation of CaCO3 fouling in cooling water. *International Journal of Heat and Mass Transfer* **53,** 1426–1437. https://doi.org/10.1016/j.ijheatmasstransfer.2009.12.009 (Mar. 2010).

3. Muryanto, S., Bayuseno, A., Ma'mun, H., Usamah, M. & Jotho. Calcium Carbonate Scale Formation in Pipes: Effect of Flow Rates, Temperature, and Malic Acid as Additives on the Mass and Morphology of the Scale. *Procedia Chemistry* **9,** 69–76. https://doi.org/10.1016/j.proche.2014.05.009 (2014).

4. Huang, S.-C., Naka, K. & Chujo, Y. Effect of Molecular Weights of Poly(acrylic acid) on Crystallization of Calcium Carbonate by the Delayed Addition Method. *Polymer Journal* **40,** 154–162. https://doi.org/10.1295/polymj.pj2007162 (Dec. 2007).

5. Sinn, C. G., Dimova, R. & Antonietti, M. Isothermal Titration Calorimetry of the Polyelectrolyte/Water Interaction and Binding of Ca^{2+}: Effects Determining the Quality of Polymeric Scale Inhibitors. *Macromolecules* **37,** 3444–3450. https://doi.org/10.1021/ma030550s (Apr. 2004).

6. Yu, J., Lei, M., Cheng, B. & Zhao, X. Effects of PAA additive and temperature on morphology of calcium carbonate particles. *Journal of Solid State Chemistry* **177,** 681–689. https://doi.org/10.1016/j.jssc.2003.08.017 (Mar. 2004).

7. Aschauer, U., Spagnoli, D., Bowen, P. & Parker, S. C. Growth modification of seeded calcite using carboxylic acids: Atomistic simulations. *Journal of Colloid and Interface Science* **346,** 226–231. https://doi.org/10.1016/j.jcis.2010.02.057 (June 2010).

8. Backer, S., Creamer, M., Pulukkody, R. & Ferrieux, S. Patent number: US20210324304. https://patents.google.com/patent/US20210324304A1/en?oq=US2021-0324304 (2024)(2021).

9. Gindele, M. B., Malaszuk, K. K., Peter, C. & Gebauer, D. On the Binding Mechanisms of Calcium Ions to Polycarboxylates: Effects of Molecular Weight, Side Chain, and Backbone Chemistry. *Langmuir* **38,** 14409–14421 (2022).

10. Reddy, M. M. & Hoch, A. R. Calcite Crystal Growth Rate Inhibition by Polycarboxylic Acids. *Journal of Colloid and Interface Science* **235,** 365–370. https://doi.org/10.1006/jcis.2000.7378 (Mar. 2001).

11. Sparks, D. J. *et al.* Adsorption of poly acrylic acid onto the surface of calcite: An experimental and simulation study. *Physical Chemistry Chemical Physics* **17,** 27357–27365. https://doi.org/10.1039/c5cp00945f (2015).

12. Schweins, R. & Huber, K. Collapse of sodium polyacrylate chains in calcium salt solutions. *The European Physical Journal E* **5,** 117–126. https://doi.org/10.1007/s101890170093 (May 2001).

13. Schweins, R., Lindner, P. & Huber, K. Calcium Induced Shrinking of NaPA Chains: A SANS Investigation of Single Chain Behavior. *Macromolecules* **36,** 9564–9573. https://doi.org/10.1021/ma0347722 (Nov. 2003).

14. Michaeli, I. Ion binding and the formation of insoluble polymethacrylic salts. *Journal of Polymer Science* **48,** 291–299. https://doi.org/10.1002/pol.1960.1204815027 (Dec. 1960).

15. Muthukumar, M. 50th Anniversary Perspective: A Perspective on Polyelectrolyte Solutions. *Macromolecules* **50,** 9528–9560. ISSN: 0024-9297, 1520-5835. https://pubs.acs.org/doi/10.1021/acs.macromol.7b01929 (2022) (Dec. 2017).

16. Schweins, R., Goerigk, G. & Huber, K. Shrinking of anionic polyacrylate coils induced by Ca^{2+}, Sr^{2+} and Ba^{2+}: A combined light scattering and ASAXS study. *The European Physical Journal E* **21,** 99–110. https://doi.org/10.1140/epje/i2006-10047-7 (Oct. 2006).

17. Yethiraj, A. Liquid State Theory of Polyelectrolyte Solutions. *The Journal of Physical Chemistry B* **113,** 1539–1551. https://doi.org/10.1021/jp8069964 (Nov. 2008).

18. Park, S., Zhu, X. & Yethiraj, A. Atomistic Simulations of Dilute Polyelectrolyte Solutions. *The Journal of Physical Chemistry B* **116,** 4319–4327. https://doi.org/10.1021/jp208138t (Apr. 2012).

19. Mantha, S. & Yethiraj, A. Conformational Properties of Sodium Polystyrenesulfonate in Water: Insights from a Coarse-Grained Model with Explicit Solvent. *The Journal of Physical Chemistry B* **119,** 11010–11018. https://doi.org/10.1021/acs.jpcb.5b01700 (June 2015).

20. Chialvo, A. A. & Simonson, J. M. Solvation Behavior of Short-Chain Polystyrene Sulfonate in Aqueous Electrolyte Solutions: A Molecular Dynamics Study. *The Journal of Physical Chemistry B* **109,** 23031–23042. https://doi.org/10.1021/jp053512e (Nov. 2005).

21. Dobrynin, A. V. Effect of Counterion Condensation on Rigidity of Semiflexible Polyelectrolytes. *Macromolecules* **39,** 9519–9527. https://doi.org/10.1021/ma061030a (Dec. 2006).

22. Prabhu, V. M. Counterion structure and dynamics in polyelectrolyte solutions. *Current Opinion in Colloid & Interface Science* **10,** 2–8. https://doi.org/10.1016/j.cocis.2005.04.002 (Aug. 2005).

23. Duan, C. & Wang, R. Association of two polyelectrolytes in salt solutions. *Soft Matter* **18,** 6934–6941. https://doi.org/10.1039/d2sm00839d (2022).

24. Sabbagh, I. & Delsanti, M. Solubility of highly charged anionic polyelectrolytes in presence of multivalent cations: Specific interaction effect. *The European Physical Journal E - Soft Matter* **1,** 75–86. https://doi.org/10.1007/s101890050009 (Jan. 2000).

25. Boisvert, J.-P., Malgat, A., Pochard, I. & Daneault, C. Influence of the counter-ion on the effective charge of polyacrylic acid in dilute condition. *Polymer* **43,** 141–148. https://doi.org/10.1016/s0032-3861(01)00603-6 (Jan. 2002).

26. Fantinel, F., Rieger, J., Molnar, F. & Hübler, P. Complexation of Polyacrylates by Ca^{2+} Ions. Time-Resolved Studies Using Attenuated Total Reflectance Fourier Transform Infrared Dialysis Spectroscopy. *Langmuir* **20,** 2539–2542. https://doi.org/10.1021/la030354e (Mar. 2004).

27. Solis, F. & de la Cruz, M. O. Flexible linear polyelectrolytes in multivalent salt solutions: Solubility conditions. *The European Physical Journal E* **4,** 143–152. https://doi.org/10.1007/s101890170123 (Jan. 2001).

28. Kundagrami, A. & Muthukumar, M. Theory of competitive counterion adsorption on flexible polyelectrolytes: Divalent salts. *The Journal of Chemical Physics* **128,** 244901. https://doi.org/10.1063/1.2940199 (June 2008).

29. Wittmer, J., Johner, A. & Joanny, J. F. Precipitation of Polyelectrolytes in the Presence of Multivalent Salts. *Journal de Physique II* **5,** 635–654. https://doi.org/10.1051/jp2:1995154 (Apr. 1995).

30. De la Cruz, M. O. *et al.* Precipitation of highly charged polyelectrolyte solutions in the presence of multivalent salts. *The Journal of Chemical Physics* **103,** 5781–5791. https://doi.org/10.1063/1.470459 (Oct. 1995).

31. Ermoshkin, A. V. & de la Cruz, M. O. Polyelectrolytes in the Presence of Multivalent Ions: Gelation Versus Segregation. *Physical Review Letters* **90,** 125504. https://doi.org/10.1103/physrevlett.90.125504 (Mar. 2003).

32. Lee, C.-L. & Muthukumar, M. Phase behavior of polyelectrolyte solutions with salt. *The Journal of Chemical Physics* **130,** 024904. https://doi.org/10.1063/1.3054140 (Jan. 2009).

33. Deserno, M., Holm, C. & May, S. Fraction of Condensed Counterions around a Charged Rod: Comparison of Poisson-Boltzmann Theory and Computer Simulations. *Macromolecules* **33,** 199–206. https://doi.org/10.1021/ma990897o (Dec. 1999).

34. Lee, S., Walker, P., Velling, S. & *et al. Molecular Control via Dynamic Bonding Enables Material Responsiveness in Additively Manufactured Metallo-Polyelectrolytes* Research Square, Preprint. Accessed 2024-01-11. Jan. 2024. https://doi.org/10.21203/rs.3.rs-3643582/v1.

35. Liu, S., Ghosh, K. & Muthukumar, M. Polyelectrolyte solutions with added salt: A simulation study. *The Journal of Chemical Physics* **119,** 1813–1823. https://doi.org/10.1063/1.1580109 (July 2003).

36. Zhou, J., Barz, M. & Schmid, F. Complex formation between polyelectrolytes and oppositely charged oligoelectrolytes. *The Journal of Chemical Physics* **144,** 164902. https://doi.org/10.1063/1.4947255 (2016).

37. Kłos, J. & Pakula, T. Monte Carlo simulations of a polyelectrolyte chain with added salt: Effect of temperature and salt valence. *The Journal of Chemical Physics* **123,** 024903. https://doi.org/10.1063/1.1948371 (July 2005).

38. Molnar, F. & Rieger, J. "Like-Charge Attraction" between Anionic Polyelectrolytes: Molecular Dynamics Simulations. *Langmuir* **21,** 786–789. https://doi.org/10.1021/la048057c (Dec. 2004).

39. Yao, G., Zhao, J., Ramisetti, S. B. & Wen, D. Atomistic Molecular Dynamic Simulation of Dilute Poly(acrylic acid) Solution: Effects of Simulation Size Sensitivity and Ionic Strength. *Industrial & Engineering Chemistry Research* **57,** 17129–17141. https://doi.org/10.1021/acs.iecr.8b03549 (Nov. 2018).

40. Sappidi, P. & Natarajan, U. Effect of salt valency and concentration on structure and thermodynamic behavior of anionic polyelectrolyte Na^+-polyethacrylate aqueous solution. *Journal of Molecular Modeling* **22,** 274. https://doi.org/10.1007/s00894-016-3144-4 (Oct. 2016).

41. Patel, K. H., Chockalingam, R. & Natarajan, U. Molecular dynamic simulations study of the effect of salt valency on structure and thermodynamic solvation behaviour of anionic polyacrylate PAA in aqueous solutions. *Molecular Simulation* **43,** 691–705. https://doi.org/10.1080/08927022.2017.1295454 (Mar. 2017).

42. Tribello, G. A., Liew, C. & Parrinello, M. Binding of Calcium and Carbonate to Polyacrylates. *The Journal of Physical Chemistry B* **113,** 7081–7085. https://doi.org/10.1021/jp900283d (Apr. 2009).

43. Chung, Y.-T. & Huang, C.-I. Ion condensation behavior and dynamics of water molecules surrounding the sodium poly(methacrylic acid) chain in water: A molecular dynamics study. *The Journal of Chemical Physics* **136,** 124903. https://doi.org/10.1063/1.3697477 (Mar. 2012).

44. Bulo, R. E. *et al.* Site Binding of Ca^{2+} Ions to Polyacrylates in Water: A Molecular Dynamics Study of Coiling and Aggregation. *Macromolecules* **40,** 3437–3442. https://doi.org/10.1021/ma0624671 (Apr. 2007).

45. Glisman, A. *et al. Multi-valent Ion Mediated Polyelectrolyte Association and Structure* arXiv. Submitted on 2023-11-17. Accessed 2024-02-18. Nov. 2023. https://arxiv.org/abs/2311.10914.

46. Mintis, D. G. & Mavrantzas, V. G. Effect of pH and Molecular Length on the Structure and Dynamics of Short Poly(acrylic acid) in Dilute Solution: Detailed Molecular Dynamics Study. *The Journal of Physical Chemistry B* **123,** 4204–4219 (2019).

47. Duboué-Dijon, E. *et al.* Binding of Divalent Cations to Insulin: Capillary Electrophoresis and Molecular Simulations. *The Journal of Physical Chemistry B* **122,** 5640–5648. https://doi.org/10.1021/acs.jpcb.7b12097 (Jan. 2018).

48. Bedrov, D. *et al.* Molecular Dynamics Simulations of Ionic Liquids and Electrolytes Using Polarizable Force Fields. *Chemical Reviews* **119,** 7940–7995. https://doi.org/10.1021/acs.chemrev.8b00763 (May 2019).

49. Duboué-Dijon, E., Javanainen, M., Delcroix, P., Jungwirth, P. & Martinez-Seara, H. A practical guide to biologically relevant molecular simulations with charge scaling for electronic polarization. *The Journal of Chemical Physics* **153.** https://doi.org/10.1063/5.0017775 (Aug. 2020).

50. Leontyev, I. & Stuchebrukhov, A. Accounting for electronic polarization in non-polarizable force fields. *Physical Chemistry Chemical Physics* **13,** 2613. https://doi.org/10.1039/c0cp01971b (2011).

51. Kirby, B. J. & Jungwirth, P. Charge Scaling Manifesto: A Way of Reconciling the Inherently Macroscopic and Microscopic Natures of Molecular Simulations. *The Journal of Physical Chemistry Letters* **10,** 7531–7536. https://doi.org/10.1021/acs.jpclett.9b02652 (Nov. 2019).

52. Cui, K., Yethiraj, A. & Schmidt, J. R. Influence of Charge Scaling on the Solvation Properties of Ionic Liquid Solutions. *The Journal of Physical Chemistry B* **123,** 9222–9229. https://doi.org/10.1021/acs.jpcb.9b08033 (Oct. 2019).

53. Timr, Š., Kadlec, J., Srb, P., Ollila, O. H. S. & Jungwirth, P. Calcium Sensing by Recoverin: Effect of Protein Conformation on Ion Affinity. *The Journal of Physical Chemistry Letters* **9,** 1613–1619. https://doi.org/10.1021/acs.jpclett.8b00495 (Mar. 2018).

54. Martinek, T. *et al.* Calcium ions in aqueous solutions: Accurate force field description aided by ab initio molecular dynamics and neutron scattering. *The Journal of Chemical Physics* **148,** 222813. https://doi.org/10.1063/1.5006779 (Mar. 2018).

55. Kohagen, M., Mason, P. E. & Jungwirth, P. Accurate Description of Calcium Solvation in Concentrated Aqueous Solutions. *The Journal of Physical Chemistry B* **118,** 7902–7909. https://doi.org/10.1021/jp5005693 (May 2014).

56. Kohagen, M., Lepšík, M. & Jungwirth, P. Calcium Binding to Calmodulin by Molecular Dynamics with Effective Polarization. *The Journal of Physical Chemistry Letters* **5,** 3964–3969. https://doi.org/10.1021/jz502099g (Nov. 2014).

57. Abraham, M. J. *et al.* GROMACS: High performance molecular simulations through multi-level parallelism from laptops to supercomputers. *SoftwareX* **1-2,** 19–25. https://doi.org/10.1016/j.softx.2015.06.001 (Sept. 2015).

58. Spoel, D. V. D. *et al.* GROMACS: Fast, flexible, and free. *Journal of Computational Chemistry* **26,** 1701–1718. https://doi.org/10.1002/jcc.20291 (2005).

59. Berendsen, H., van der Spoel, D. & van Drunen, R. GROMACS: A message-passing parallel molecular dynamics implementation. *Computer Physics Communications* **91,** 43–56. https://doi.org/10.1016/0010-4655(95)00042-e (Sept. 1995).

60. Bonomi, M. *et al.* PLUMED: A portable plugin for free-energy calculations with molecular dynamics. *Computer Physics Communications* **180,** 1961–1972. https://doi.org/10.1016/j.cpc.2009.05.011 (Oct. 2009).

61. Tribello, G. A., Bonomi, M., Branduardi, D., Camilloni, C. & Bussi, G. PLUMED 2: New feathers for an old bird. *Computer Physics Communications* **185,** 604–613. https://doi.org/10.1016/j.cpc.2013.09.018 (Feb. 2014).

62. PlumedConsortium. Promoting transparency and reproducibility in enhanced molecular simulations. *Nature Methods* **16,** 670–673. https://doi.org/10.1038/s41592-019-0506-8 (July 2019).

63. Berendsen, H. J. C., Postma, J. P. M., van Gunsteren, W. F., DiNola, A. & Haak, J. R. Molecular dynamics with coupling to an external bath. *The Journal of Chemical Physics* **81,** 3684–3690. https://doi.org/10.1063/1.448118 (Oct. 1984).

64. Parrinello, M. & Rahman, A. Polymorphic transitions in single crystals: A new molecular dynamics method. *Journal of Applied Physics* **52,** 7182–7190. https://doi.org/10.1063/1.328693 (Dec. 1981).

65. Nosé, S. A unified formulation of the constant temperature molecular dynamics methods. *The Journal of Chemical Physics* **81,** 511–519. https://doi.org/10.1063/1.447334 (July 1984).

66. Hoover, W. G. Canonical dynamics: Equilibrium phase-space distributions. *Physical Review A* **31,** 1695–1697. https://link.aps.org/doi/10.1103/PhysRevA.31.1695 (3 Mar. 1985).

67. Hess, B., Bekker, H., Berendsen, H. J. C. & Fraaije, J. G. E. M. LINCS: A linear constraint solver for molecular simulations. *Journal of Computational Chemistry* **18,** 1463–1472 (Sept. 1997).

68. Darden, T., York, D. & Pedersen, L. Particle mesh Ewald: An $N \log N$) method for Ewald sums in large systems. *The Journal of Chemical Physics* **98,** 10089–10092. https://doi.org/10.1063/1.464397 (June 1993).

69. Essmann, U. *et al.* A smooth particle mesh Ewald method. *The Journal of Chemical Physics* **103,** 8577–8593. https://doi.org/10.1063/1.470117 (Nov. 1995).

70. Wang, L., Friesner, R. A. & Berne, B. J. Replica Exchange with Solute Scaling: A More Efficient Version of Replica Exchange with Solute Tempering (REST2). *The Journal of Physical Chemistry B* **115,** 9431–9438. https://doi.org/10.1021/jp204407d (July 2011).

71. Bussi, G. Hamiltonian replica exchange in GROMACS: A flexible implementation. *Molecular Physics* **112,** 379–384. https://doi.org/10.1080/00268976.2013.824126 (Aug. 2013).

72. Panagiotopoulos, A. Z. Simulations of activities, solubilities, transport properties, and nucleation rates for aqueous electrolyte solutions. *The Journal of Chemical Physics* **153,** 010903. https://doi.org/10.1063/5.0012102 (July 2020).

73. Saravi, S. H. & Panagiotopoulos, A. Z. Activity Coefficients and Solubilities of NaCl in Water–Methanol Solutions from Molecular Dynamics Simulations. *The Journal of Physical Chemistry B* **126,** 2891–2898. https://doi.org/10.1021/acs.jpcb.2c00813 (Apr. 2022).

74. Young, J. M. & Panagiotopoulos, A. Z. System-Size Dependence of Electrolyte Activity Coefficients in Molecular Simulations. *The Journal of Physical Chemistry B* **122,** 3330–3338. https://doi.org/10.1021/acs.jpcb.7b09861 (Jan. 2018).

75. Young, J. M., Tietz, C. & Panagiotopoulos, A. Z. Activity Coefficients and Solubility of $CaCl_2$ from Molecular Simulations. *Journal of Chemical & Engineering Data* **65,** 337–348. https://doi.org/10.1021/acs.jced.9b00688 (Oct. 2019).

76. Chase, M. W. *NIST-JANAF Thermochemical Tables - 4th ed.* Accessed on January 31, 2022. 1998. https://janaf.nist.gov/.

77. Moučka, F., Kolafa, J., Lísal, M. & Smith, W. R. Chemical potentials of alkaline earth metal halide aqueous electrolytes and solubility of their hydrates by molecular simulation: Application to CaCl2, antarcticite, and sinjarite. *The Journal of Chemical Physics* **148,** 222832. https://doi.org/10.1063/1.5024212 (Apr. 2018).

78. Bennett, C. H. Efficient estimation of free energy differences from Monte Carlo data. *Journal of Computational Physics* **22,** 245–268. https://doi.org/10.1016/0021-9991(76)90078-4 (Oct. 1976).

79. Mester, Z. & Panagiotopoulos, A. Z. Mean ionic activity coefficients in aqueous NaCl solutions from molecular dynamics simulations. *The Journal of Chemical Physics* **142,** 044507. https://doi.org/10.1063/1.4906320 (Jan. 2015).

80. Impey, R. W., Madden, P. A. & McDonald, I. R. Hydration and mobility of ions in solution. *The Journal of Physical Chemistry* **87,** 5071–5083. https://doi.org/10.1021/j150643a008 (Dec. 1983).

Chapter 3

MULTI-VALENT ION MEDIATED POLYELECTROLYTE ASSOCIATION AND STRUCTURE

Polyelectrolytes are commonly used to chelate multi-valent ions in aqueous solutions, playing a critical role in water softening and the prevention of mineralization. At sufficient ionic strength, ion-mediated polyelectrolyte–polyelectrolyte interactions can precipitate polyelectrolyte–ion complexes, a phenomenon known as "like-charge attraction." While the significant influence of small ions on polyelectrolyte solution phase behavior is recognized, the precise molecular mechanisms driving the counterintuitive phenomenon remain largely elusive. In this study, we employ all-atom molecular dynamics simulations to investigate the molecular mechanism of like-charge attraction between two poly(acrylic acid) (PAA) chains in solution. We find that moderate quantities of Ca^{2+} ions induce attraction between PAA chains, facilitated by the formation of PAA–Ca^{2+}–PAA bridges and a significant increase in the coordination of Ca^{2+} ions by the PAA chains. At high Ca^{2+} number densities, ion bridges are disfavored due to electrostatic screening, yet the chains are still attracted to each other due to solvent-mediated interactions between the chains and their chelated ions. The insights gleaned from this study not only enrich our understanding of the intricate mechanism of like-charge attraction between polyanions in solution but also illuminate the influence of multi-valent ions on polyelectrolyte interactions.

This chapter includes content from our previously published article:

1. Glisman, A. *et al.* Multi-valent ion-mediated polyelectrolyte association and structure. *Macromolecules* **57,** 1941–1949 (2024).

3.1 Introduction

Aqueous polyelectrolyte (PE) solutions find widespread utility in diverse fields, including water treatment [1], drug delivery [2], and scale ($CaCO_3$) inhibition [3], among others. For many of these applications, it is crucial to manage the behavior of the polyelectrolyte solution phase. By carefully tuning the ionic strength, intriguing phenomena known as "salting out" and "salting in" can be induced, leading to the precipitation or re-dissolution of polyelectrolytes, respectively [4–8]. Therefore, a detailed understanding of the relationship between polyelectrolyte structure and ionic interactions is essential for the systematic design of advanced polyelectrolyte materials and additives.

Polyelectrolytes, such as poly(acrylic acid) (PAA), are commonly used as scale inhibitors due to their ability to chelate Ca^{2+} ions [9, 10] and modify $CaCO_3$ crystal growth [3, 11–13]. The effectiveness of PAA, and other scale inhibitors, relies heavily on the polymer's capacity to simultaneously bind numerous Ca^{2+} ions while preserving polyelectrolyte–ion solubility. Past experimental studies, such as those by Huber [14, 15], have demonstrated that the addition of Ca^{2+} induces a transition in polymer conformation from an extended coil to a collapsed chain, which results in the precipitation of ion-PE complexes once the polymer's binding capacity is exceeded. Subsequent work conducted by Sinn *et al.* [9] found that a screened-Coulomb ion–polyelectrolyte interaction model could not explain the observed precipitation phenomenon, suggesting a more complex understanding of Ca^{2+} mediated interactions is necessary.

Polyelectrolyte theory suggests that a polyelectrolyte's behavior and adsorption properties in solution are strongly tied to the polymer's chain conformation, which in turn is influenced by solution ionic strength and ionic valency [16–22]. Coarse-grained theoretical models have captured the addition of multi-valent ions leading to chain collapse. However, precipitation has been attributed to differing mechanisms, including correlations between chelated ions, ion-bridging between chains, or charge neutralization of the polymer in various studies [23–26]. While theory and experiments predict precipitation of polyelectrolyte-Ca^{2+} complexes at certain conditions, to design novel polyelectrolytes that stay soluble in aqueous solution, we need to understand the molecular principles that govern the Ca^{2+} induced association between like-charged polyelectrolytes. Molecular dynamics (MD) simulations provide a framework for such an investigation.

Several seminal MD studies have investigated the behavior of polyelectrolytes in aqueous $CaCl_2$ solutions. The work of Molnar and Rieger [27] provided evidence for the attraction of polyanions in solution by showing that two PAA chains in a solution were more prone to association as the number of Ca^{2+} ions increased. However, the limited simulation box size (6 nm) and integration time (10 ns) precluded observation of different ion binding environments, polymer conformations, and transitions between states. Subsequent single-chain PAA simulations by the Parrinello group [28, 29] corroborated the stability of ion bridging and hypothesized that interchain ion bridges were responsible for the observed attraction between chains.

While these prior studies have yielded valuable insights, our preceding work [30] underscored a critical limitation: using classical force fields to model electrostatic interactions involving Ca^{2+} without accounting for polarization effects results in exceedingly long Ca^{2+}-PAA relaxation times. Such models can erroneously predict charge inversion of PAA-Ca^{2+} complexes, a phenomenon that is not supported by experimental data [9, 10]. This discrepancy implies that earlier MD investigations concerning Ca^{2+} mediated like-charge interactions suffer from insufficient sampling of PAA-Ca^{2+} populations and polyelectrolyte conformations.

To overcome these challenges, our previous work [30] utilized the Electronic Continuum Correction (ECC) method, modeling the electronic polarization effects in a mean-field manner. This approach enabled us to mirror the polyelectrolyte–ion binding capacities observed in experiments [9, 10]. We also calculated the adsorption isotherm for Ca^{2+} ions on a single PAA chain. The findings showed a transition from an extended coil to a collapsed chain conformation as the number of Ca^{2+} ions increased, a result consistent with experimental observations [10, 14]. We attributed this transition to the formation of intrachain ion bridges which caused a chain collapse. Despite these advancements, there remain unresolved questions. For example, it is unclear how Ca^{2+} ions mediate interchain interactions, and whether the formation of interchain ion bridges constitutes the dominant mechanism driving like-charge attraction between PAA chains in solution.

In the present study, we use our previously validated all-atom MD model to investigate the molecular mechanism of like-charge attraction between two PAA chains in solution. Our enhanced sampling protocol provides an efficient

exploration of the polyelectrolyte conformational space and ion binding environments, enabling the identification of the dominant conformations of PAA chains in solution. We find that at moderate Ca^{2+} numbers, the PAA chains are attracted to each other due to the formation of PAA-Ca^{2+}-PAA bridges between the chains as well as a significant increase in the number of ion and polymer contacts. However, at high Ca^{2+} numbers, ion bridges are disfavored due to electrostatic screening, yet the chains are still attracted to each other mainly due to correlations between the chelated ions on the chains. We then compute the precipitation concentration of PAA in solution using the second osmotic virial coefficient to quantify the net attraction between PAA chains. To analyze the dominant conformations of PAA chains interacting in solution and to investigate potential transition pathways between these conformations, we employ machine learning techniques.

The rest of the manuscript is organized as follows. We first describe our models and specific parameters used in the enhanced sampling algorithms for the molecular dynamics simulations. Next, we report the numerical data obtained from our calculations and discuss their implications. We then conclude the article with an outlook on the path forward for molecular design of antiscalant polyelectrolytes.

3.2 Methods

Molecular Dynamics Simulations. Molecular dynamics simulations were performed using GROMACS (version 2022.3) MD engine [31–33] integrated with PLUMED (version 2.8.1) [34–36]. We studied systems of two 16-mer PAA chains in solution with varying numbers of Ca^{2+} ions. The PAA chains were modeled as atactic and fully deprotonated (pH $\geq$ 11) with Na^{+} counterions, and constructed using CHARMM-GUI [37, 38] with 16 monomers per chain. The PAA chains were then solvated in a 12 nm cubic box of SPC/E water [39] with Packmol [40].

The general AMBER force field (GAFF) [41–43] was employed to model the PAA chains, following the protocol used in our single-chain PAA studies [30] and originally validated by Mintis and Mavrantzas [44]. As electrostatic interactions are known to be overly strong in non-polarizable force fields [45], we utilized the electronic continuum correction (ECC) method [46, 47] to more accurately describe the electrostatic interactions between PAA and Ca^{2+} ions.

The ion parameters for Ca^{2+} and Cl^- were taken from the electronic continuum correction with rescaling (ECCR) parameters of Martinek *et al.* [45], while those for Na^+ were taken from the ECCR optimized parameters of Kohagen *et al.* [48]. It has been shown that scaling polyelectrolyte and small ion charges is required to reproduce experimental binding results accurately [30, 49]. As a result, we applied the ECC method to all PAA partial charges.

For the van der Waals interactions, a cutoff of 1.2 nm was chosen. The long-range electrostatic interactions were calculated via the PME method [50, 51] with a real space cutoff of 1.2 nm. The LINCS algorithm [52] was utilized to constrain all bonds with hydrogen atoms, and the system equations of motion were integrated using the leap-frog algorithm.

After solvation and ion addition, the system was energy-minimized using the steepest descent algorithm for approximately 100,000 steps. The system was then equilibrated in the NVT ensemble at 300 K for 10 ns with 1 fs time steps, using the Nosé–Hoover thermostat [53, 54] with a 0.25 ps relaxation time constant. Further equilibration was carried out for another 10 ns in the NPT ensemble at 300 K and 1 bar using the Parrinello–Rahman barostat [55] with a 5 ps relaxation time constant.

The production phase simulations were conducted in the NVT ensemble at 300 K using a time step of 2 fs. The sampling of the equilibrium ensemble was enhanced by applying a combined well-tempered metadynamics [56–59] and HREMD [60, 61] protocol. The well-tempered metadynamics protocol was used for improved sampling of the two-chain distance free energy surface (FES) [57, 58]. Though metadynamics sampled the two-chain distance effectively, the slow relaxation of the polymer conformations and ion binding environments prevented adequate convergence of the FES. Consequently, we employed the HREMD protocol to efficiently sample the polymer conformational space [62] and ion binding environments [63]. Concurrently, the well-tempered metadynamics protocol was used for improved sampling of the two-chain distance free energy surface (FES) [57, 58].

Coordinate exchanges between replicas were attempted every 100 steps, and the number of replicas was set to ensure an average exchange acceptance rate of approximately 25%. The systems with 0, 8, 16, and 32 Ca^{2+} had 16 replicas, while those with 64 and 128 Ca^{2+} had 24 replicas. In each replica, the elec-

trostatic, Lennard-Jones, and dihedral interactions for all solute atoms were scaled by a parameter λ, ranging from 1 (unbiased) and 0.68 (most biased) geometrically distributed to improve exchange acceptance rates [61].

Each replica contained an independent well-tempered metadynamics bias potential with an initial Gaussian height of 1.2 kJ/mol, Gaussian width of 0.025 nm, deposition stride of 500 steps, and bias factor of 10. The metadynamics biases of each replica were evaluated in the Metropolis coordinate exchange probability. The collective variable (CV) in metadynamics was the distance between the centers of mass of the two PAA chains, facilitating the sampling of various associated and dissociated states. An additional harmonic wall was placed at 6 nm to prevent sampling beyond the minimum image. Replicas were equilibrated for 25 ns at 300 K before production sampling, and the metadynamics bias was added. Each replica simulation was run for at least 250 ns, yielding a total production simulation time of 29.4 μs.

The reported data in our study were collected from the $\lambda = 1$ replica, and statistics were calculated by reweighting this data based on the Boltzmann factor of the metadynamics and harmonic wall biases. Uncertainties, when reported, were estimated using block averaging on correlated MD data to obtain the standard error of the sample mean, which was then converted to 95% confidence intervals. Analysis of the simulation data involved the use of MDAnalysis [64, 65] and custom Python scripts, while VMD [66, 67] was employed for visualizing the generated trajectories.

Stability of Polyelectrolyte Solution. Determination of the solution phase boundary from molecular simulation is non-trivial, as phase transitions are macroscopic events, and the range of system configurational space is large. This boundary typically comprises a polymer-dilute branch and a polymer-rich branch interconnected at the critical concentration, and as shown below, the spinodal of the dilute branch can be estimated with a leading-order expansion of the osmotic virial equation of state. In contrast, the branch corresponding to higher polymer concentrations would require many chain simulations and the enhanced sampling approaches detailed above would become computationally prohibitive. Despite the difference in polymer concentrations and the complexities involved in their prediction, one can anticipate similar key physics and interactions on both branches of the spinodal. This is due to

the fact that precipitation is primarily driven by local interactions between the polymer chains and the ions. Thus, regardless of the concentration, the essential characteristics of these interactions remain the same.

To estimate the spinodal from the simulation data, the primary property of interest from the simulations is the potential of mean force (PMF) between the two PAA chains as a function of the center of mass separation distance. The PMF provides a local measure of the relative stability of associated and dissociated chain configurations. If the PMF at narrow separations is negative, the chains favor association, which may lead to precipitation of the polyelectrolyte at sufficiently high concentrations.

Following previous studies [68–70], we can then calculate the second osmotic virial coefficient as

$$B_2(T) = -2\pi \int_0^\infty dr\, r^2 \left(e^{-\beta U_{\mathrm{PMF}}(r)} - 1\right) \ , \tag{3.1}$$

where r denotes the center of mass distance between the two PAA chains, $\beta = 1/k_B T$, and $U_{\mathrm{PMF}}(r)$ is the PMF obtained from the simulation. As we simulate the system in the canonical ensemble, our potential of mean force as the Helmholtz free energy for the two-chain interaction ($U_{\mathrm{PMF}}(r) = \Delta F(r)$). Rigorously, the PMF should be calculated at fixed chemical potential of the ions, but constant chemical potential simulations are computationally prohibitive for the systems studied here. However, the PMF calculated at fixed number density of ions (canonical ensemble) has been shown to reproduce experimental trends in phase behavior for similar macromolecules with added salt [69].

A positive $B_2(T)$ indicates a repulsive interaction, while a negative $B_2(T)$ indicates an attractive interaction. To calculate the maximum polyelectrolyte density of the suspension before the onset of polyelectrolyte–ion precipitation, we utilized the leading-order term in the virial expansion of the osmotic pressure [71, 72] to find the spinodal of the polyelectrolyte solution as

$$\rho_{\mathrm{PE}} = -\frac{1}{2\, B_2(T)} \quad | \quad B_2(T) < 0 \ . \tag{3.2}$$

The spinodal polyelectrolyte chain concentration allows us to quantitatively determine the effects of Ca^{2+} ions on the polyelectrolyte solution phase behavior and evaluate the emergence of like-charge attraction.

Autoencoder Neural Network. We employed machine learning models to analyze the large amount of simulation data generated and to map the polyelectrolyte conformational space in a low-dimensional representation. Autoencoder (AE) networks, a type of neural network, have emerged as powerful tools in understanding and predicting complex systems. Recent studies have shown successful applications of AE networks in mapping the conformational space of proteins and oligomers [73–76]. An AE network consists of an encoder that maps the input to a lower-dimensional representation and a decoder that reconstructs the original input from the lower-dimensional representation. Both networks are symmetric, containing the same number of layers and neurons. The encoded lower-dimensional representation, known as the latent space, provides a compressed representation of the input data and aids in visualizing the phase space.

In line with the approach proposed by Bandyopadhyay and Mondal [75], we trained the AE network using the pairwise distances between the C_α atoms of the PAA backbone. The encoder was built with three hidden layers comprising 496, 128, and 32 neurons, fully connected with a latent space output of 2 dimensions. The training was conducted over 150 epochs using the Adam optimizer with a learning rate of 0.001 and batches of 256 randomly chosen conformations. We used the mean squared error between the input and output as the loss function and applied an L_2 penalty of 0.00001 for weight regularization. Furthermore, to test the model, 20% of the data was withheld. All aspects of model development and training were facilitated by the PyTorch library [77, 78].

3.3 Results and Discussion

The 16-mer PAA two-chain PMF curves for each number of Ca^{2+} ions ($N_{Ca^{2+}}$) are shown in Figure 3.1. The reference state for each system is the free energy at $r = 4$ nm, where the average two-chain interactions have plateaued for all calcium-containing systems. In the absence of Ca^{2+} ions, the system has repulsive ($\Delta F > 0$) interactions at all distances, as expected. At small numbers of Ca^{2+} ions ($N_{Ca^{2+}} \approx 8$), Ca^{2+} adsorption reduces the long-ranged chain repulsion and a metastable association well emerges at ∼1.2 nm. As $N_{Ca^{2+}}$ increases, the PMF develops a globally stable well at short distances ($r \leq 1.8$ nm) with a large barrier separating the associated and dissociated states. Higher $N_{Ca^{2+}}$ shifts the PMF well to larger distances and the bar-

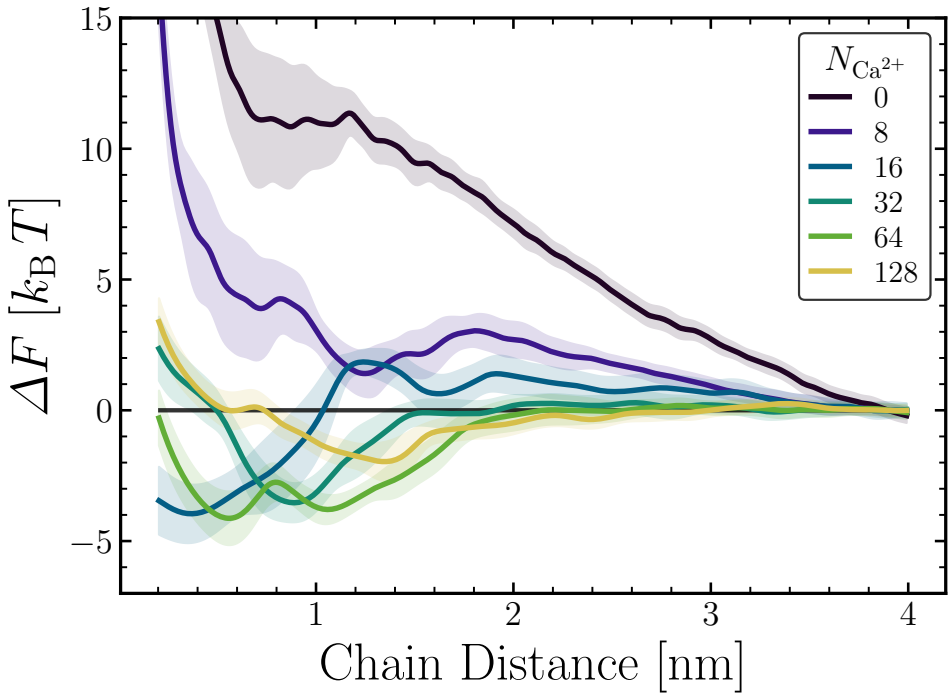

Figure 3.1: Potential of mean force for two 16-mer PAA chains with varying number of Ca^{2+} ions.

rier height vanishes. Increased electrostatic screening at higher $N_{Ca^{2+}}$ reduces the long-ranged repulsion between the chains, and likely contributes to the observed reduction in the barrier height.

We next estimated the precipitation conditions of the polymer–ion complex using the osmotic virial equation of state. The second osmotic virial coefficient (B_2) physically represents the two-body interaction between polymer chains such that a positive B_2 value indicates repulsion, and a negative B_2 value indicates attraction. We calculate B_2 using Eq. 3.1 with the approximation that the infinite integral domain can be replaced with a finite domain of $r \in [0, 6]$ nm, which is appropriate given the short-ranged interactions and the PMF curves plateau, which causes the integrand to vanish. We do not include the $N_{Ca^{2+}} = 0$ system in the calculation of B_2 because the PMF is repulsive at all distances. For systems with net-attraction ($B_2 < 0$), the corresponding maximum polymer concentration at which the polymer–ion complex is predicted to precipitate is calculated using Eq. 3.2 and shown in the inset of Figure 3.2. Interestingly, the system with 16 Ca^{2+} ions exhibits a positive B_2 value, suggesting no precipitation of the polymer–ion complex (to leading

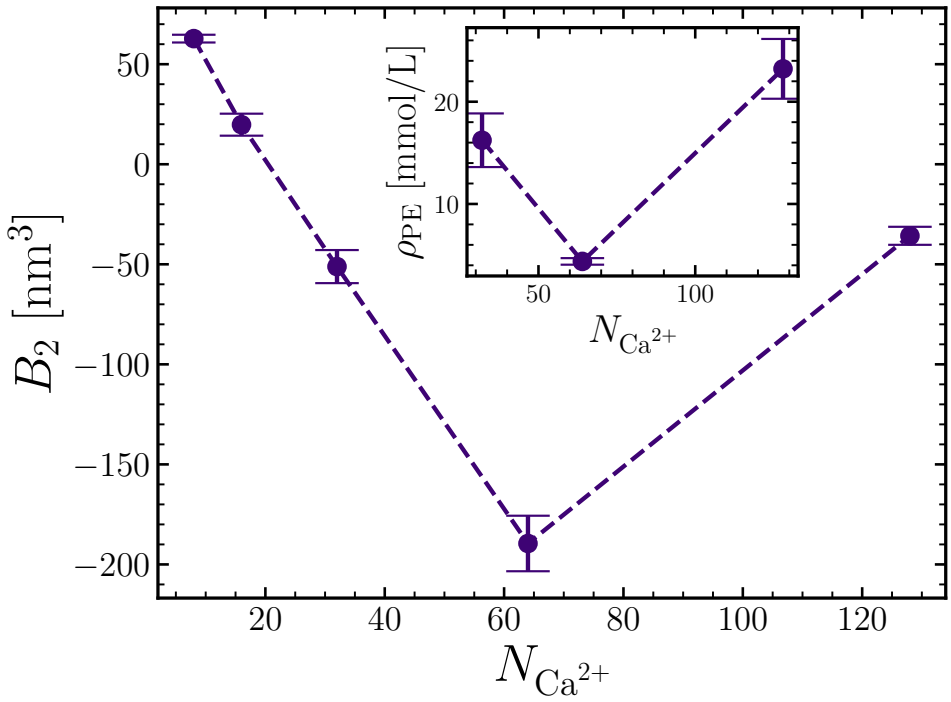

Figure 3.2: PAA second osmotic virial coefficient as a function of Ca^{2+} ions in the system. Inset shows the corresponding polymer concentration at which the polymer–ion complex is predicted to precipitate. The dotted lines are guides to the eye.

order), despite possessing an attractive PMF well of $\sim 4k_B T$. We additionally observe a non-monotonic trend in the second osmotic virial coefficient. This trend results in the spinodal polymer concentration being higher for 128 Ca^{2+} than 64 Ca^{2+}, which implies a salting-in effect.

The non-monotonic behavior of the second osmotic virial coefficient with increasing $N_{Ca^{2+}}$ qualitatively agrees with theoretical predictions of salting-in effects reported by Wittmer *et al.* [25] at higher ionic strengths. However, unlike the theoretical prediction of polymer charge inversion via ion chelation, our simulations did not show such behavior. Instead, the number of calcium ions bound to the polymer increased and saturated below the 16 Ca^{2+} count needed for charge neutrality (see Figure 3.3). The number of calcium ions bound to the two 16-mer PAA chains saturates around 9 ions, which is not enough to neutralize, much less invert, the charge of the polymer. These results are consistent with our single-chain 32-mer PAA simulations [30], which showed that the number of calcium ions bound to the polymer saturates at approximately 0.4 ions per monomer. Experimental studies on longer chains

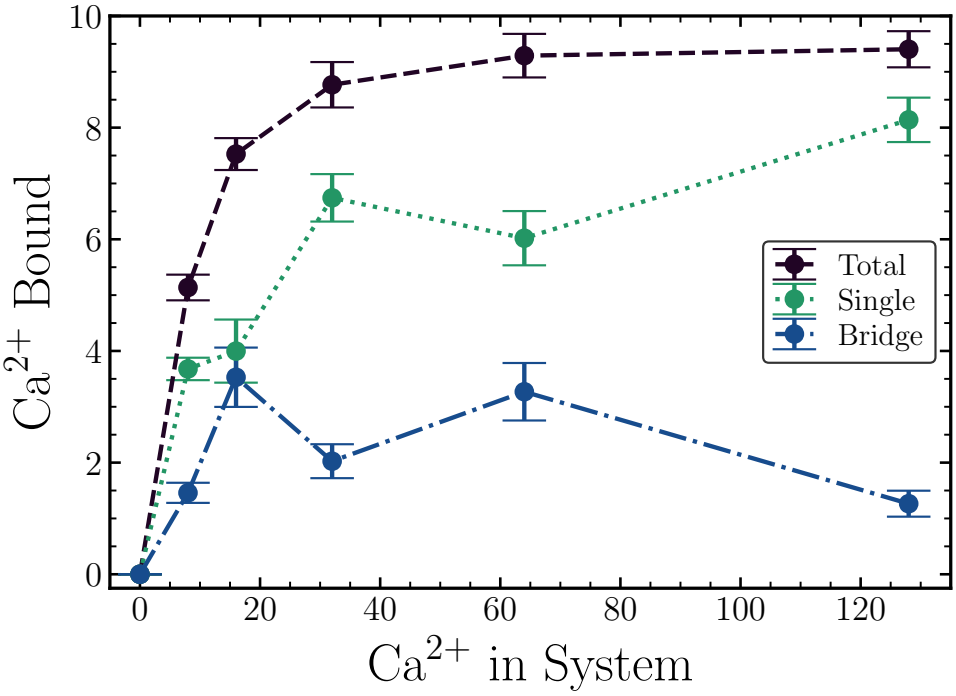

Figure 3.3: Number of calcium ions bound to PAA carboxylate groups as a function of the number of calcium ions in the system. Data are plotted within 1 $k_B T$ of the minimum in the interchain potential of mean force, ensuring the relevance to the system's most stable configurations. Calcium ions bound to a single chain are depicted in green, while bridging ions between chains are shown in blue. The dotted lines are guides to the eye.

have similarly measured a binding capacity of about 0.3 Ca^{2+} per monomer [9, 10]. The sodium counter-ion binding to the polymer is negligible as the calcium ions out-compete the sodium ions for binding sites, as shown in the Supporting Information. At higher sodium ion numbers, the sodium ions may compete with the calcium ions for binding sites. The competition and increase in electrostatic screening may decrease the polyelectrolyte ion binding capacity and would be an interesting future investigation.

At high $N_{Ca^{2+}}$, the electrostatic screening reduces the formation of ion bridges between chains, leading to a slightly weaker and longer-ranged attraction, which is consistent with our single-chain PAA simulations [30] and de la Cruz *et al.* [16]. This phenomenon is the source of the salting-in behavior. The average number of bridging Ca^{2+} ions decreases to just 1 at 128 Ca^{2+} ions, yet the chains are still attracted to each other, as seen in the PMF curves (Figure 3.1). However, the chain-associated state remains favorable due to the

presence of 8 single-chain adsorbed Ca^{2+} ions. These single-chain adsorbed Ca^{2+} are often chelated by a single carboxylate group, which locally inverts the effective monomer charge from -1 to $+1$. The positive charge of the effectively monovalent cation monomer screens the long-ranged chain repulsive interactions and promotes chain association.

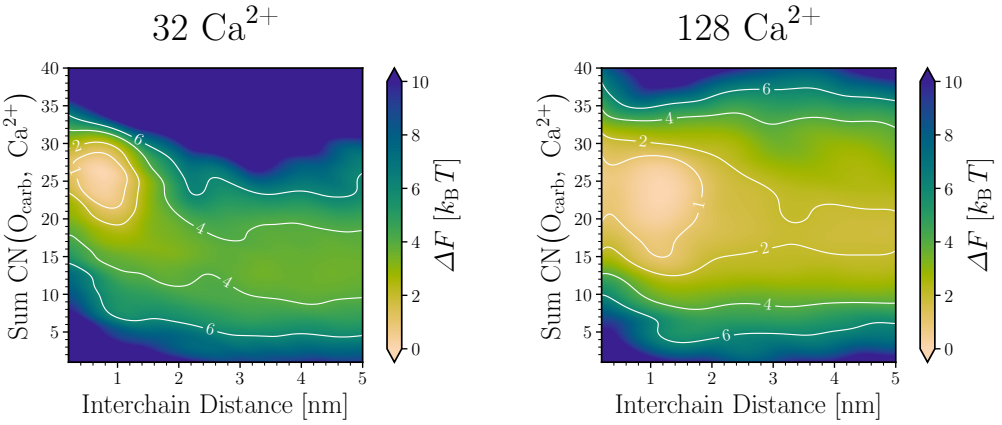

Figure 3.4: Two-dimensional free energy surfaces for two 16-mer PAA chains with 32 (**left panel**) and 128 (**right panel**) Ca^{2+} ions. The horizontal axis represents the center of mass distance between the PAA chains, while the vertical axis denotes the summed coordination number of carboxylate oxygen atoms about Ca^{2+} ions. Isolines are drawn at 1, 2, 4, and 6 $k_B T$.

The depiction of Ca^{2+} adsorption in Figure 3.3 elucidates how Ca^{2+} facilitates the association of PAA chains. However, this representation only shows the structure of associated states and not the overall driving forces propelling the chain association. Our single-chain studies [30] have shown that isolated chains similarly adsorb Ca^{2+} and exhibit intrachain ion bridging. We observe that as the two chains approach one another, the calcium-mediated interactions become more pronounced through both an increase in ion bridging and calcium adsorption, as shown in Figure 3.4.

The above trend can be quantified by evaluating the number of contacts between carboxylate groups and Ca^{2+} ions. We establish a 'contact' when the distance between a carboxylate group and a Ca^{2+} ion falls below 0.35 nm. This cut-off was determined by the location of the first minima in the radial distribution function for Ca^{2+} and carboxylate oxygen atoms. The proximity denotes direct PE–ion interactions, which eliminate solvent-mediated interactions.

Figure 3.4 shows the free energy landscape of PE–ion contacts as a function of the interchain distance for systems with 32 and 128 Ca^{2+} ions, respectively. We focus on these two systems, as 32 Ca^{2+} ions is the minimum number of ions in this study that leads to $B_2 < 0$ and 128 Ca^{2+} ions exhibits non-monotonicity in the B_2 curve (Figure 3.2). For 32 Ca^{2+} ions, the stable associated states have a larger number of PE–ion contacts than the dissociated states. As the chains approach each other, more Ca^{2+} ions adsorb onto the chains due to the higher density of carboxylate groups. This not only decreases the electrostatic repulsion between the chains but also aids in forming ion bridges. However, for 128 Ca^{2+} ions, the chains are already saturated with Ca^{2+} ions in the dissociated states, and so the relative increase in the number of PE–ion contacts is less with further decrease in the interchain distance. In addition, the overall free energy surface (FES) valley is shallower and shifted to larger chain center of mass distances, which is consistent with the decreased number of bridging Ca^{2+} ions (Figure 3.3).

We sought to identify the dominant polymer conformations of the most stable associated states in the 32 Ca^{2+} system that contribute to the two-chain attractive interactions and to explore the relative importance of bridging and single-chain adsorbed Ca^{2+} ions. The full free energy landscape of the polymer conformations is a high-dimensional surface that is difficult to visualize and analyze. Consequently, we wanted to coarse-grain the conformational space into a low-dimensional representation that would facilitate the identification of the dominant conformations through key collective variables (CVs). Physical CVs, such as the radius of gyration or the angle between the principal radius of gyration vectors, proved insufficient to discern the dominant conformations due to the multitude of metastable states and the broad distributions of these variables. As a result, we employed machine learning techniques, specifically an autoencoder (AE), to learn a low-dimensional representation of the conformational space given the pairwise distances between the C_α atoms of the PAA backbone, as described in the Methods section.

Figure 3.5 illustrates the two-dimensional AE latent space projection (z_1, z_2) of the simulation data, which is reweighted by the Boltzmann factor of the metadynamics bias potential and subsequently transformed into a free energy surface. The reference state for the free energy surface was set as the most stable minima within the latent space. Polymer conformations at local minima

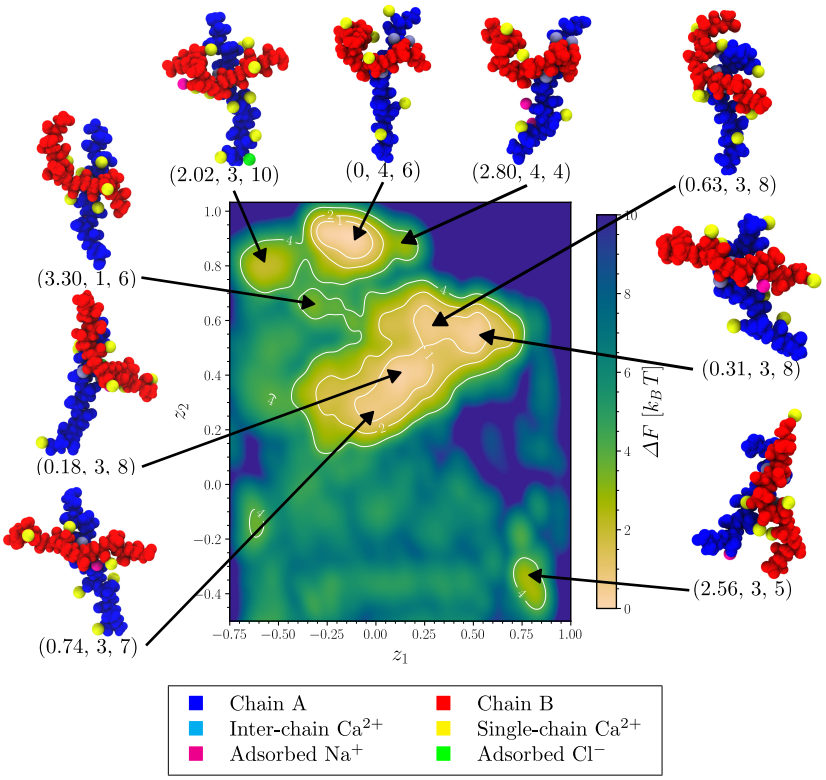

Figure 3.5: Free energy landscape of the autoencoder latent space for two 16-mer PAA chains with 32 Ca^{2+} ions within 1 $k_B T$ of the minimum in the interchain potential of mean force. Chain conformations at relevant minima are visualized, along with ions within 0.35 nm of the chains. The tuple below each conformation displays the corresponding free energy, the number of bridging calcium ions, and the number of single-chain adsorbed calcium ions. Isolines are drawn at 1, 2, and 4 $k_B T$.

in the free energy surface are rendered to visualize the metastable states. The chains are colored to indicate the conformations more clearly, and ions within 0.35 nm of the chains are shown. Water molecules are omitted for clarity. Remarkably, the AE identifies different ion bridging environments without explicit training on the number of bridging ions or their coordinates.

The most stable conformations reside in the upper energy basin and contain 4 bridging Ca^{2+} with 6 single-chain adsorbed Ca^{2+}. Within this arrangement, one of the chains adopts a collapsed conformation (colored red) and is partially wrapped around the other chain, which is in an extended conformation (colored blue). The collapsed chain facilitates the formation of ion bridges with the extended chain, and each chain adsorbs three additional Ca^{2+} ions, which serve to neutralize the polymer charge and mitigate unfavorable carboxylate–carboxylate interactions.

The central energy basin hosts a more diverse set of conformations, stabilized by 3 bridging Ca^{2+} ions. Chains in this region can assume either extended or partially collapsed conformations. The most stable conformation maximizes the number of ion bridges, but interestingly, the AE also identifies conformations with fewer ion bridges that are stabilized by extra single-chain adsorbed Ca^{2+} ions. Both metastable basins at 0.18 and 0.31 $k_B T$ contain 8 single-chain adsorbed Ca^{2+}. Additional frames depict local minima along the transition path between metastable conformations, as well as a possible transition between the basins of 3 and 4 bridging calcium ions.

The basin with 3 bridging calcium ions at 0.74 $k_B T$ contains 7 single-chain adsorbed Ca^{2+} and highlights the relative importance of ion adsorption and bridging at moderate $N_{Ca^{2+}}$. Compared to the minimum free energy conformation observed, the total number of Ca^{2+} on the polyelectrolyte complex is the same in both conformations, but a bridging calcium ion has been replaced by a single-chain adsorbed calcium ion. The 0.74 $k_B T$ basin also has a relatively extended chain conformations, which likely yields an increase in the chain conformational entropy. The loss of the ion bridge has a modest impact on free energy ($< 1\, k_B T$), indicating that the ion bridging does not dominate the free energy landscape. The cost of losing an ion bridge can be further reduced to 0.18 $k_B T$ by the addition of 1 single-chain adsorbed calcium ion.

As seen in Figure 3.3, ion bridges are not dominant at $N_{Ca^{2+}} = 128$. However, the presence of ion bridges does not vanish, as seen in Figure 3.6. The left panel depicts a conformation with 4 ion bridges and the right panel depicts a conformation with no ion bridges that largely interacts through via solvent mediation. Both conformations are within 0.1 $k_B T$ of the minimum in the interchain potential of mean force and are highly populated. However, the majority of conformations in the basin contain low numbers of ion bridges, as the increased electrostatic screening reduces the cost of separating the chains and leads to a slightly longer-ranged interaction well (Figure 3.1). We observe that the increased flexibility of polymer conformations with more Ca^{2+} ions allows for a broader range of conformations, where ion bridges can be destroyed and additional ions adsorbed with almost no free energy difference. The conformational flexibility may play a role in the salting-in behavior, as the chains can relax into conformations that are more favorable for solvation.

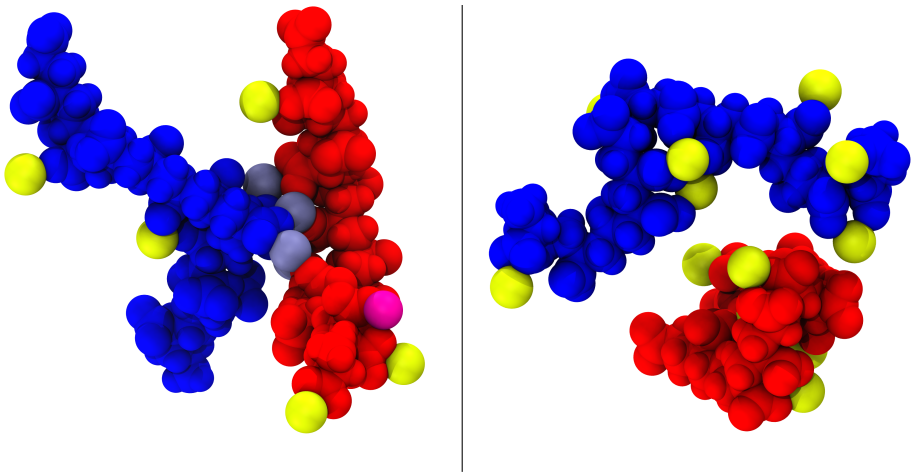

Figure 3.6: Representative conformations of two 16-mer PAA chains with 128 Ca^{2+} ions (within 0.1 $k_B T$ of the minimum in the interchain potential of mean force). The visualization depicts the two PAA chains as dark blue and red, Na^{+} ions as magenta, Ca^{2+} ions as yellow, and interchain bridging Ca^{2+} ions as light blue. **Left panel:** The chains are in direct contact, bridged by 4 Ca^{2+} ions, and have 5 single-chain adsorbed Ca^{2+} ions. **Right panel:** The chains have no bridging Ca^{2+} ions but feature 12 single-chain adsorbed Ca^{2+} ions. Note that the red chain's principal axis is aligned into the page for the right panel.

3.4 Conclusions

This investigation has uncovered the fundamental factors underpinning the like-charge attraction observed within polyanion solutions mediated by multivalent cations. We have found that two primary mechanisms contribute to this phenomenon.

The initial driving force is the increase in the number of favorable polyelectrolyte–ion contacts in chain-associated states when compared to their respective dissociated states (Figure 3.4). At lower Ca^{2+} numbers, these contacts lead to ion bridges between the chains, which are important in setting the length-scale of the attraction. This is manifested in the position of the PMF minima in Figure 3.1.

Our autoencoder analysis revealed that once a sufficient number of ion bridges are formed (3 for the 32 Ca^{2+} system), the free energy difference between forming and breaking additional ion bridges is small compared to thermal energy. Notably, the ion bridge stability is contingent on electrostatic screening, with higher Ca^{2+} numbers rendering these bridges unnecessary for attraction. At high ionic strengths, chains are saturated with Ca^{2+} ions and increases in electrostatic screening decrease the favorability of interchain ion bridges, yet the

chains still experience a net attraction. This attraction remains similar in magnitude even when the relative increase of PE–ion contacts in chain-associated states is less pronounced.

The observed attraction at high Ca^{2+} numbers hints at a second factor driving the attraction: favorable chain–chain interactions that are enabled by the PE–ion contacts on individual chains. We observed that as the two chains approach one another, they increase the number of PE–ion contacts to stabilize the associated chain states.

Our study is consistent with earlier theoretical findings [16, 18–20], which propose that divalent ions can induce chain association. However, we propose that precipitation might not be dominated by ion bridging induced chain collapse or chain neutralization, as generic polyelectrolyte models may suggest. As the number of Ca^{2+} increases, chains are saturated with ions, but the saturated PE–ion complex still carries a net-negative charge (Figure 3.2). At high Ca^{2+} numbers, electrostatic screening decreases the favorability of direct ion bridging, yet the chains still experience a net attraction due to solvent-mediated interactions between the chains and chelated ions.

Our investigation into chain association builds on the previous research of the Parrinello group [28, 29], focusing on longer chains that can accommodate a wider range of Ca^{2+} adsorption environments, such as ions chelated by multiple, non-neighboring monomers. Figure 3.5 illustrates the relative favorability of ion bridging, and our observations show that the most stable associated state arises when at least one of the chains adopts an extended conformation, with ion bridges forming exclusively between chains. Even minor changes in the relative polymer conformations can significantly alter the ion binding environments and the favorability of chain association, as shown in the upper basin of Figure. 3.5.

Experimental studies have shown longer PAA chains precipitate at lower Ca^{2+} concentrations than shorter chains [79]. In our previous single-chain studies [30], we have shown that the conformational flexibility and increased numbers of ion-binding sites of longer chains can increase the favorability of ion chelation by multiple, non-neighboring monomers, which results in the formation of intrachain ion bridges. The intrachain ion bridges increased the chain's ion binding capacity and facilitated cooperative ion binding. We hypothesize that

the same mechanism favoring intrachain ion bridging in isolated chains may also promote interchain ion bridging, which leads to precipitation at lower Ca^{2+} concentrations.

As the simulated PAA chains were fully deprotonated, the model polyelectrolyte acted as a strong polyelectrolyte. As such, we expect that the observed trends in the polyelectrolyte–ion complex precipitation are generalizable to other strong polyelectrolytes of similar side-chain size and charge density. Strong polyelectrolytes, such as poly(vinyl sulfonate) (PVS) and poly(styrene sulfonate) (PSS), have been shown to exhibit similar precipitation behavior [79] with multi-valent cations. The precipitation behavior of PAA at lower pH values, where some of the carboxylate groups are protonated, may be different due to the reduced charge density. The reduced charge density will likely lead to a reduction in the number of Ca^{2+} ions bound to the polymer. Although the fundamental mechanisms driving precipitation remain consistent, variations in specific polymer chemistries and pH can modulate the balance between interchain ion bridging and single-chain ion chelation, thereby influencing the precipitation process.

Looking forward, potential strategies for maintaining aqueous polyelectrolyte solution stability might focus on increasing the solution stability by altering the relative favorability between interchain ion bridging and single-chain ion chelation with solvent-mediated interactions through rational design of the polyelectrolyte. Simple modifications to the polyelectrolyte, such as the introduction of bulky or non-polar side-chains, may curtail the short-ranged ion bridging. At higher ionic strengths, solution stability might be achieved by decreasing the pH to protonate carboxylate groups and subsequently the number of adsorbed ions. The competition between interchain ion bridging and single-chain ion chelation elucidates a more comprehensive understanding of like-charge attractions in polyanion solutions.

3.5 Appendix

GROMACS and PLUMED input files for the simulations described in this chapter are available at `https://github.com/alec-glisman/Simulation-Two-Chain-PAA`. Additional analysis scripts are available at `https://github.com/alec-glisman/Analysis-Two-Chain-PAA`. This manuscript was also deposited to the arXiv preprint server at `https://doi.org/10.48550/arXiv.2311.10914`.

Polyelectrolyte–Ion Structure

In this section, we present additional details on the equilibration and structure of the polyelectrolyte–ion complexes for the 16-mer poly(acrylic acid) (PAA) systems. With the combined Hamiltonian replica exchange and well-tempered metadynamics enhanced sampling methods, we were able to sample the conformational space of the polyelectrolyte–ion complexes and obtain converged free energy surfaces. As replica coordinate exchanges are attempted every 100 steps (0.2 ps), the polymer chain R_g is decorrelated within 0.1 ns of simulation time for all replicas (Figure 3.7). These relaxation time scales do not represent unbiased ensemble dynamics and are meant to highlight how quickly the polyelectrolyte structure equilibrated.

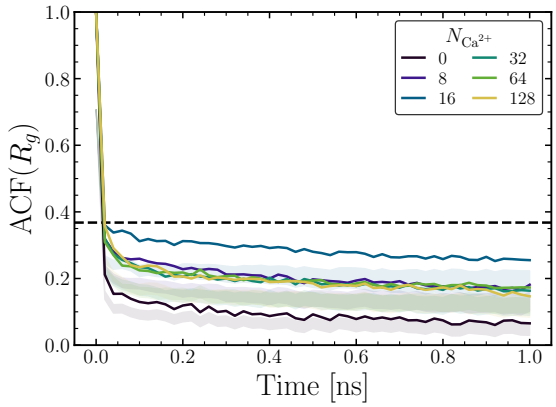

Figure 3.7: Autocorrelation function of the polyelectrolyte chain radius of gyration. The horizontal dashed line is added as a guide to the eye at e^{-1} to estimate the decorrelation time.

The potential of mean force (PMF) curves as a function of the interchain distance shown in the main text are coarse-grained metrics of the interchain interactions and do not provide information about the local structure of the complexes. In Figure 3.8, we present the radial distribution function (RDF) of side-chain carboxylate carbon atoms, denoted C_{cb}, on one chain (A) with respect to C_{cb} atoms on the other chain (B). As the C_{cb} atoms are on the side-chains and directly involved in the ion binding/bridging, they provide a local measure of the interchain interaction distance. The carboxylate carbon RDFs show a well-defined peak at 0.5 nm that is representative of the distance between carboxylate groups bridged by a single Ca^{2+} ion. Notably, the height of this peak shows the same non-monotonic trend as the number of bridging Ca^{2+} ions seen in the main text with increasing Ca^{2+} ions.

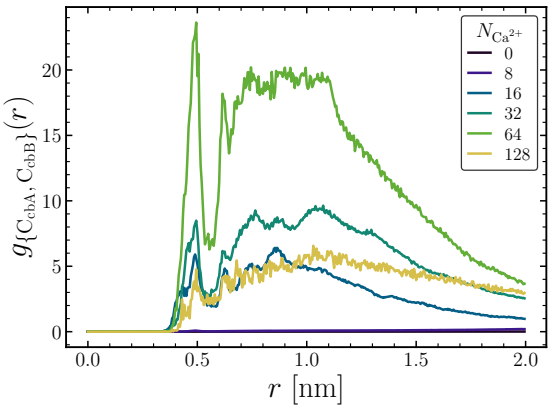

Figure 3.8: RDF of carboxylate carbon (C_{cb}) atoms on one chain with respect to carboxylate carbon atoms on the other chain.

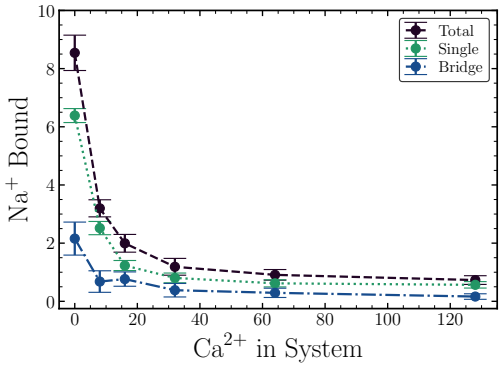

Figure 3.9: Number of sodium ions bound to PAA carboxylate groups as a function of the number of calcium ions in the system. Data plotted within 1 k_BT of the minimum in the interchain potential of mean force. Ions bound to a single chain are green, and bridging ions are blue. The 0 Ca^{2+} data comes from associated states where the interchain distance was less than 2 nm, as the PMF was repulsive at all distances. The dotted lines are guides to the eye.

Ca^{2+} outcompete Na^+ for binding to the carboxylate groups, and the number of Na^+ bound to the carboxylate groups decreases with increasing Ca^{2+}, as shown in Figure 3.9. Even at high Ca^{2+} numbers, one Na^+ remains bound to the polyelectrolyte–ion complex on average and does not contribute significantly to the ion bridging behavior.

Further RDFs illustrating the ion binding to carboxylate carbons and oxygens (O_{cb}) are shown in Figures 3.10 and 3.11. Two dominant peaks are observed about carboxylate carbon atoms corresponding to bidentate and monodentate chelation, respectively.

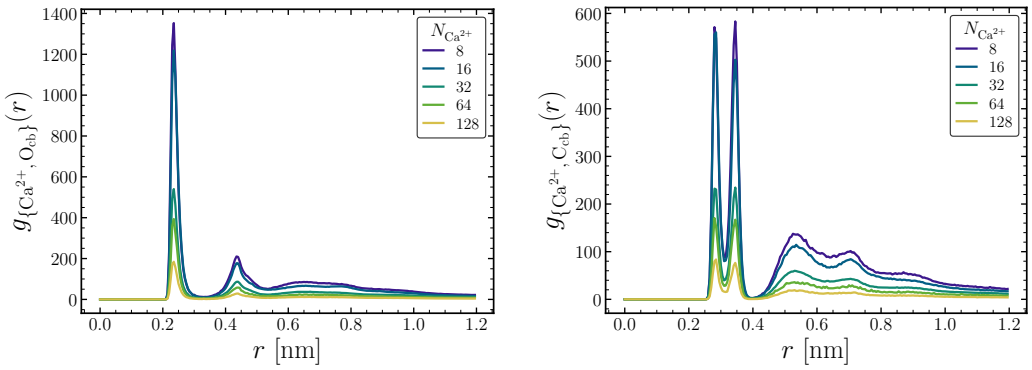

Figure 3.10: RDF of calcium ions about the polyelectrolyte. **Left panel:** RDF of calcium ions around carboxylate oxygen atoms. **Right panel:** RDF of calcium ions around carboxylate carbon atoms.

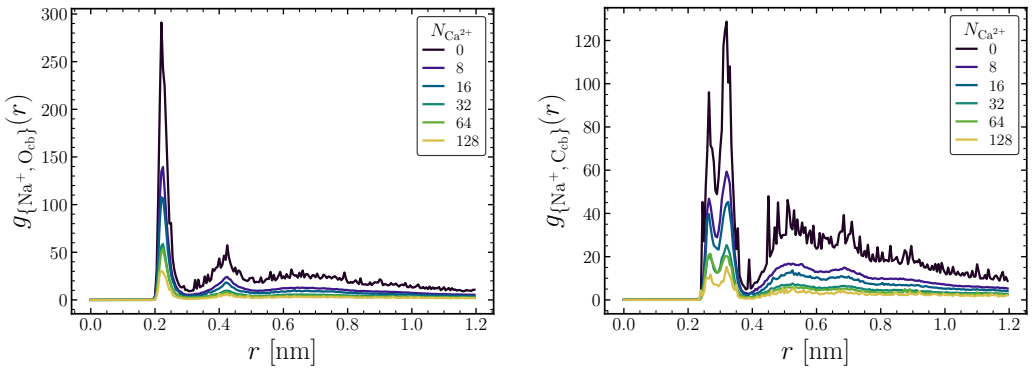

Figure 3.11: RDF of sodium ions around the polyelectrolyte. **Left panel:** RDF of sodium ions around carboxylate oxygen atoms. **Right panel:** RDF of sodium ions around carboxylate carbon atoms.

Additional Free Energy Surfaces

We show the free energy surfaces for the number of calcium and carboxylate oxygen contacts as a function of the interchain center of mass distance for systems not shown in the main text in Figure 3.4. The 8 Ca^{2+} system favors dissociated chain states, as there are not enough Ca^{2+} ions to form sufficient numbers of polymer–ion contacts to stabilize the two-chain complex. The 16 and 64 Ca^{2+} systems exhibit a qualitatively similar free energy surface to the 32 Ca^{2+} system in the main text.

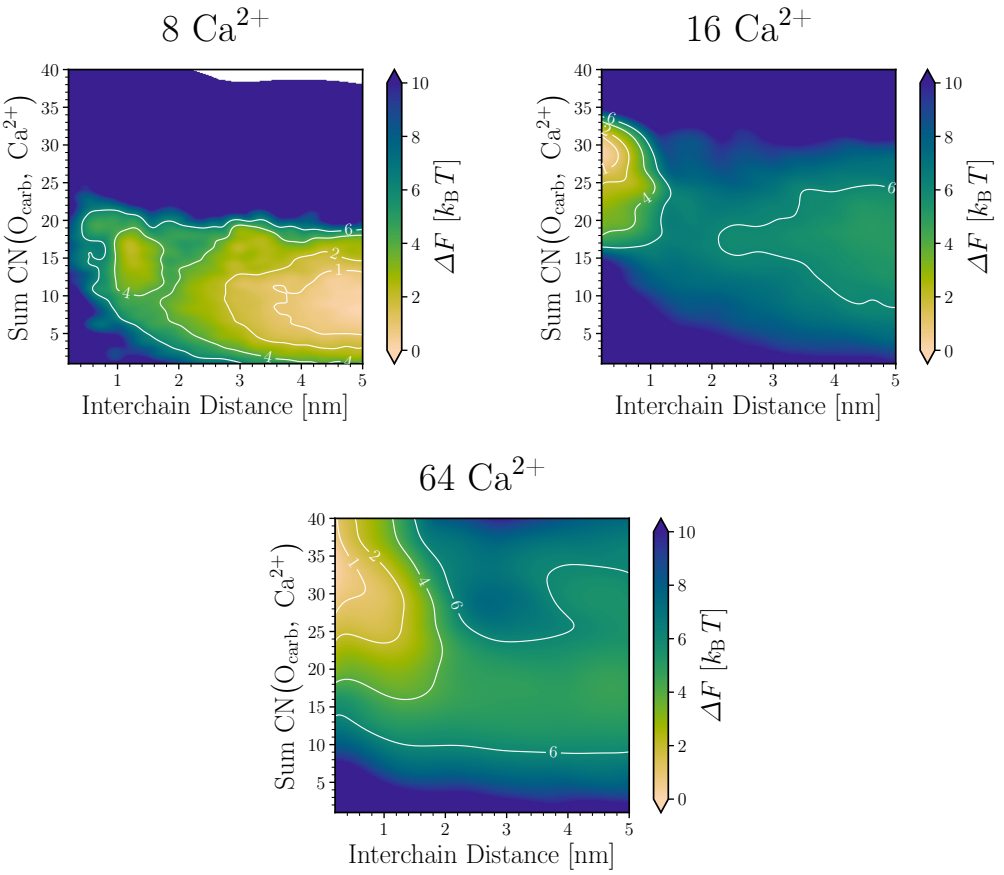

Figure 3.12: Two-dimensional free energy surfaces for two 16-mer PAA chains with 8 (**upper left panel**), 16 (**upper right panel**), and 64 (**bottom panel**) Ca^{2+} ions. The horizontal axis denotes the chain center of mass distance, and the vertical axis denotes the summed coordination number of carboxylate oxygen atoms around Ca^{2+} ions. Isolines are drawn at 1, 2, 4, and 6 k_BT.

Autoencoder

As discussed in the main text, the input data to the autoencoder (AE) consisted of the pairwise distances between all backbone C_α atoms for the 32 Ca^{2+} system. We further restricted the input data to frames where the interchain distance was within 1 k_BT of the minimum in the interchain PMF to focus on the dominant conformational states. The distances were then scaled to the range $[0, 1]$ to improve the training of the AE. Our autoencoder (AE) architecture consisted of an encoder and a decoder connected by a latent space. The encoder consisted of 3 fully connected hidden layers of 496, 128, and 32 neurons, respectively, with hyperbolic tangent activation functions. The decoder

was a mirror image of the encoder with the same number of layers and neurons but had an additional output layer with sigmoid activation to scale the output to the range $[0, 1]$. Weights were initialized with the Xavier uniform initializer.

We determined the optimal latent space by minimizing the reconstruction error of the AE with a fixed latent space dimension of 2 for visualization purposes. The training dynamics of the AE, represented by the loss function during the training process, are shown in Figure 3.13. The loss function converges during training, indicating successful learning and feature extraction.

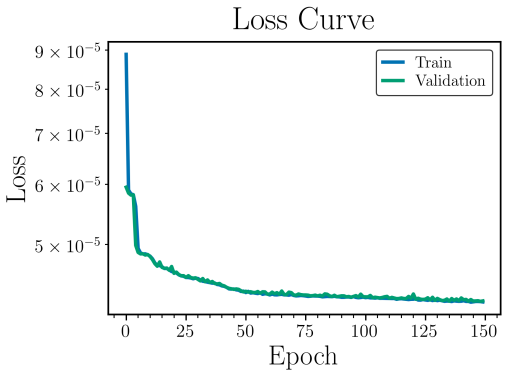

Figure 3.13: The loss function of the autoencoder during training.

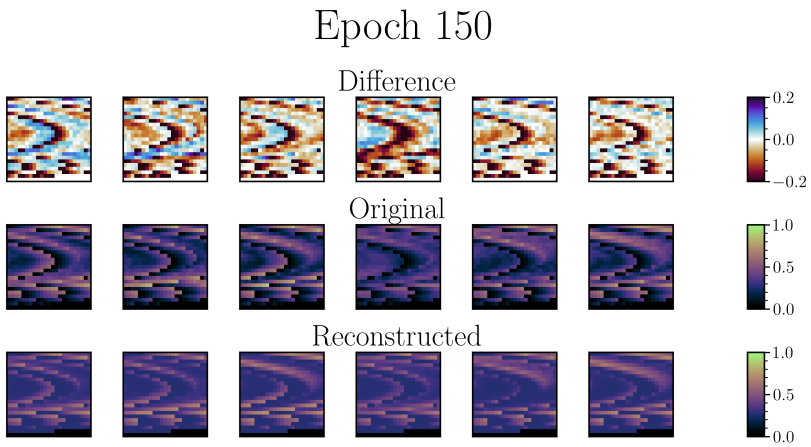

Figure 3.14: The performance of the autoencoder on a set of 6 randomly selected conformations. **Top panel:** Difference between the input and output of the AE for the pairwise distance between all backbone alpha carbons. **Middle panel:** Scaled input features to the AE. **Bottom panel:** Reconstructed features from the latent space.

Figure 3.14 provides a visual representation of the AE's performance on a set of 6 randomly selected conformations. The top panel illustrates the difference between the scaled input data and the reconstructed output of the AE. The middle panel displays the scaled input features to the AE, while the bottom panel presents the reconstructed features from the latent space, showcasing the capability of the AE to capture important features of the input data.

To gain insight into the relationships between the latent space features and relevant physical quantities influencing the conformational space, we analyzed the linear correlation between a few selected variables in Figure 3.15. The latent space features exhibit weak correlations with each other, implying that they capture distinct and complementary aspects of the system. This observation suggests that the autoencoder effectively performs dimensionality reduction and representation learning, allowing it to extract relevant features while preserving important information about the system. The moderate correlation with polymer radii of gyration is consistent with our previous single-chain studies, highlighting the significance of polymer size in determining calcium adsorption behavior. The relatively weak correlation with interchain distance is attributed to the input data restriction of conformations within 1 $k_{\mathrm{B}}T$ of the minimum in the interchain PMF (0.70–1.07 nm), focusing on specific conformational states near the minimum.

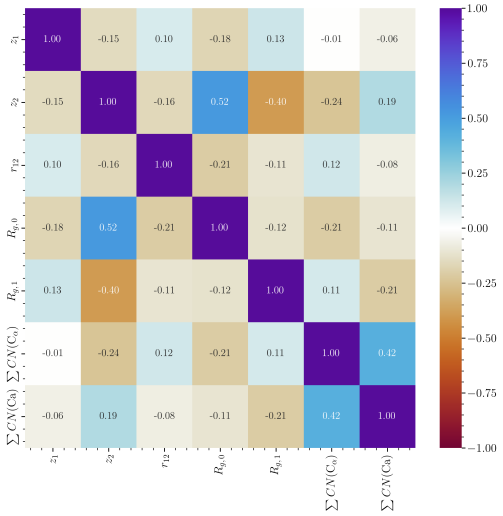

Figure 3.15: The correlation matrix of the latent space features z_i with physical features of interest for the 16-mer PAA chains with 32 calcium ions within 1 k_BT of the minimum in the interchain PMF. The physical features are the interchain distance r_{12}, the chain radius of gyration R_g, the total number of contacts between C_α atoms, and the total number of contacts between Ca^{2+} ions and carboxylate carbons, respectively.

References

1. Bolto, B. & Gregory, J. Organic polyelectrolytes in water treatment. *Water Research* **41,** 2301–2324 (2007).

2. Lankalapalli, S. & Kolapalli, V. Polyelectrolyte complexes: A review of their applicability in drug delivery technology. *Indian Journal of Pharmaceutical Sciences* **71,** 481 (2009).

3. Reddy, M. M. & Hoch, A. R. Calcite crystal growth rate inhibition by polycarboxylic acids. *Journal of Colloid and Interface Science* **235.** Publisher: Academic Press Inc., 365–370. ISSN: 00219797 (Mar. 2001).

4. Arakawa, T. & Timasheff, S. N. Mechanism of protein salting in and salting out by divalent cation salts: Balance between hydration and salt binding. *Biochemistry* **23,** 5912–5923 (1984).

5. Allahyarov, E., D'Amico, I. & Löwen, H. Attraction between Like-Charged Macroions by Coulomb Depletion. *Physical Review Letters* **81,** 1334–1337. ISSN: 0031-9007, 1079-7114. `https://link.aps.org/doi/10.1103/PhysRevLett.81.1334` (2023) (Aug. 1998).

6. Curtis, R. A., Ulrich, J., Montaser, A., Prausnitz, J. M. & Blanch, H. W. Protein-protein interactions in concentrated electrolyte solutions. *Biotechnology and Bioengineering* **79,** 367–380. ISSN: 0006-3592, 1097-0290. `https://onlinelibrary.wiley.com/doi/10.1002/bit.10342` (2023) (Aug. 2002).

7. Saluja, A. *et al.* Anion Binding Mediated Precipitation of a Peptibody. *Pharmaceutical Research* **26,** 152. ISSN: 0724-8741, 1573-904X. http://link.springer.com/10.1007/s11095-008-9722-0 (2023) (Jan. 2009).

8. Li, Y., Girard, M., Shen, M., Millan, J. A. & Olvera De La Cruz, M. Strong attractions and repulsions mediated by monovalent salts. *Proceedings of the National Academy of Sciences of the United States of America* **114,** 11838–11843. ISSN: 0027-8424, 1091-6490. https://pnas.org/doi/full/10.1073/pnas.1713168114 (2023) (Nov. 2017).

9. Sinn, C. G., Dimova, R. & Antonietti, M. Isothermal Titration Calorimetry of the Polyelectrolyte/Water Interaction and Binding of Ca^{2+}: Effects Determining the Quality of Polymeric Scale Inhibitors. *Macromolecules* **37,** 3444–3450. ISSN: 0024-9297, 1520-5835. https://pubs.acs.org/doi/10.1021/ma030550s (2022) (May 2004).

10. Gindele, M. B., Malaszuk, K. K., Peter, C. & Gebauer, D. On the Binding Mechanisms of Calcium Ions to Polycarboxylates: Effects of Molecular Weight, Side Chain, and Backbone Chemistry. *Langmuir* **38,** 14409–14421. ISSN: 0743-7463, 1520-5827. https://pubs.acs.org/doi/10.1021/acs.langmuir.2c01662 (2022) (Nov. 2022).

11. Yu, J., Lei, M., Cheng, B. & Zhao, X. Effects of PAA additive and temperature on morphology of calcium carbonate particles. *Journal of Solid State Chemistry* **177,** 681–689. ISSN: 00224596 (Mar. 2004).

12. Jada, A., Ait Akbour, R., Jacquemet, C., Suau, J. & Guerret, O. Effect of sodium polyacrylate molecular weight on the crystallogenesis of calcium carbonate. *Journal of Crystal Growth* **306,** 373–382. ISSN: 00220248. https://linkinghub.elsevier.com/retrieve/pii/S0022024807005325 (2022) (Aug. 2007).

13. Aschauer, U., Spagnoli, D., Bowen, P. & Parker, S. C. Growth modification of seeded calcite using carboxylic acids: Atomistic simulations. *Journal of Colloid and Interface Science* **346,** 226–231. ISSN: 00219797. https://linkinghub.elsevier.com/retrieve/pii/S0021979710002614 (2022) (2010).

14. Huber, K. Calcium-induced shrinking of polyacrylate chains in aqueous solution. *The Journal of Physical Chemistry* **97,** 9825–9830 (1993).

15. Schweins, R. & Huber, K. Collapse of sodium polyacrylate chains in calcium salt solutions. *European Physical Journal E* **5,** 117–126 (2001).

16. De La Cruz, M. O. *et al.* Precipitation of highly charged polyelectrolyte solutions in the presence of multivalent salts. *The Journal of Chemical Physics* **103,** 5781–5791. ISSN: 0021-9606, 1089-7690. https://pubs.aip.org/jcp/article/103/13/5781/293715/Precipitation-of-highly-charged-polyelectrolyte (2023) (Oct. 1995).

17. Castelnovo, M., Sens, P. & Joanny, J.-F. Charge distribution on annealed polyelectrolytes. *European Physical Journal E* **1,** 115–125. ISSN: 1292-8941. http://link.springer.com/10.1007/PL00014591 (2022) (Feb. 2000).

18. Huang, C.-I. & Olvera de La Cruz, M. Polyelectrolytes in multivalent salt solutions: Monomolecular versus multimolecular aggregation. *Macromolecules* **35,** 976–986 (2002).

19. Liu, S., Ghosh, K. & Muthukumar, M. Polyelectrolyte solutions with added salt: A simulation study. *The Journal of Chemical Physics* **119,** 1813–1823 (2003).

20. Kundagrami, A. & Muthukumar, M. Theory of competitive counterion adsorption on flexible polyelectrolytes: Divalent salts. *The Journal of Chemical Physics* **128** (2008).

21. Lee, C.-L. & Muthukumar, M. Phase behavior of polyelectrolyte solutions with salt. *The Journal of Chemical Physics* **130** (2009).

22. Muthukumar, M. 50th Anniversary Perspective: A Perspective on Polyelectrolyte Solutions. *Macromolecules* **50,** 9528–9560. ISSN: 0024-9297, 1520-5835. https://pubs.acs.org/doi/10.1021/acs.macromol.7b01929 (2022) (Dec. 2017).

23. Ha, B.-Y. & Liu, A. J. Counterion-Mediated Attraction between Two Like-Charged Rods. *Physical Review Letters* **79,** 1289–1292. ISSN: 0031-9007, 1079-7114. https://link.aps.org/doi/10.1103/PhysRevLett.79.1289 (2023) (Aug. 1997).

24. Arenzon, J., Stilck, J. & Levin, Y. Simple model for attraction between like-charged polyions. *European Physical Journal B* **12,** 79–82. ISSN: 1434-6028. http://link.springer.com/10.1007/s100510050980 (2023) (Oct. 1999).

25. Wittmer, J., Johner, A. & Joanny, J. F. Precipitation of Polyelectrolytes in the Presence of Multivalent Salts. *Journal de Physique II* **5,** 635–654. ISSN: 1155-4312, 1286-4870. http://www.edpsciences.org/10.1051/jp2:1995154 (2023) (Apr. 1995).

26. Solis, F. J. & De La Cruz, M. O. Collapse of flexible polyelectrolytes in multivalent salt solutions. *The Journal of Chemical Physics* **112,** 2030–2035 (2000).

27. Molnar, F. & Rieger, J. "Like-Charge Attraction" between Anionic Polyelectrolytes: Molecular Dynamics Simulations. *Langmuir* **21,** 786–789. ISSN: 0743-7463, 1520-5827. https://pubs.acs.org/doi/10.1021/la048057c (2023) (Jan. 2005).

28. Bulo, R. E. *et al.* "Site Binding" of Ca^{2+} Ions to Polyacrylates in Water: A Molecular Dynamics Study of Coiling and Aggregation. *Macromolecules* **40,** 3437–3442. ISSN: 0024-9297, 1520-5835. `https://pubs.acs.org/doi/10.1021/ma0624671` (2022) (May 2007).

29. Tribello, G. A., Liew, C. & Parrinello, M. Binding of Calcium and Carbonate to Polyacrylates. *The Journal of Physical Chemistry B* **113,** 7081–7085. ISSN: 1520-6106, 1520-5207. `https://pubs.acs.org/doi/10.1021/jp900283d` (2022) (May 2009).

30. Glisman, A. *et al.* Adsorption isotherm and mechanism of Ca^{2+} binding to polyelectrolyte. *arXiv preprint arXiv:2311.11404* (2023).

31. Berendsen, H. J., van der Spoel, D. & van Drunen, R. GROMACS: A message-passing parallel molecular dynamics implementation. *Computer Physics Communications* **91,** 43–56 (1995).

32. Van Der Spoel, D. *et al.* GROMACS: Fast, flexible, and free. *Journal of Computational Chemistry* **26,** 1701–1718 (2005).

33. Abraham, M. J. *et al.* GROMACS: High performance molecular simulations through multi-level parallelism from laptops to supercomputers. *SoftwareX* **1,** 19–25 (2015).

34. Bonomi, M. *et al.* PLUMED: A portable plugin for free-energy calculations with molecular dynamics. *Computer Physics Communications* **180,** 1961–1972 (2009).

35. Tribello, G. A., Bonomi, M., Branduardi, D., Camilloni, C. & Bussi, G. PLUMED 2: New feathers for an old bird. *Computer Physics Communications* **185,** 604–613 (2014).

36. Bonomi, M. *et al.* Promoting transparency and reproducibility in enhanced molecular simulations. *Nature Methods* **16,** 670–673 (2019).

37. Jo, S., Kim, T., Iyer, V. G. & Im, W. CHARMM-GUI: A web-based graphical user interface for CHARMM. *Journal of Computational Chemistry* **29,** 1859–1865 (2008).

38. Choi, Y. K. *et al.* CHARMM-GUI polymer builder for modeling and simulation of synthetic polymers. *Journal of Chemical Theory and Computation* **17,** 2431–2443 (2021).

39. Berendsen, H. J., Grigera, J. R. & Straatsma, T. P. The missing term in effective pair potentials. *Journal of Physical Chemistry* **91,** 6269–6271 (1987).

40. Martínez, L., Andrade, R., Birgin, E. G. & Martínez, J. M. PACKMOL: A package for building initial configurations for molecular dynamics simulations. *Journal of Computational Chemistry* **30,** 2157–2164 (2009).

41. Wang, J., Wolf, R. M., Caldwell, J. W., Kollman, P. A. & Case, D. A. Development and testing of a general amber force field. *Journal of Computational Chemistry* **25,** 1157–1174 (2004).

42. Wang, J., Wang, W., Kollman, P. A. & Case, D. A. Automatic atom type and bond type perception in molecular mechanical calculations. *Journal of Molecular Graphics and Modelling* **25,** 247–260 (2006).

43. Sprenger, K., Jaeger, V. W. & Pfaendtner, J. The general AMBER force field (GAFF) can accurately predict thermodynamic and transport properties of many ionic liquids. *The Journal of Physical Chemistry B* **119,** 5882–5895 (2015).

44. Mintis, D. G. & Mavrantzas, V. G. Effect of pH and Molecular Length on the Structure and Dynamics of Short Poly(acrylic acid) in Dilute Solution: Detailed Molecular Dynamics Study. *The Journal of Physical Chemistry B* **123,** 4204–4219. ISSN: 1520-6106, 1520-5207. `https://pubs.acs.org/doi/10.1021/acs.jpcb.9b01696` (2021) (May 2019).

45. Martinek, T. *et al.* Calcium ions in aqueous solutions: Accurate force field description aided by ab initio molecular dynamics and neutron scattering. *The Journal of Chemical Physics* **148** (2018).

46. Leontyev, I. V. & Stuchebrukhov, A. A. Electronic continuum model for molecular dynamics simulations. *The Journal of Chemical Physics* **130,** 085102. ISSN: 0021-9606, 1089-7690. `http://aip.scitation.org/doi/10.1063/1.3060164` (2022) (Feb. 2009).

47. Duboué-Dijon, E., Javanainen, M., Delcroix, P., Jungwirth, P. & Martinez-Seara, H. A practical guide to biologically relevant molecular simulations with charge scaling for electronic polarization. *The Journal of Chemical Physics* **153,** 050901. ISSN: 0021-9606, 1089-7690. `http://aip.scitation.org/doi/10.1063/5.0017775` (2022) (Aug. 2020).

48. Kohagen, M., Mason, P. E. & Jungwirth, P. Accurate Description of Calcium Solvation in Concentrated Aqueous Solutions. *The Journal of Physical Chemistry B* **118,** 7902–7909. ISSN: 1520-6106, 1520-5207. `https://pubs.acs.org/doi/10.1021/jp5005693` (2022) (July 2014).

49. Duboué-Dijon, E. *et al.* Binding of divalent cations to insulin: Capillary electrophoresis and molecular simulations. *The Journal of Physical Chemistry B* **122,** 5640–5648 (2018).

50. Darden, T., York, D. & Pedersen, L. Particle mesh Ewald: An N log (N) method for Ewald sums in large systems. *The Journal of Chemical Physics* **98,** 10089–10092 (1993).

51. Essmann, U. *et al.* A smooth particle mesh Ewald method. *The Journal of Chemical Physics* **103,** 8577–8593 (1995).

52. Hess, B., Bekker, H., Berendsen, H. J. & Fraaije, J. G. LINCS: A linear constraint solver for molecular simulations. *Journal of Computational Chemistry* **18,** 1463–1472 (1997).

53. Nosé, S. A unified formulation of the constant temperature molecular dynamics methods. *The Journal of Chemical Physics* **81,** 511–519 (1984).

54. Hoover, W. G. Canonical dynamics: Equilibrium phase-space distributions. *Physical Review A* **31,** 1695 (1985).

55. Parrinello, M. & Rahman, A. Polymorphic transitions in single crystals: A new molecular dynamics method. *Journal of Applied Physics* **52,** 7182–7190 (1981).

56. Laio, A. & Parrinello, M. Escaping free-energy minima. *Proceedings of the National Academy of Sciences of the United States of America* **99.** www.pnas.orgcgidoi10.1073pnas.202427399 (Oct. 2002).

57. Barducci, A., Bussi, G. & Parrinello, M. Well-tempered metadynamics: A smoothly converging and tunable free-energy method. *Physical Review Letters* **100.** arXiv: 0803.3861. ISSN: 00319007 (Jan. 2008).

58. Barducci, A., Bonomi, M. & Parrinello, M. Metadynamics. *WIREs Comput. Mol. Sci.* **1,** 826–843. ISSN: 1759-0876, 1759-0884. https://onlinelibrary.wiley.com/doi/10.1002/wcms.31 (2021) (Sept. 2011).

59. Tiwary, P. & Parrinello, M. A Time-Independent Free Energy Estimator for Metadynamics. *The Journal of Physical Chemistry B* **119,** 736–742. ISSN: 1520-6106, 1520-5207. https://pubs.acs.org/doi/10.1021/jp504920s (2022) (Jan. 2015).

60. Wang, L., Friesner, R. A. & Berne, B. J. Replica Exchange with Solute Scaling: A More Efficient Version of Replica Exchange with Solute Tempering (REST2). *The Journal of Physical Chemistry B* **115,** 9431–9438. ISSN: 1520-6106, 1520-5207. https://pubs.acs.org/doi/10.1021/jp204407d (2023) (Aug. 2011).

61. Bussi, G. Hamiltonian replica exchange in GROMACS: a flexible implementation. *Mol. Phys.* **112,** 379–384. ISSN: 0026-8976, 1362-3028. http://www.tandfonline.com/doi/abs/10.1080/00268976.2013.824126 (2022) (Feb. 2014).

62. Park, S., Zhu, X. & Yethiraj, A. Atomistic Simulations of Dilute Polyelectrolyte Solutions. *The Journal of Physical Chemistry B* **116,** 4319–4327. ISSN: 1520-6106, 1520-5207. https://pubs.acs.org/doi/10.1021/jp208138t (2022) (Apr. 2012).

63. Robbins, T. J. & Wang, Y. Effect of initial ion positions on the interactions of monovalent and divalent ions with a DNA duplex as revealed with atomistic molecular dynamics simulations. *Journal of Biomolecular Structure and Dynamics* **31,** 1311–1323. ISSN: 0739-1102, 1538-0254. http://www.tandfonline.com/doi/abs/10.1080/07391102.2012.732344 (2022) (2013).

64. Michaud-Agrawal, N., Denning, E. J., Woolf, T. B. & Beckstein, O. MDAnalysis: A toolkit for the analysis of molecular dynamics simulations. *Journal of Computational Chemistry* **32,** 2319–2327 (2011).

65. Gowers, R. J. *et al. MDAnalysis: A Python package for the rapid analysis of molecular dynamics simulations* in *Proceedings of the 15th python in science conference* **98** (2016), 105.

66. Humphrey, W., Dalke, A. & Schulten, K. VMD – Visual Molecular Dynamics. *Journal of Molecular Graphics and Modelling.* **14,** 33–38 (1996).

67. Stone, J. An Efficient Library for Parallel Ray Tracing and Animation MA thesis (Computer Science Department, University of Missouri-Rolla, 1998).

68. Neal, B., Asthagiri, D. & Lenhoff, A. Molecular Origins of Osmotic Second Virial Coefficients of Proteins. *Biophysical Journal* **75,** 2469–2477. ISSN: 00063495. https://linkinghub.elsevier.com/retrieve/pii/S000634959877691X (2023) (Nov. 1998).

69. Lund, M. & Jönsson, B. A Mesoscopic Model for Protein-Protein Interactions in Solution. *Biophysical Journal* **85,** 2940–2947. ISSN: 00063495. https://linkinghub.elsevier.com/retrieve/pii/S0006349503747146 (2023) (Nov. 2003).

70. Stark, A. C., Andrews, C. T. & Elcock, A. H. Toward Optimized Potential Functions for Protein–Protein Interactions in Aqueous Solutions: Osmotic Second Virial Coefficient Calculations Using the MARTINI Coarse-Grained Force Field. *Journal of Chemical Theory and Computation* **9,** 4176–4185. ISSN: 1549-9618, 1549-9626. https://pubs.acs.org/doi/10.1021/ct400008p (2023) (Sept. 2013).

71. Neal, B., Asthagiri, D. & Lenhoff, A. Molecular origins of osmotic second virial coefficients of proteins. *Biophysical Journal* **75,** 2469–2477 (1998).

72. Hill, T. L. *Statistical mechanics: principles and selected applications* 341–350 (Courier Corporation, 2013).

73. Lemke, T. & Peter, C. EncoderMap: Dimensionality Reduction and Generation of Molecule Conformations. *Journal of Chemical Theory and Computation* **15,** 1209–1215. ISSN: 1549-9618, 1549-9626. https://pubs.acs.org/doi/10.1021/acs.jctc.8b00975 (2023) (Feb. 2019).

74. Lemke, T., Berg, A., Jain, A. & Peter, C. EncoderMap(II): Visualizing Important Molecular Motions with Improved Generation of Protein Conformations. *Journal of Chemical Information and Modeling* **59,** 4550–4560. ISSN: 1549-9596, 1549-960X. https://pubs.acs.org/doi/10.1021/acs.jcim.9b00675 (2023) (Nov. 2019).

75. Bandyopadhyay, S. & Mondal, J. A deep autoencoder framework for discovery of metastable ensembles in biomacromolecules. *The Journal of Chemical Physics* **155.** arXiv: 2106.00724 Publisher: American Institute of Physics Inc. ISSN: 10897690 (Sept. 2021).

76. Glielmo, A. *et al.* Unsupervised Learning Methods for Molecular Simulation Data. *Chemical Reviews* **121,** 9722–9758. ISSN: 0009-2665, 1520-6890. https://pubs.acs.org/doi/10.1021/acs.chemrev.0c01195 (2023) (Aug. 2021).

77. Paszke, A. *et al. Automatic differentiation in pytorch* in *31st Conference on Neural Information Processing Systems* (2017).

78. Paszke, A. *et al.* Pytorch: An imperative style, high-performance deep learning library. *Advances in Neural Information Processing Systems* **32** (2019).

79. Sabbagh, I. & Delsanti, M. Solubility of highly charged anionic polyelectrolytes in presence of multivalent cations: Specific interaction effect. *European Physical Journal E* **1,** 75–86 (2000).

Chapter 4

ELECTROSTATICALLY DRIVEN POLYELECTROLYTE BINDING TO NEUTRAL CALCITE SURFACES

Aqueous polyelectrolytes are effective mineralization inhibitors due to their ability to template onto crystal surfaces and chelate ions in solution. These additives have been shown to alter the morphology and polymorph of calcium carbonate crystals, making them promising candidates for biological and industrial applications. However, the molecular mechanisms governing the interactions between polyelectrolytes and crystal surfaces remain poorly understood and are key to designing more effective mineralization inhibitors. In this study, we investigate the adsorption of poly(acrylic acid) (PAA) on the dominant calcite $(10\bar{1}4)$ cleavage plane using all-atom molecular dynamics simulations. Although the calcite slab is electrostatically neutral, its charge distribution induces a strong electrostatic potential, which leads to significant water structuring at the interface and interacts with the charged functional groups of PAA. The adsorption of PAA is driven by the formation of multiple binding modes, including direct monomer binding to the surface, ion-bridges, and water-mediated interactions. As the polymer adsorbs to the surface, the chain conformation adapts to the interfacial water structure, facilitating the integration of the PAA chain into pre-existing hydrogen bond networks rather than disrupting the broader interfacial water structure. Our findings reveal that the adsorption of the polyelectrolyte is sensitive to chain length, charge density, and aqueous solution conditions, with longer chains and higher charge densities resulting in stronger adsorption. These results provide new insights into the molecular mechanisms governing the adsorption of polyelectrolytes on crystalline surfaces and suggest that polyelectrolyte binding affinity can be tuned by altering the polymer chain interactions with the interfacial water structure rather than the surface itself.

This chapter includes content from our previously published article:

1. Glisman, A. *et al.* Binding modes and water-mediation of polyelectrolyte adsorption to a neutral surface. *Manuscript in Preparation* (2024).

4.1 Introduction

The process of mineralization, or the formation of solid mineral deposits, is ubiquitous in nature and industry. In biological systems, mineralization is essential for the formation and growth of bones, teeth, and shells [1–3]. For example, sea shells are composed of calcium carbonate ($CaCO_3$) crystals, which form through the precipitation of Ca^{2+} and $CO_3{}^{2-}$ ions from seawater and exhibit highly ordered structures [4]. Interestingly, the common polymorph of $CaCO_3$ in sea shells is aragonite, which is metastable relative to the thermodynamically stable calcite polymorph. It is believed that the formation of aragonite is influenced by the presence of small ions [5, 6] and macromolecules such as proteins and polyelectrolytes [7–9].

However, mineralization can also be detrimental, forming scale deposits in industrial processes, such as water treatment facilities and desalination plants [10, 11]. In addition to polymorph and morphology control, industrial processes require the inhibition of mineralization to prevent scale formation or to limit the growth of preexisting mineral deposits. For both of these applications, aqueous solutions of polyelectrolytes have shown promise as an effective means of controlling mineralization.

Polyelectrolytes (PEs) are particularly effective at inhibiting $CaCO_3$ growth due to their ability to chelate Ca^{2+} ions and modify or slow crystal growth through their charged functional groups [12–17]. PEs have also been shown to stabilize amorphous calcium carbonate (ACC) [18, 19], stabilize the vaterite polymorph [20], and alter the surface morphology of $CaCO_3$ precipitates [21, 22]. While the effects of PEs on $CaCO_3$ growth have been well-documented, the molecular mechanisms underlying the growth modification and inhibition of $CaCO_3$ by PEs are poorly understood. It is believed that PEs can template the growth of $CaCO_3$ crystals by preferential binding patterns and by altering the local environment around the growing crystal [13], but the specific interactions between PEs and $CaCO_3$ surfaces are not well characterized.

Many research efforts have employed molecular modeling to describe the crystalline phase of $CaCO_3$ as well as its interfaces with water and organic molecules [23–31]. Aschauer *et al.* [29] used molecular dynamics (MD) simulations to investigate the growth modification of calcite with a step defect by PAA with a chain length of 10 monomers. They found that the adsorption of PAA on the calcite surface was energetically unfavorable, but it was stabilized by an

increase in the system entropy due to the destruction of the interfacial water structure. PAA was seen to weakly bind to the step defect and decreased the translational and orientational order of water molecules at the interface. Sparks *et al.* [30] built on this work by investigating the adsorption of longer PAA chains (28 monomers) on the calcite $(10\bar{1}4)$ surface. It was found that the longer PAA chains preferentially adsorbed with an extended conformation and that only a small fraction of the PAA chain was adsorbed on the surface. In both studies, the authors noted that multiple binding effects were not observed in a single trajectory of 1–2 ns. The limited ensemble sampling suggests longer simulation times are needed to observe the full range of binding modes.

Our previous work investigated how polyelectrolytes, such as poly(acrylic acid) (PAA), can chelate Ca^{2+} ions to prevent nucleation of $CaCO_3$ crystal, as well as avoid the precipitation of PAA–Ca^{2+} complexes [32, 33]. In this study, we extend our previous models to investigate the adsorption of PAA on a $CaCO_3$ surface. We aim to understand the molecular principles that govern the adsorption of PAA on a $CaCO_3$ surface to understand what design principles may lead to more effective antiscalant polyelectrolytes. We focus on the adsorption of the model polyelectrolyte PAA on the calcite $(10\bar{1}4)$ surface, the dominant surface of calcite in aqueous solution [34]. We seek to probe the effects of chain length, PE charge density, and aqueous solution conditions on the adsorption behavior of PAA on the calcite surface, with a particular focus on the role of water in mediating the adsorption process.

The rest of the manuscript is organized as follows. In the Methods section, we describe the models and parameters used in our enhanced sampling molecular dynamics simulations. We then present the results of our study and discuss the implications of our findings in the Results and Discussion section. Finally, we summarize our findings and suggest future research directions in the Conclusions section.

4.2 Methods

We studied the adsorption properties of poly(acrylic acid) (PAA) on the calcite $(10\bar{1}4)$ surface using molecular dynamics simulations. Five systems were simulated, as shown in Table 4.1. The $(10\bar{1}4)$ surface was chosen as it is the most stable surface of calcite in water [34]. The systems included monomer chain lengths of 16 and 32 in both fully charged (PAA) and neutral (PAAn)

Polymer	Aqueous Ions	Box Length
16-PAA	16 Na^+	9 nm
16-PAAn	–	9 nm
32-PAA	32 Na^+	12 nm
32-PAAn	–	12 nm
32-PAA	32 Na^+, 32 $CaCl_2$	12 nm

Table 4.1: Polyelectrolyte and ion systems simulated for single-chain adsorption on the calcite $(10\bar{1}4)$ surface. The polymer entries indicate the number of monomers in the polymer chain and whether they are charged (AA) or neutral (AAn) acrylic acid monomers. The ions indicate the number of ions in the system, and the box length indicates the linear dimension of the simulation box in the x and y directions. The z direction is perpendicular to the calcite surface and is 1 nm longer than the box length to accommodate the approximately 1 nm thick calcite slab.

forms of acrylic acid. The different ionization states of the polymer provide insight into the effects of polyelectrolyte charge density on adsorption behavior. As PAA is a weak polyelectrolyte with a pKa of ~ 4.5 [35], these systems also provide indirect information on the role of pH (i.e., charge regulation) on adsorption behavior. For systems with charged monomers, Na^+ ions were added to neutralize the system. The 32-mer PAA system was also simulated with 32 $CaCl_2$ ions to investigate the effect of aqueous multi-valent ions on adsorption behavior.

Initial polymer structures were generated using CHARMM-GUI [36, 37] with atactic stereochemistry. Calcite crystal structures were taken from the American Mineralogist Crystal Structure Database [38] with data from Markgraf & Reeder [39]. The unit cell of the calcite slab was then sliced along the $(10\bar{1}4)$ plane to create a 1 nm thick slab in the z axis and replicated in the x and y axes to generate a super-cell of the desired size using the Python Materials Genomics (PyMatGen) package [40]. Finally, the system was solvated with water molecules and neutralized with Na^+ ions using GROMACS tools [41–43] in a cubic box with periodic boundary conditions. Snapshots of the systems after equilibration are shown in Figure 4.1.

Following the protocols and models established in our previous work [32, 33], we employed the SPC/E [44] water model and the general AMBER force field (GAFF) [45–47] to model the polymer chains as well as the calcite slab. To appropriately balance the strength of electrostatic interaction, we used

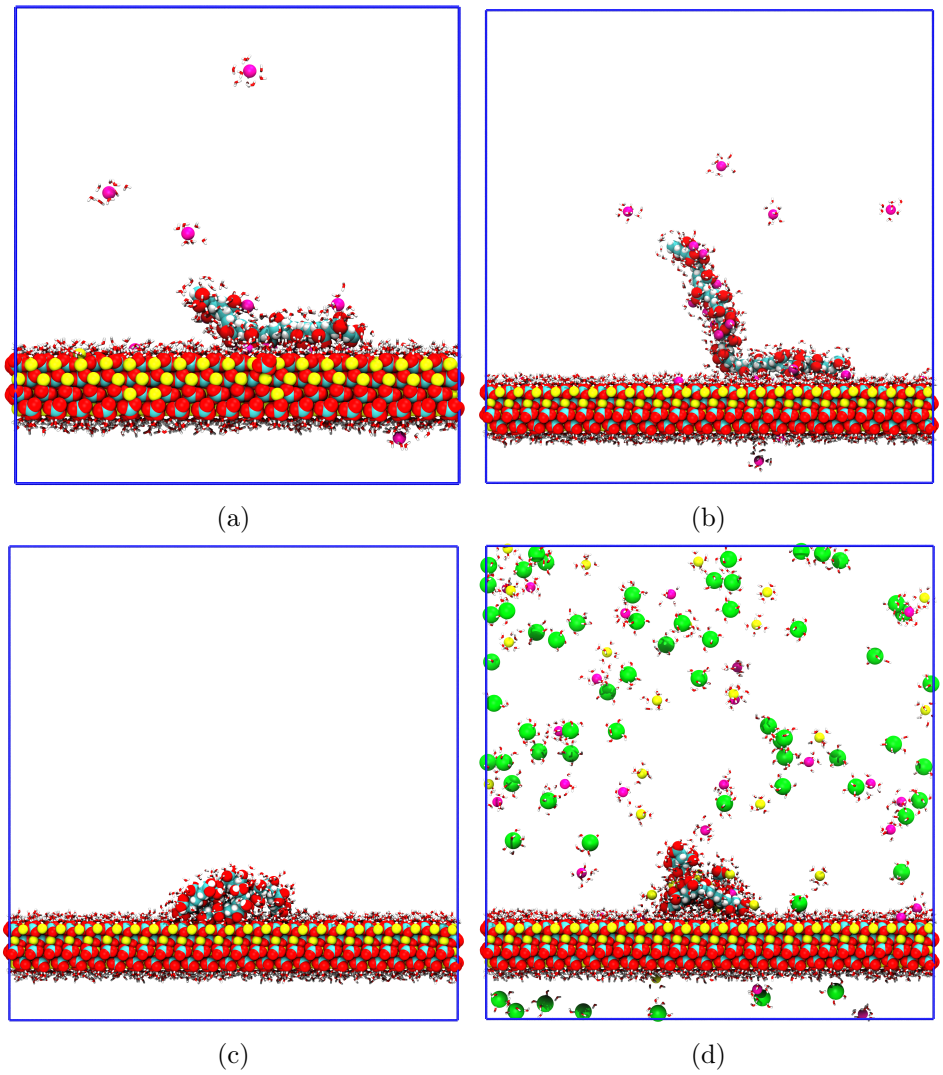

Figure 4.1: Snapshots of the polyelectrolytes binding to the calcite surface: (a) 16-PAA, (b) 32-PAA, (c) 32-PAAn, and (d) 32-PAA with 32 $CaCl_2$. The first solvation shell water molecules are shown in the licorice representation, and other atoms are shown in the van der Waals representation. Oxygen atoms are red, carbon atoms are gray, calcium atoms are green, sodium atoms are purple, chlorine atoms are yellow, and hydrogen atoms are white.

the electronic continuum correction (ECC) method [48, 49] to correct the partial charges of all non-water atoms in the system. Further details on the methodology can be found in Glisman *et al.* [32]

We used the GROMACS (version 2023.2) simulation package [41–43] patched with the PLUMED (version 2.9.0) plugin [50–52]. A cutoff distance of 1.2 nm was used for the van der Waals interactions, and the Particle Mesh Ewald (PME) method [53, 54] was used to calculate the long-range electrostatic inter-

actions with a real-space cutoff of 1.2 nm. The LINCS algorithm [55] was used to constrain bond lengths for hydrogen atoms, and the leap-frog algorithm was used to integrate Newton's equations of motion. Where applicable, the system temperature was maintained at 300 K using the Nosé–Hoover thermostat [56, 57] with a 0.25 ps relaxation time constant. The pressure was maintained at 1 bar using the semi-isotropic Parrinello–Rahman barostat [58] with a 5.0 ps relaxation time constant. The compressibility was set to 4.5×10^{-5} bar^{-1} in the z direction and 4.5×10^{-15} bar^{-1} in the x and y directions to effectively make the crystalline slab incompressible.

The systems were minimized using the steepest descent algorithm for approximately 100,000 steps. The systems were then equilibrated for 5 ns in the NVT ensemble, followed by 5 ns in the NPT ensemble with a time step of 1 fs to equilibrate the system temperature and density. Finally, production NVT simulations were run for 500 ns with a time step of 2 fs. Harmonic restraints were applied to the calcite slab to prevent the slab from moving during the simulations. The first 50 ns were discarded for each simulation as equilibration, and the remaining 450 ns were used for analysis. Each simulation consisted of five independent runs with different starting polymer conformations, and the results were averaged to obtain the final values. The error bars reported are 95% confidence intervals from the independent simulations.

To enhance the sampling of the polymer conformations, we used the on-the-fly probability-enhanced (OPES) method developed by Invernizzi & Parrinello [59] and later extended to replica exchange (OneOPES) techniques by Rizzi *et al.* [60]. The OneOPES method uses eight replicas with varying bias potentials to enhance the sampling of the polymer adsorption conformations and improve the convergence of the free energy calculations. The base (first) replica contains a single OPES bias potential, and the remaining replicas contain multiple OPES bias potentials with increasing strength, such that the highest (eighth) replica rapidly explores the entire free energy landscape. Exchange attempts are made between neighboring replicas every 1,000 steps, and the enhanced sampling parameters were tuned to achieve a minimum average exchange acceptance rate of 20%.

In the first replica, the z distance between the center of mass of the polymer and the calcite surface was used as the collective variable (CV) for the OPES Explore bias potential [61]. The distance CV was updated with a 10,000 step

pace, 0.2 nm width, and 30 kJ/mol barrier. The second replica added a second OPES Explore bias potential on the polymer radius of gyration with a 20,000 step pace, 0.02 nm width, and a barrier of 8 kJ/mol. The third replica added a third OPES Explore bias potential on the coordination number of aqueous ions around the carboxylate oxygens with a 20,000 step pace, 0.2 width, and 8 kJ/mol barrier. The coordination number was calculated with the continuous PLUMED coordination plugin with $n = 8$, $m = 16$, and $r_0 = 0.35$ nm. Finally, the fourth replica added a fourth OPES Explore bias potential on average z distance between the aqueous ions and the calcite surface with a 20,000 step pace, 0.2 nm width, and 8 kJ/mol barrier.

In addition to the OPES Explore bias potentials, the OneOPES method also uses the OPES MultiThermal bias potential [62] to allow the system to simultaneously explore multiple temperature distributions without altering the thermostat. The MultiThermal bias was updated with a 100 step pace and a maximum temperature of 304 K, 312 K, 326 K, 338 K, 354 K, and 374 K for replicas 3–8, respectively. Each replica contained independent OPES Explore and MultiThermal bias potentials, as prescribed by the OneOPES method.

4.3 Results and Discussion

The binding potential of mean force (PMF) for the polyelectrolyte chains is shown in Figure 4.2. The PMF is calculated as a function of the z distance from the chain center of mass to the top layer of the calcite surface (z_{surf}). Error bars are derived from the 95% confidence interval of five independent simulations. The reference state for each system is the free energy at $z_{\text{surf}} = 4$ nm, where the polyelectrolyte-calcite interaction has plateaued.

In all studied systems, the polyelectrolyte chains show a strong attraction to the calcite surface, as evidenced by the negative PMF values at short PE-surface distances ($z_{\text{surf}} < 1$ nm). The charged polyelectrolyte systems (16-PAA/32-PAA) exhibit significantly stronger attraction to the calcite surface compared to the neutral systems (16-PAAn/32-PAAn), indicating that electrostatic interactions between the polyelectrolyte and the calcite surface are the dominant driving force for adsorption. However, the PE-surface interaction appears to be mediated by other species, as the PMF minimum occurs on average at distances of ~ 0.65 nm.

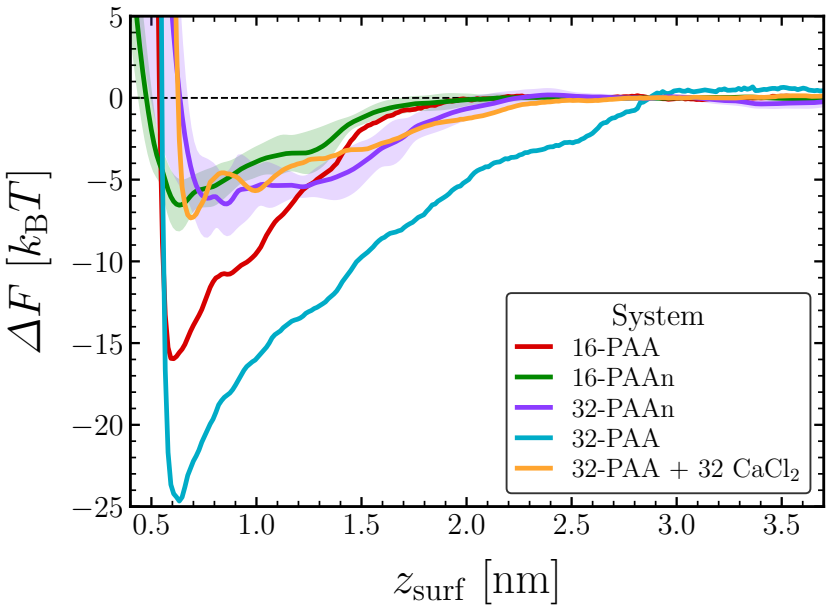

Figure 4.2: The potential of mean force for the z distance of the polymer chain center of mass from the calcite surface.

The effects of chain length are also evident for the charged systems, with the PMF minimum shifting from 16 $k_\mathrm{B}T$ to 25 $k_\mathrm{B}T$ as the chain length increases from 16 to 32 monomers. The sub-linear increase in binding affinity with chain length suggests that many polyelectrolyte monomers do not interact strongly with the calcite surface. As discussed in our previous work [32, 33], when aqueous Ca^{2+} ions are present, the polyelectrolyte chains strongly chelate the Ca^{2+} ions, thereby lowering the polyelectrolyte–ion complex charge density and reducing the electrostatic interactions with the calcite surface. The neutral systems also exhibit a weaker attraction to the calcite surface, consistent with their weaker electrostatic interactions. Additionally, the broader PMF minimum indicates that the adsorption binding modes are less specific and more driven by solvent-mediated interactions.

To investigate how adsorption alters the polyelectrolyte chain structure, we calculated the radius of gyration (R_g) of the polyelectrolyte chain as a function of the distance from the calcite surface (Figure 4.3). At short PE-surface distances, the polyelectrolyte chains exhibit an increase in R_g, as the chains extend towards the calcite surface to maximize the number of favorable interactions. Due to the chelation of aqueous Ca^{2+} ions, the 32 $CaCl_2$ system exhibits a much smaller R_g than the salt-free system, which is consistent with Ca^{2+} ions facilitating intra-chain ion-bridges that reduce the chain's conformational

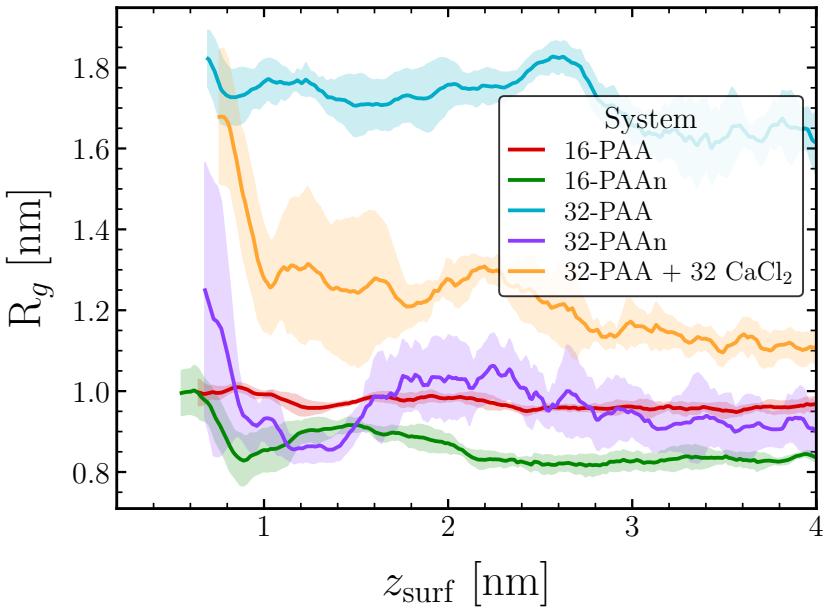

Figure 4.3: Polymer radius of gyration profile of the polymer chain near the calcite surface.

freedom [32]. Ca^{2+} chelation in the 32 $CaCl_2$ system causes the polyelectrolyte expansion upon adsorption to be less favorable, which is consistent with the weaker adsorption observed. The neutral systems are more poorly solvated and exhibit a smaller R_g than the charged systems. While this size reduction minimizes PE-solvent interactions, it similarly minimizes the number of favorable PE-surface interactions, which may explain the weaker adsorption of the neutral systems.

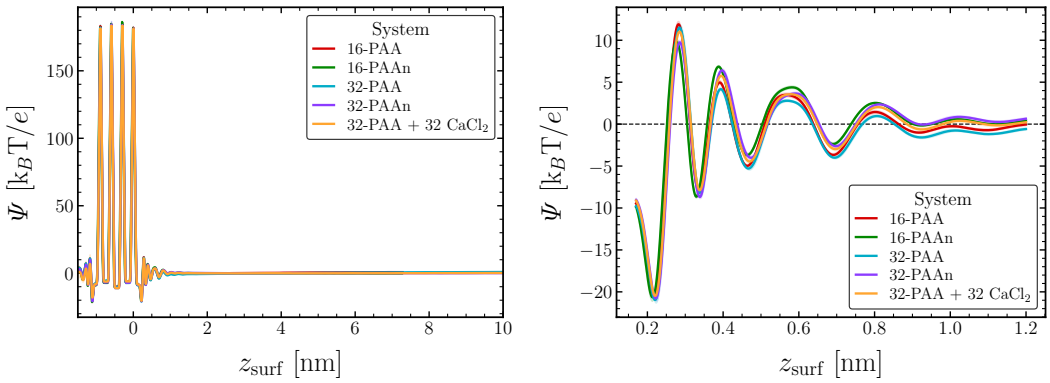

Figure 4.4: Average electrostatic potential profile of the system (a) and zoomed in near the calcite surface (b).

We calculated the system electrostatic potential by solving Poisson's equation ($\nabla^2\Psi = -\rho_c/\epsilon_0$) to understand the long-ranged and mediated electrostatic interactions between the polyelectrolyte chains and the calcite surface. The potential profile was approximated as one-dimensional and solved using the average system charge density (ρ_c) along the z-axis with periodic boundary conditions using a finite difference method. The electrostatically neutral calcite slab creates a highly negative potential near the surface due to the morphology of the calcite ($10\bar{1}4$) surface (Figure 4.4b). As seen in Figure 4.1, the calcite layers consist of interleaved Ca^{2+} and $CO_3{}^{2-}$ ions. The carbonate ions are oriented such that the oxygen atoms are pointing slightly outwards the surface, creating a charge distribution resulting in the potential profile shown in Figure 4.4a and inducing a strong dipole moment in the solvent near the calcite surface (Figure 4.5a). The potential profile deviates significantly from the bulk potential (arbitrary reference) within 1 nm of the calcite surface, consistent with the strong adsorption of the polyelectrolyte chains to the calcite surface. Notably, the potential profile is not significantly perturbed by the presence of polyelectrolyte chains or small ions. As the simulation box size was chosen to ensure the polymers were in the dilute regime, it is not surprising that the polyelectrolyte chains and small ions do not significantly alter the potential profile of the system.

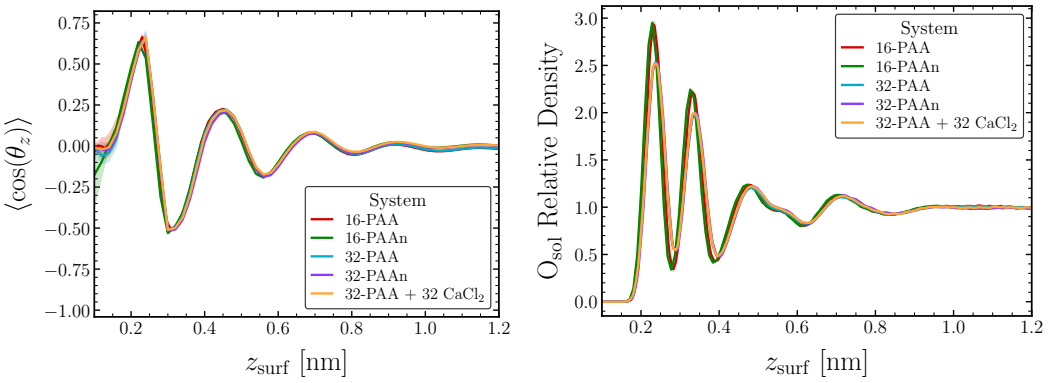

(a) (b)

Figure 4.5: Interfacial water structure near the calcite surface. (a) The average angle of the dipole moment of the solvent. The dipole moment angle is measured with respect to the $+z$ axis such that $\cos(\theta) = 1$ indicates the water oxygen is pointing directly towards the calcite surface and $\cos(\theta) = -1$ indicates the water hydrogens are pointing directly towards the calcite surface. (b) Linear solvent density (water oxygen) relative density profile near the calcite surface. The density is normalized by the bulk water density.

The potential profile near the calcite surface induces the strong dipole moment of the solvent. In Figure 4.5a, we show the average dipole moment angle of the solvent with respect to the $+z$ axis. The electrostatic potential profile near the calcite surface is highly negative, which attracts the water hydrogen atoms toward the surface and the water oxygen atoms away from the surface. The second layer of water molecules is oriented such that the water oxygen atoms point towards the surface to facilitate hydrogen bonding with the first layer of water molecules. In addition to rotational ordering, the solvent is linearly ordered near the calcite surface (Figure 4.5b) into two highly ordered and two weakly ordered layers. Note that the highly ordered layers are within 0.5 nm of the calcite surface, which is closer than the most favorable PE-surface distance of 0.65 nm. This indicates that the PE dominantly adsorbs within the weakly ordered solvent layers and does not significantly perturb the highly ordered solvent layers directly adjacent to the calcite surface.

Figure 4.5 provides evidence that the PE does not significantly perturb the linear and angular solvent structure near the calcite surface. Instead, the PE modifies its structure to interact favorably with the interfacial solvent structure to maximize the number of favorable PE-solvent interactions rather than disrupting the solvent structure to maximize PE-surface interactions. The PE displaces water molecules from the surface due to excluded volume effects, but this is a local rather than long-ranged effect. We even see that in the PE first solvation shell (see Figure S2 in the Supporting Information), the water molecules are still ordered according to the interfacial water structure, indicating that the PE does not significantly perturb the solvent structure. The polymer binding, therefore, can free water molecules from the excluded volume of the PE and increase the entropy of the system, but it does not appear to significantly increase the entropy of the remaining interfacial water structure.

Due to the negative surface potential, small cations such as Na^+ and Ca^{2+} accumulate near the calcite surface (see Figure S1 in the Supporting Information), which may facilitate the adsorption of the polyelectrolyte chains through ion-bridges. In Figure 4.6, we show the distribution of binding modes of the polyelectrolyte to the calcite surface for the systems studied. It is clear that direct monomer adsorption onto the calcite surface is not the dominant bind-

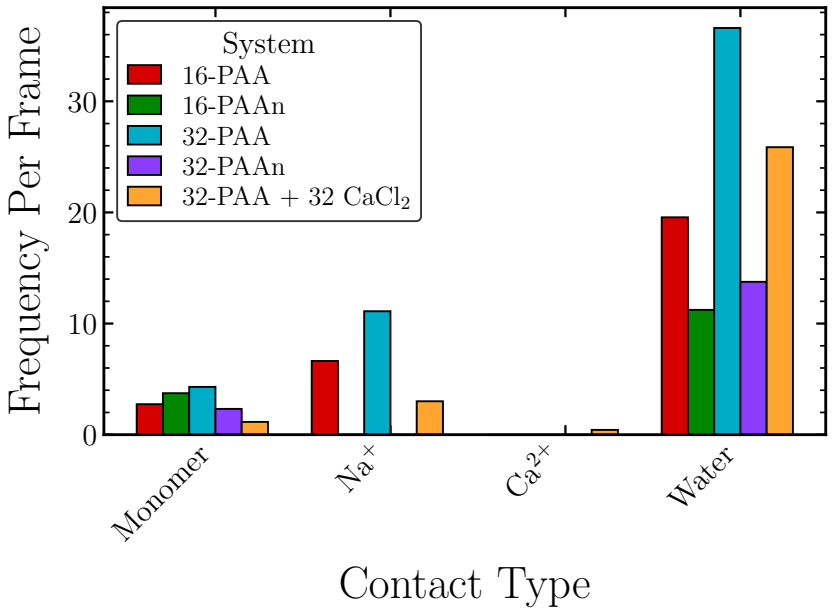

Figure 4.6: Distribution of binding modes of the polyelectrolyte to the calcite surface: direct monomer adsorption, Na^+ bridges, Ca^{2+} bridges, and water bridges. The y-axis is the number of contacts formed between the polyelectrolyte and the calcite surface on average.

ing mode for the polyelectrolyte chains. On average, only 2–5 monomers are directly adsorbed to the calcite surface, with no clear trend related to chain length or charge density.

Instead, the dominant binding modes are Na^+ bridges (when Na^+ ions are present) and water bridges. A Na^+ bridge is defined as a Na^+ ion that is simultaneously coordinated to the polyelectrolyte and the calcite surface. The coordination exists when the Na^+ ion is within 3.5 Å of the polyelectrolyte and the calcite surface. Ca^{2+} bridges are defined similarly. Water bridges are defined as water molecules that simultaneously form hydrogen bonds between the polyelectrolyte and the calcite surface. These are the dominant binding modes for the polyelectrolyte chains, with the number of water bridges increasing with chain length and charge density. Higher-order water bridges are also observed (see Figure S3 the in Supporting Information), where multiple water molecules form a bridge between the polyelectrolyte and the calcite surface.

The 32 $CaCl_2$ system presents a unique case where the ion-bridges are significantly reduced. The chelated ions are not available to form ion-bridges, which reduces the number of water bridges as well as Na^+ and Ca^{2+} bridges compared to the salt-free system, resulting in a weaker adsorption of the polyelectrolyte chain to the calcite surface (Figure 4.2).

4.4 Conclusions

This study elucidated the mechanisms driving the adsorption of polyelectrolytes on crystalline surfaces. Specifically, we demonstrated that the adsorption of poly(acrylic acid) (PAA) on the calcite $(10\bar{1}4)$ surface is driven by the conformational changes of the PAA chains to integrate into the hydrogen bond network of the interfacial water layer. Although polyelectrolyte adsorption displaced some water molecules due to the excluded volume of the PAA chains, the overall interfacial water structure remained largely undisturbed.

Furthermore, the electrostatically neutral calcite slab generated a strong electrostatic field that both ordered the interfacial water layer and attracted small ions to the surface. The resulting ion-bridging and water-mediated interactions between the PAA chains dominated the polyelectrolyte-surface interactions.

In an experimental setting, the difference in adsorption affinity between ionized and neutral PAA chains may not be as pronounced as reported in our study. A growing crystalline face will facilitate a dynamic exchange of Ca^{2+} ions at the interface, which can be chelated by the PAA chains. The chelation of Ca^{2+} ions by ionized PAA chains could reduce the chain adsorption affinity, weakening the electrostatic interactions between the PAA chains and the surface.

The unique surface morphology of the calcite $(10\bar{1}4)$ surface, where $CO_3{}^{2-}$ groups dominate the surface interactions, may also contribute to the observed adsorption behavior. The surface Ca^{2+} ions are partially hidden by the rotated $CO_3{}^{2-}$ groups, which may favor the indirect bridging of the PAA chains through the interfacial water layer over direct binding to the surface Ca^{2+} ions. Future research should investigate the adsorption of PAA on multiple surfaces of the various polymorphs of $CaCO_3$ to understand the full scope of PAA adsorption on $CaCO_3$ surfaces, as multiple surfaces are present in a crystalline $CaCO_3$ particle growing in solution [34]. The Ca^{2+}-terminated calcite basal

plane, for example, may facilitate direct binding of PAA chains to the surface Ca^{2+} ions, which may lead to important differences in the binding affinity and selectivity of PAA chains to different $CaCO_3$ surfaces.

4.5 Appendix

In this section, we present additional details on the structure of the adsorption of poly(acrylic acid) (PAA) on a calcite $(10\bar{1}4)$ surface. We show the linear density profiles of aqueous ions and the dipole moment of the polyelectrolyte solvation shell. We also present the distribution of the polyelectrolyte binding modes to the calcite surface, including higher-order water bridges between the polyelectrolyte and the surface.

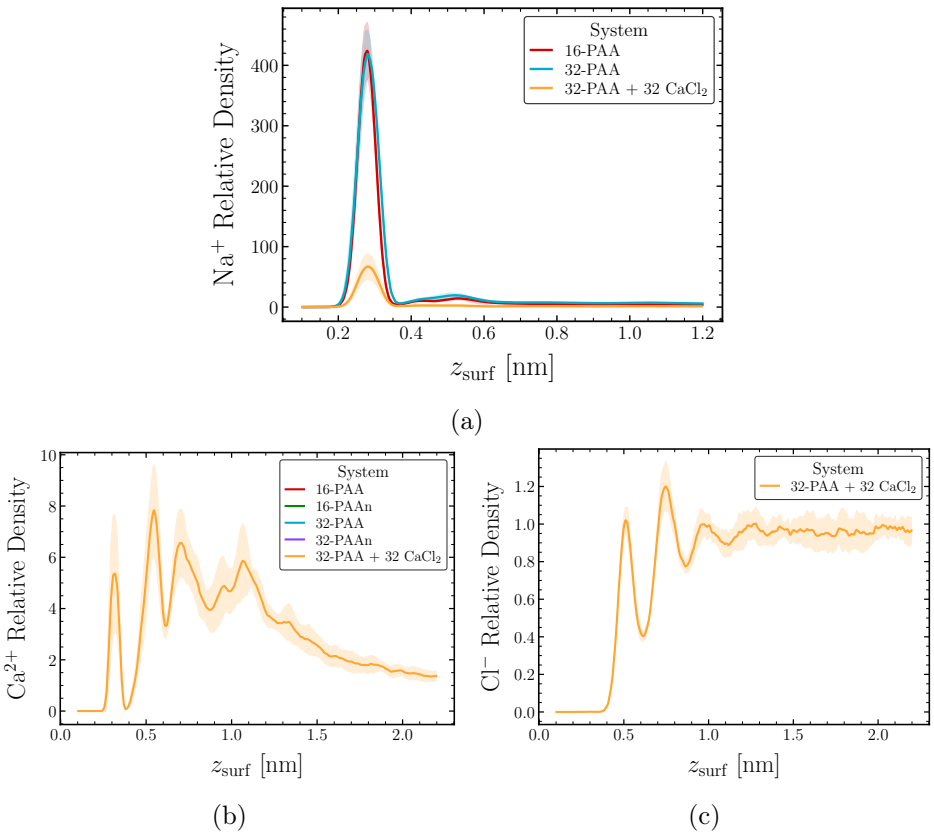

Figure 4.7: Relative density profiles of (a) Na^+, (b) Ca^{2+}, and (c) Cl^- ions near the calcite surface. Note that the relative number densities are normalized by the bulk number density of each ion to highlight the depletion and accumulation of ions near the surface.

From Figure 4.7a, we observe that Na^+ ions accumulate near the calcite surface, with a peak in the density profile at approximately 0.3 nm from the surface, indicating direct (non-water mediated) adsorption. However, when

aqueous Ca^{2+} ions are present in the system, the density peak of Na^{+} ions is reduced, as the Ca^{2+} ions compete with Na^{+} ions for adsorption sites. Ca^{2+} ions also accumulate near the surface (Figure 4.7b), with a peak in the density profile at approximately 0.3 nm from the surface, yet most Ca^{2+} ions are found 0.5–2.0 nm from the surface. The broad distribution of Ca^{2+} ions near the surface is due to the chelation of Ca^{2+} ions by the carboxylate groups of the polyelectrolyte, which itself prefers to be further from the surface with water-mediated adsorption. Cl^{-} ions (Figure 4.7c) are found in the bulk solution and are depleted near the surface.

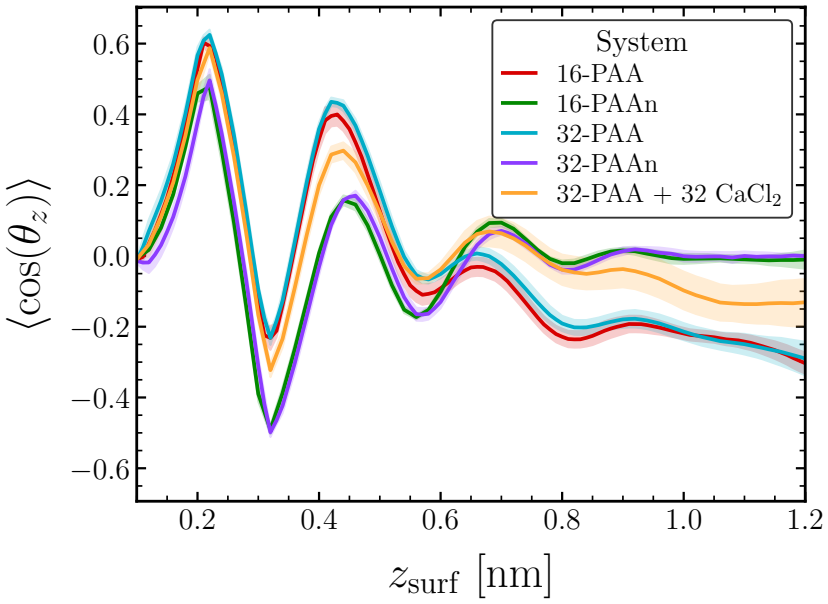

Figure 4.8: Average dipole moment angle profile of the polyelectrolyte solvation shell near the calcite surface. The dipole moment angle is measured with respect to the z axis. The solvation shell is defined as all water molecules within 3.5 Å of the polyelectrolyte.

In Figure 4.8, we show the average dipole moment angle of the polyelectrolyte solvation shell near the calcite surface. The solvation shell is defined as all water molecules within 3.5 Å of the polyelectrolyte atoms, and we calculate the average dipole moment angle of the water molecules with respect to the z axis. While the magnitude of the orientational correlations is slightly reduced compared to the overall interfacial water structure (Figure 4.5a), the solvation shell still strongly prefers to order according to the overall interfacial water structure. As the polyelectrolytes bind to the surface, the water molecules in the solvation shell retain the interfacial water profile discussed in the main text, as the qualitative behavior of the water molecules is not significantly

altered by the presence of the polyelectrolyte. When the polyelectrolyte is further from the surface, the water molecules in the solvation shell are less ordered, but the overall trend of the water molecules deviate from the bulk water structure to more favorably interact with the polyelectrolyte. This can be seen by the negative dipole moment angle for $z_{\text{surf}>\approx 0.8}$ nm, whereas the bulk water structure has a decayed to zero at the same distance from the surface.

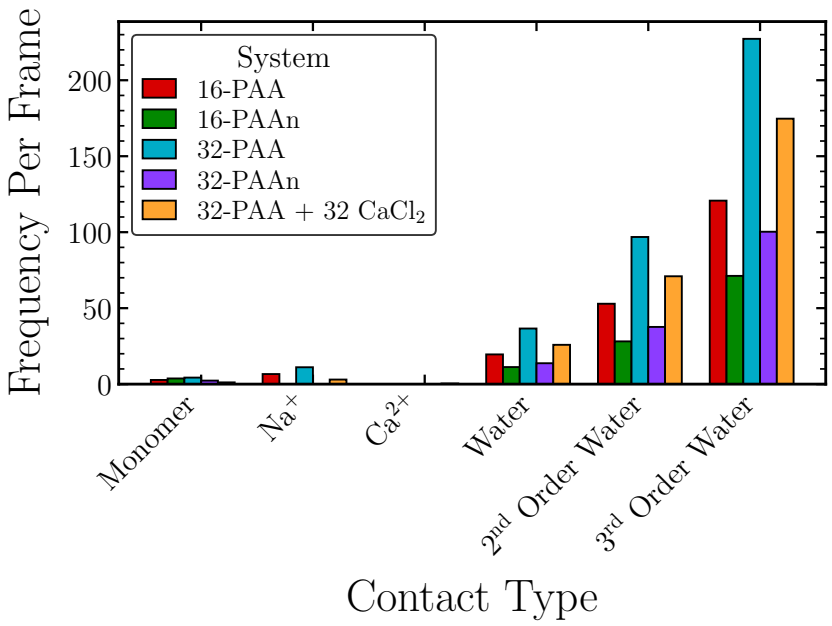

Figure 4.9: Distribution of binding modes of the polyelectrolyte to the calcite surface: direct monomer adsorption, Na^+ bridges, Ca^{2+} bridges, and water bridges. A water bridge is defined as a water molecule that forms a hydrogen bond between the polyelectrolyte and the calcite surface simultaneously, and higher-order water bridges involve more than one water molecule in the bridge. The y axis is the number of contacts formed between the polyelectrolyte and the calcite surface on average.

Figure 4.9 contains the distribution of binding modes found in the main text (Figure 4.6) with the addition of second and third-order water bridges. A second-order water bridge is defined as a two-water network that simultaneously forms a hydrogen bond between the polyelectrolyte and the calcite surface while also forming a hydrogen bond between the two water molecules. A third-order water bridge is defined similarly but with three water molecules. Higher-order water bridging occurs much more frequently than direct interactions or salt bridges and follows the same trend as first-order water bridges, with the majority of the binding modes being water-mediated.

References

1. Weiner, S. & Addadi, L. Design strategies in mineralized biological materials. *Journal of Materials Chemistry* **7,** 689–702 (1997).

2. Simkiss, K. & Wilbur, K. M. *Biomineralization* (Elsevier, 2012).

3. Dhami, N. K., Reddy, M. S. & Mukherjee, A. Biomineralization of calcium carbonates and their engineered applications: A review. *Frontiers in Microbiology* **4,** 314 (2013).

4. Kocot, K. M., Aguilera, F., McDougall, C., Jackson, D. J. & Degnan, B. M. Sea shell diversity and rapidly evolving secretomes: Insights into the evolution of biomineralization. *Frontiers in Zoology* **13,** 1–10 (2016).

5. De Leeuw, N. H. Molecular dynamics simulations of the growth inhibiting effect of Fe^{2+}, Mg^{2+}, Cd^{2+}, and Sr^{2+} on calcite crystal growth. *Journal of Physical Chemistry B* **106,** 5241–5249. ISSN: 10895647 (May 2002).

6. Jung, G. Y. *et al.* Thermodynamic Control of Amorphous Precursor Phases for Calcium Carbonate via Additive Ions. *Chemistry of Materials* **31.** Publisher: American Chemical Society, 7547–7557. ISSN: 15205002 (Sept. 2019).

7. Sun, W., Jayaraman, S., Chen, W., Persson, K. A. & Ceder, G. Nucleation of metastable aragonite CaCO3 in seawater. *Proceedings of the National Academy of Sciences* **112,** 3199–3204 (2015).

8. Feng, Q. *et al.* Polymorph and morphology of calcium carbonate crystals induced by proteins extracted from mollusk shell. *Journal of Crystal Growth* **216,** 459–465 (2000).

9. Sikirić, M. D. & Füredi-Milhofer, H. The influence of surface active molecules on the crystallization of biominerals in solution. *Advances in Colloid and Interface Science* **128-130,** 135–158. ISSN: 00018686 (Dec. 2006).

10. Qasem, N. A., Mohammed, R. H. & Lawal, D. U. Removal of heavy metal ions from wastewater: A comprehensive and critical review. *Npj Clean Water* **4,** 1–15 (2021).

11. Amjad, Z., Zuhl, R. W. & Zibrida, J. F. *Factors Influencing the Precipitation of Calcium-Inhibitor Salts in Industrial Water Systems Carbosperse K-700 Water Treatment Polymers* tech. rep. Volume: 17 (ZIBEX, Inc, 2003).

12. Reddy, M. M. & Hoch, A. R. Calcite crystal growth rate inhibition by polycarboxylic acids. *Journal of Colloid and Interface Science* **235.** Publisher: Academic Press Inc., 365–370. ISSN: 00219797 (Mar. 2001).

13. Gebauer, D., Cölfen, H., Verch, A. & Antonietti, M. The Multiple Roles of Additives in CaCO3 Crystallization: A Quantitative Case Study. *Advanced Materials* **21,** 435–439. ISSN: 09359648, 15214095. https://onlinelibrary.wiley.com/doi/10.1002/adma.200801614 (2022) (Jan. 2009).

14. Kim, I. W., Robertson, R. E. & Zand, R. Effects of some nonionic polymeric additives on the crystallization of calcium carbonate. *Crystal Growth and Design* **5,** 513–522. ISSN: 15287483 (Mar. 2005).

15. Picker, A., Kellermeier, M., Seto, J., Gebauer, D. & Cölfen, H. The multiple effects of amino acids on the early stages of calcium carbonate crystallization. *Zeitschrift für Kristallographie - Crystalline Materials* **227,** 744–757. ISSN: 2194-4946. https://www.degruyter.com/document/doi/10.1524/zkri.2012.1569/html (2022) (Nov. 2012).

16. Deng, H., Shen, X. C., Wang, X. M. & Du, C. Calcium carbonate crystallization controlled by functional groups: A mini-review. *Frontiers of Materials Science* **7,** 62–68. ISSN: 2095025X (Mar. 2013).

17. Jafar Mazumder, M. A. A review of green scale inhibitors: Process, types, mechanism and properties. *Coatings* **10.** Publisher: MDPI AG, 1–29. ISSN: 20796412 (Oct. 2020).

18. Huang, S.-C., Naka, K. & Chujo, Y. A carbonate controlled-addition method for amorphous calcium carbonate spheres stabilized by poly (acrylic acid)s. *Langmuir* **23,** 12086–12095 (2007).

19. Huang, S.-C., Naka, K. & Chujo, Y. Effect of molecular weights of poly (acrylic acid) on crystallization of calcium carbonate by the delayed addition method. *Polymer Journal* **40,** 154–162 (2008).

20. Ouhenia, S., Chateigner, D., Belkhir, M., Guilmeau, E. & Krauss, C. Synthesis of calcium carbonate polymorphs in the presence of polyacrylic acid. *Journal of Crystal Growth* **310,** 2832–2841 (2008).

21. Gower, L. & Tirrell, D. Calcium carbonate films and helices grown in solutions of poly(aspartate). *Journal of Crystal Growth* **191,** 153–160. ISSN: 00220248. https://linkinghub.elsevier.com/retrieve/pii/S0022024898000025 (2022) (July 1998).

22. Aschauer, U., Ebert, J., Aimable, A. & Bowen, P. Growth modification of seeded calcite by carboxylic acid oligomers and polymers: toward an understanding of complex growth mechanisms. *Crystal Growth & Design* **10,** 3956–3963 (2010).

23. Schuitemaker, A., Raiteri, P. & Demichelis, R. The atomic structure and dynamics at the CaCO $_3$ vaterite–water interface: A classical molecular dynamics study. *The Journal of Chemical Physics* **154,** 164504. ISSN: 0021-9606, 1089-7690. https://aip.scitation.org/doi/10.1063/5.0049483 (2022) (Apr. 2021).

24. Raiteri, P., Gale, J. D., Quigley, D. & Rodger, P. M. Derivation of an Accurate Force-Field for Simulating the Growth of Calcium Carbonate from Aqueous Solution: A New Model for the Calcite–Water Interface. *The Journal of Physical Chemistry C* **114,** 5997–6010. ISSN: 1932-7447, 1932-7455. https://pubs.acs.org/doi/10.1021/jp910977a (2022) (Apr. 2010).

25. Raiteri, P., Demichelis, R. & Gale, J. D. Thermodynamically Consistent Force Field for Molecular Dynamics Simulations of Alkaline-Earth Carbonates and Their Aqueous Speciation. *The Journal of Physical Chemistry C* **119,** 24447–24458. ISSN: 1932-7447, 1932-7455. https://pubs.acs.org/doi/10.1021/acs.jpcc.5b07532 (2023) (Oct. 2015).

26. Fenter, P., Kerisit, S., Raiteri, P. & Gale, J. D. Is the Calcite–Water Interface Understood? Direct Comparisons of Molecular Dynamics Simulations with Specular X-ray Reflectivity Data. *The Journal of Physical Chemistry C* **117,** 5028–5042. ISSN: 1932-7447, 1932-7455. https://pubs.acs.org/doi/10.1021/jp310943s (2023) (Mar. 2013).

27. Liu, Z. *et al.* Charge-modulated calcite surface for anionic surfactant adsorption from molecular dynamics simulations. *Surfaces and Interfaces* **33,** 102234. ISSN: 24680230. https://linkinghub.elsevier.com/retrieve/pii/S2468023022005004 (2022) (Oct. 2022).

28. Chun, B. J., Lee, S. G., Choi, J. I. & Jang, S. S. Adsorption of carboxylate on calcium carbonate (10 1 4) surface: Molecular simulation approach. *Colloids and Surfaces A: Physicochemical and Engineering Aspects* **474.** Publisher: Elsevier B.V., 9–17. ISSN: 18734359 (June 2015).

29. Aschauer, U., Spagnoli, D., Bowen, P. & Parker, S. C. Growth modification of seeded calcite using carboxylic acids: Atomistic simulations. *Journal of Colloid and Interface Science* **346,** 226–231. ISSN: 00219797. https://linkinghub.elsevier.com/retrieve/pii/S0021979710002614 (2022) (2010).

30. Sparks, D. J. *et al.* Adsorption of poly acrylic acid onto the surface of calcite: An experimental and simulation study (SUPPLEMENTAL). *Physical Chemistry Chemical Physics* **17,** 27357–27365. ISSN: 1463-9076, 1463-9084. http://xlink.rsc.org/?DOI=C5CP00945F (2022) (2015).

31. Zhu, B., Xu, X. & Tang, R. Hydration layer structures on calcite facets and their roles in selective adsorptions of biomolecules: A molecular dynamics study. *The Journal of Chemical Physics* **139,** 234705. ISSN: 0021-9606, 1089-7690. http://aip.scitation.org/doi/10.1063/1.4848696 (2022) (Dec. 2013).

32. Glisman, A. *et al.* Adsorption isotherm and mechanism of Ca^{2+} binding to polyelectrolyte. *Langmuir* **40,** 6212–6219 (2024).

33. Glisman, A. *et al.* Multi-valent ion-mediated polyelectrolyte association and structure. *Macromolecules* **57,** 1941–1949 (2024).

34. De Leeuw, N. H. & Parker, S. C. *Surface Structure and Morphology of Calcium Carbonate Polymorphs Calcite, Aragonite, and Vaterite: An Atomistic Approach* tech. rep. (1998).

35. Michaels, A. & Morelos, O. Polyelectrolyte adsorption by kaolinite. *Industrial & Engineering Chemistry* **47,** 1801–1809 (1955).

36. Jo, S., Kim, T., Iyer, V. G. & Im, W. CHARMM-GUI: A web-based graphical user interface for CHARMM. *Journal of Computational Chemistry* **29,** 1859–1865 (2008).

37. Choi, Y. K. *et al.* CHARMM-GUI polymer builder for modeling and simulation of synthetic polymers. *Journal of Chemical Theory and Computation* **17,** 2431–2443 (2021).

38. Downs, R. T. & Hall-Wallace, M. The American Mineralogist crystal structure database. *American Mineralogist* **88,** 247–250 (2003).

39. Markgraf, S. A. & Reeder, R. J. High-temperature structure refinements of calcite and magnesite. *American Mineralogist* **70,** 590–600 (1985).

40. Ong, S. P. *et al.* Python Materials Genomics (pymatgen): A robust, open-source python library for materials analysis. *Computational Materials Science* **68,** 314–319 (2013).

41. Berendsen, H. J., van der Spoel, D. & van Drunen, R. GROMACS: A message-passing parallel molecular dynamics implementation. *Computer Physics Communications* **91,** 43–56 (1995).

42. Van Der Spoel, D. *et al.* GROMACS: Fast, flexible, and free. *Journal of Computational Chemistry* **26,** 1701–1718 (2005).

43. Abraham, M. J. *et al.* GROMACS: High performance molecular simulations through multi-level parallelism from laptops to supercomputers. *SoftwareX* **1,** 19–25 (2015).

44. Berendsen, H. J., Grigera, J. R. & Straatsma, T. P. The missing term in effective pair potentials. *Journal of Physical Chemistry* **91,** 6269–6271 (1987).

45. Wang, J., Wolf, R. M., Caldwell, J. W., Kollman, P. A. & Case, D. A. Development and testing of a general amber force field. *Journal of Computational Chemistry* **25,** 1157–1174 (2004).

46. Wang, J., Wang, W., Kollman, P. A. & Case, D. A. Automatic atom type and bond type perception in molecular mechanical calculations. *Journal of Molecular Graphics and Modelling* **25,** 247–260 (2006).

47. Sprenger, K., Jaeger, V. W. & Pfaendtner, J. The general AMBER force field (GAFF) can accurately predict thermodynamic and transport properties of many ionic liquids. *The Journal of Physical Chemistry B* **119,** 5882–5895 (2015).

48. Leontyev, I. V. & Stuchebrukhov, A. A. Electronic continuum model for molecular dynamics simulations. *The Journal of Chemical Physics* **130,** 085102. ISSN: 0021-9606, 1089-7690. `http://aip.scitation.org/doi/10.1063/1.3060164` (2022) (Feb. 2009).

49. Duboué-Dijon, E., Javanainen, M., Delcroix, P., Jungwirth, P. & Martinez-Seara, H. A practical guide to biologically relevant molecular simulations with charge scaling for electronic polarization. *The Journal of Chemical Physics* **153,** 050901. ISSN: 0021-9606, 1089-7690. `http://aip.scitation.org/doi/10.1063/5.0017775` (2022) (Aug. 2020).

50. Bonomi, M. *et al.* PLUMED: A portable plugin for free-energy calculations with molecular dynamics. *Computer Physics Communications* **180,** 1961–1972 (2009).

51. Tribello, G. A., Bonomi, M., Branduardi, D., Camilloni, C. & Bussi, G. PLUMED 2: New feathers for an old bird. *Computer Physics Communications* **185,** 604–613 (2014).

52. Bonomi, M. *et al.* Promoting transparency and reproducibility in enhanced molecular simulations. *Nature Methods* **16,** 670–673 (2019).

53. Darden, T., York, D. & Pedersen, L. Particle mesh Ewald: An N log (N) method for Ewald sums in large systems. *The Journal of Chemical Physics* **98,** 10089–10092 (1993).

54. Essmann, U. *et al.* A smooth particle mesh Ewald method. *The Journal of Chemical Physics* **103,** 8577–8593 (1995).

55. Hess, B., Bekker, H., Berendsen, H. J. & Fraaije, J. G. LINCS: A linear constraint solver for molecular simulations. *Journal of Computational Chemistry* **18,** 1463–1472 (1997).

56. Nosé, S. A unified formulation of the constant temperature molecular dynamics methods. *The Journal of Chemical Physics* **81,** 511–519 (1984).

57. Hoover, W. G. Canonical dynamics: Equilibrium phase-space distributions. *Physical Review A* **31,** 1695 (1985).

58. Parrinello, M. & Rahman, A. Polymorphic transitions in single crystals: A new molecular dynamics method. *Journal of Applied Physics* **52,** 7182–7190 (1981).

59. Invernizzi, M. & Parrinello, M. Rethinking Metadynamics: From Bias Potentials to Probability Distributions. *The Journal of Physical Chemistry Letters* (2020).

60. Rizzi, V., Aureli, S., Ansari, N. & Gervasio, F. L. OneOPES, a Combined Enhanced Sampling Method to Rule Them All. *Journal of Chemical Theory and Computation,* acs.jctc.3c00254. ISSN: 1549-9618, 1549-9626. https://pubs.acs.org/doi/10.1021/acs.jctc.3c00254 (2023) (Aug. 2023).

61. Invernizzi, M. & Parrinello, M. Exploration vs Convergence Speed in Adaptive-Bias Enhanced Sampling. *Journal of Chemical Theory and Computation* (2022).

62. Invernizzi, M., Piaggi, P. M. & Parrinello, M. Unified approach to enhanced sampling. *Physical Review X* **10,** 041034 (2020).

Part II

Hydrodynamic Self-Propulsion

Chapter 5

INTRODUCTION

This introductory chapter provides an overview of active matter systems and aspects of self-propulsion that serve to motivate our investigations. We describe previous studies of self-propulsion and collective phenomena in a fluid medium and highlight the open questions this work seeks to resolve. The subsequent chapters present mathematical derivations in potential flow theory and simulations of self-propelled bodies in Stokes as well as potential flow.

This chapter includes content from our previously published article:

1. Glisman, A. & Brady, J. F. Swimming in potential flow. *Journal of Fluid Mechanics* **962,** 11. `https://doi.org/10.1017/jfm.2022.946` (Nov. 2022).

5.1 Active Matter

Active matter is a class of materials that generate their own propulsive force, leading to net motion. This motion can arise from mechanisms such as phoresis [1] or internal body deformations [2–4]. A diverse range of active matter systems across different length scales is depicted in Fig. 5.1. In the natural world, organisms like fish and birds achieve propulsion by deforming their bodies within their fluid environments [5], while microorganisms such as *E. coli* utilize the rotation of flagellar bundles to shear the surrounding fluid [6]. Groups of these self-propelled entities can interact, leading to emergent phenomena, such as schooling and swarming [7]. The fascinating interplay between individual components and collective behavior is a hallmark of active matter systems. Moreover, the intriguing super-structures formed by self-propulsive bodies are not exclusive to biological systems, where some form of innate intelligence might be present, expanding the scope and potential applications of active matter studies.

Synthetic active systems, such as Janus spheres, are a promising area of exploration, particularly in understanding the dynamics of self-propelled bodies without biological complexity [9–13]. These spheres, which catalyze chemical decomposition on one hemisphere to self-propel through diffusiophoresis, serve as nano-motors without moving parts [14, 15]. The ability to manipulate these particles using external fields such as light [8] or acoustics [16] adds a layer of control, allowing researchers to investigate the underlying mechanisms leading to collective behavior.

In both biological and synthetic systems, we believe the fluid environment plays a crucial role in the dynamics of active matter systems. We focus on fluid-mediated interactions between self-propulsive bodies, and investigate how these interactions influence the motion of individual bodies and the resulting collective behavior of the system. The hydrodynamic feedback loop between individual bodies is essential: a single body's movement creates a fluid disturbance, influencing the motion of others, and thus reciprocally affecting its own trajectory. This feedback loop is a key feature of active matter systems generally, and we believe that it can be the source of emergent phenomena.

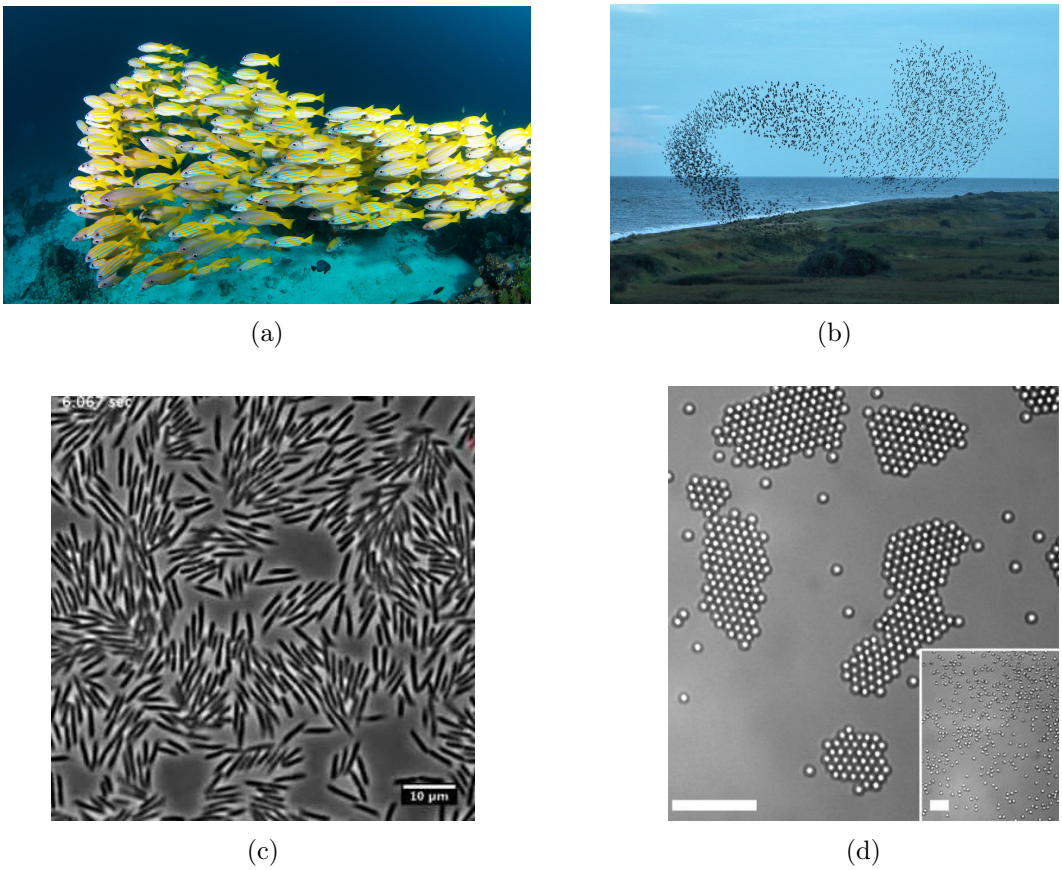

(a) (b) (c) (d)

Figure 5.1: Macroscopic examples of emergent phenomena: (a) fish schooling and (b) starlings flocking. Self-propulsive bodies also aggregate in the microscopic regime. (c, [7]) *E. coli* swarm and align with nearest neighbors. (d, [8]) Light-activated Janus particles cluster from a homogenous distribution (inset) as light catalyzes phoretic motion (scale bar 10 μm).

5.2 Hydrodynamics

The essential fluid mechanics vary between the microscopic (bacteria) and macroscopic (birds) regimes and are characterized by the Reynolds number, $Re := \rho_f \, U \, L / \mu$. The Reynolds number is a dimensionless number which quantifies the relative importance of inertial to viscous forces within the fluid medium [17–19] and spans many orders of magnitude in swimming and flying organisms (Fig. 5.2). The fluid density ρ_f and viscosity μ are material parameters, and the characteristic length L and velocity U scales in our systems are set by a body's length and average swim speed, respectively.

For microscopic systems, both characteristic velocity and length scales tend to be "small" such that $Re \ll 1$, and the Navier-Stokes equations of motion reduce to the linear Stokes equations. Self-propulsion in the Stokes regime

has been extensively studied with considerable knowledge about individual swimming mechanisms [2, 4, 20–23] and the interactions between swimming bodies that give rise to emergent phenomena [24–26].

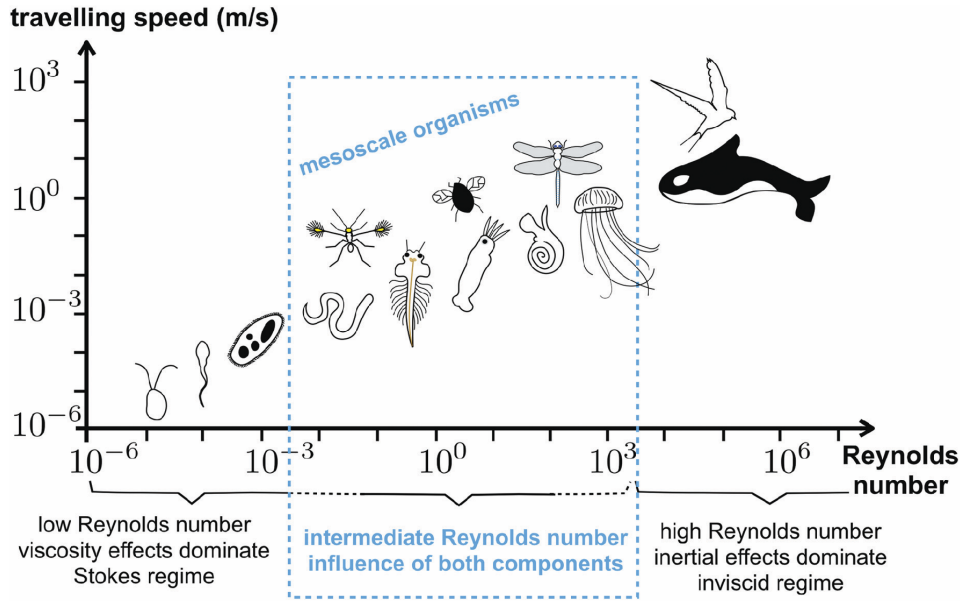

Figure 5.2: Reynolds numbers of swimming and flying animals from Ref. [27]. Organisms from left to right: algae, bacterium, paramecium, nematode, fairyfly, brine shrimp, larval squid, wasp, pteropod, dragonfly, jellyfish, whale, swallow.

Larger bodies, such as birds and fish, self-propel at high Reynolds numbers. With common material parameters [28, 29] and assumed characteristic scales of $\mathrm{L} = 0.1\,\mathrm{m}$ and $\mathrm{U} = 0.1\,\mathrm{m/s}$ as an approximation for both birds and fish, the Reynolds number for self-propulsion in air and water is 6×10^2 and 1×10^4, respectively. At these moderate and large Reynolds numbers, non-linear inertial terms within the Navier-Stokes equations become significant. The non-linearity of the Navier-Stokes equations makes the fluid mechanical problem significantly more computationally expensive to solve as well as making analytical insight more difficult to obtain. Of course, a finite element scheme for the fluid with deformable solid bodies can be constructed to solve for the fluid flow field. This method works very well with a few swimmers, especially when paired with statistical learning techniques [30]. However, collective phenomena by definition require large numbers of bodies, $O(10^3)$, and the full fluid mechanical solution becomes computationally intractable at this limit.

Historically, modeling emergent phenomena at high Reynolds number has avoided solution of the Navier-Stokes equations by neglecting the fluid medium entirely. The models instead introduce phenomenological rules for body interactions that lead to collective behavior. One of the most widespread models, the Vicsek model [31], assumes that each body will align its velocity vector with the average of its nearest neighbors—with added noise to prevent all trajectories from collapsing to a single point. The Vicsek model has also been generalized to account for more complex interactions between group members by incorporating relative orientational and rotational interactions [32–35]. While the Vicsek model can reproduce the group dynamics seen in fish schooling and birds flocking, the model only provides a phenomenological basis for the observed phenomena. We seek to investigate if the imposed "intelligence" is necessary for collective effects or if one can reproduce the same phenomena using a simple, mechanical model that explicitly accounts for fluid interactions.

5.3 Collective Phenomena in Potential Flow

By approximating the fluid flow as irrotational and incompressible, we can apply potential flow theory to create a much simpler model of the many-body hydrodynamic interactions [36–40]. The irrotational restriction is admittedly severe, and we are neglecting a physical phenomenon that has often been considered essential [5, 41, 42] for self-propulsion in high Reynolds flow: vortex shedding through the momentum boundary layer. Vorticity naturally exists in the wake and boundary layer surrounding the bodies, which may account for some aspect of collective motion. However, the vorticity sources have been shown to scale inversely with the Reynolds number for spherical bodies [43] and so might not be critical for modelling the hydrodynamics of certain classes of swimmers. Before discussing the feasibility of self-propulsion in potential flow, we begin with a few comments on how a potential flow may lead to collective effects.

In potential flow at high Reynolds number, the steady flow field reduces to the well-known Bernoulli's equation

$$p + \frac{1}{2}\,\rho_{\mathrm{f}}\,u^2 = \text{constant}\ , \tag{5.1}$$

which states that the fluid velocity and pressure are in a constant balance. The constant in Eq. (5.1) is the same for all points in the fluid domain. The simple form of Eq. (5.1) allows us to make a few qualitative statements about the fluid flow induced by a collection of solid bodies.

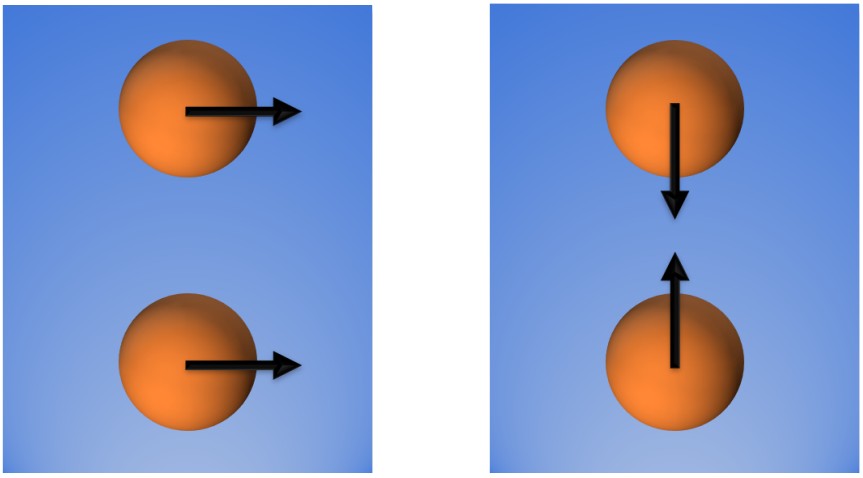

(a) (b)

Figure 5.3: Two spheres translating in a potential flow. (a) Two particles translating parallel to one another are attracted and (b) are repelled when translating towards their mutual center.

Two particles that are translating parallel to each other (Fig. 5.3a) cause the fluid between their line of centers to flow faster relative to the background velocity. By Bernoulli's equation, the pressure in the fluid between the particles must therefore be lower than the pressure in the surrounding fluid. Potential flow then presents a physical mechanism for bodies to aggregate and may be a source of emergent phenomena. If two particles are instead translating towards one another (Fig. 5.3b), they must push the fluid out of their mutual center. By symmetry, a stagnation point exists at the pair's central point, leading to a pressure maxima and fluid repulsive forces. As the fluid can both attract and repel bodies [44], it may therefore set a natural interaction length scale and aid in modeling collective phenomena.

5.4 Self-Propulsion in Potential Flow

Now that the possible mechanism for collective phenomena seen in Fig. 5.1 has been shown for potential flow, we return to the issue of self-propulsion. We have made two crucial fluid mechanical assumptions: the fluid flow is inviscid and irrotational. As we will show, viscous drag forces can be added

by using the Rayleigh dissipation function in a Lagrangian framework [45, 46]. However, the irrotational approximation cannot be relaxed in potential flow, and we must ask if vorticity is an essential element for self-propulsion.

Is a single fish or bird able to self-propel in an inviscid potential flow without modeling boundary layers? Thankfully, the answer is a resounding yes, and vorticity is not needed for self-propulsion at high Reynolds number. Saffman first demonstrated that net motion is possible for an inviscid swimmer in potential flow [3]. The result is especially interesting, as the net motion occurs without energetic dissipation. Saffman argued that by breaking the natural time-reversal symmetry inherent in an inviscid and irrotational flow, propulsion could be generated from the configuration-dependent hydrodynamic forces. Kanso & Marsden have continued to study self-propulsion potential flows by modelling swimming bodies as a collection of two-dimensional ellipsoids connected via hinges [40, 47, 48] and used control theory to determine the optimal articulation for various swimmer designs.

The question of what body deformations result in self-propulsion has been long debated in Stokes flow. Purcell first hypothesized the general deformation requirements for a Stokes swimmer in what is now referred to as the Scallop Theorem [49]. The Scallop Theorem states that in the time-reversible Stokes medium, a body must deform non-reciprocally to have net translation after one period of articulation. Non-reciprocal motion is not time-invariant and is distinct when viewed forwards and backward in time. It was named after the motion of an idealized scallop, which can only open and close about a single hinge. After one cycle of opening and closing, the scallop returns to its original position due to the time-reversible hydrodynamics. Purcell stated that at least two degrees of freedom must vary with some out-of-phase component to effect propulsion. More recent work by Chambrion & Munnier [50] revealed a more general requirement of self-propulsion that relied on geometric arguments instead of time-reversibility. They showed that net motion is possible when a linear mapping of the shape (deformational) variables to another linear space result in an open path and also proved the same principle holds in the inviscid regime [51] we seek to study.

5.5 Outline

In the following chapters, we develop a hydrodynamic model for a collection of rigid bodies in an inviscid, irrotational fluid. Chapter 6 presents the physical and mathematical details necessary to derive the equations of motion for a set of rigid bodies in an inviscid, irrotational fluid. We first derive the equations of motion for a collection of spherical particles in an inviscid potential flow and extend the model to account for viscous dissipation and rigid body motion. Chapter 7 then constructs a simple, three-link swimmer model and compares the self-propulsive motion between the Stokesian and inviscid limits.

References

1. Golestanian, R. Phoretic Active Matter. *arXiv preprint arXiv:1909.03747* (2019).
2. Najafi, A. & Golestanian, R. Simple swimmer at low Reynolds number: Three linked spheres. *Physical Review E* **69,** 062901 (2004).
3. Saffman, P. The self-propulsion of a deformable body in a perfect fluid. *Journal of Fluid Mechanics* **28,** 385–389 (1967).
4. Swan, J. W., Brady, J. F., Moore, R. S. & ChE 174. Modeling hydrodynamic self-propulsion with Stokesian Dynamics. Or teaching Stokesian Dynamics to swim. *Physics of Fluids* **23,** 071901 (2011).
5. Lighthill, S. J. *Mathematical biofluiddynamics* (SIAM, 1975).
6. Ishihara, A., Segall, J. E., Block, S. M. & Berg, H. C. Coordination of flagella on filamentous cells of Escherichia coli. *Journal of Bacteriology* **155,** 228–237 (1983).
7. Copeland, M. F. & Weibel, D. B. Bacterial swarming: A model system for studying dynamic self-assembly. *Soft Matter* **5,** 1174–1187 (2009).
8. Palacci, J. *et al.* Light-activated self-propelled colloids. *Philosophical Transactions of the Royal Society A: Mathematical, Physical and Engineering Sciences* **372,** 20130372 (2014).
9. Jiang, S. *et al.* Janus particle synthesis and assembly. *Advanced Materials* **22,** 1060–1071 (2010).
10. Chen, Q. *et al.* Supracolloidal reaction kinetics of Janus spheres. *Science* **331,** 199–202 (2011).
11. Ebbens, S., Tu, M.-H., Howse, J. R. & Golestanian, R. Size dependence of the propulsion velocity for catalytic Janus-sphere swimmers. *Physical Review E* **85,** 020401 (2012).
12. Zhang, J., Grzybowski, B. A. & Granick, S. Janus particle synthesis, assembly, and application. *Langmuir* **33,** 6964–6977 (2017).
13. Campbell, A. I., Ebbens, S. J., Illien, P. & Golestanian, R. Experimental observation of flow fields around active Janus spheres. *Nature Communications* **10,** 3952 (2019).
14. Howse, J. R. *et al.* Self-motile colloidal particles: from directed propulsion to random walk. *Physical Review Letters* **99,** 048102 (2007).
15. Buttinoni, I., Volpe, G., Kümmel, F., Volpe, G. & Bechinger, C. Active Brownian motion tunable by light. *Journal of Physics: Condensed Matter* **24,** 284129 (2012).
16. Takatori, S. C., De Dier, R., Vermant, J. & Brady, J. F. Acoustic trapping of active matter. *Nature Communications* **7,** 10694 (2016).

17. Reynolds, O. XXIX. An experimental investigation of the circumstances which determine whether the motion of water shall be direct or sinuous, and of the law of resistance in parallel channels. *Philosophical Transactions of the Royal Society of London,* 935–982 (1883).

18. Batchelor, C. K. & Batchelor, G. *An introduction to fluid dynamics* (Cambridge University Press, 2000).

19. Lamb, H. *Hydrodynamics* (University Press, 1924).

20. Taylor, G. I. Analysis of the swimming of microscopic organisms. *Proceedings of the Royal Society of London. Series A. Mathematical and Physical Sciences* **209,** 447–461 (1951).

21. Avron, J., Kenneth, O. & Oaknin, D. Pushmepullyou: An efficient microswimmer. *New Journal of Physics* **7,** 234 (2005).

22. Elgeti, J., Winkler, R. G. & Gompper, G. Physics of microswimmers–single particle motion and collective behavior: A review. *Reports on Progress in Physics* **78,** 056601 (2015).

23. Burkholder, E. W. *Single Particle Motion in Active Matter.* PhD thesis (California Institute of Technology, 2019).

24. Pooley, C., Alexander, G. & Yeomans, J. Hydrodynamic interaction between two swimmers at low Reynolds number. *Physical Review Letters* **99,** 228103 (2007).

25. Lauga, E. & Bartolo, D. No many-scallop theorem: Collective locomotion of reciprocal swimmers. *Physical Review E* **78,** 030901 (2008).

26. Marchetti, M. C. *et al.* Hydrodynamics of soft active matter. *Reviews of Modern Physics* **85,** 1143 (2013).

27. Klotsa, D. As above, so below, and also in between: Mesoscale active matter in fluids. *Soft Matter* **15,** 8946–8950 (2019).

28. *NIST Chemistry WebBook* Online. 2020.

29. *Material paramters:* $\rho^{\text{air}} = 1.2\,\text{kg/m}^3$, $\rho^{\text{water}} = 1000\,\text{kg/m}^3$, $\mu^{\text{air}} = 2 \times 10^{-5}\,\text{Pa} * \text{s}$, $\mu^{\text{water}} = 1 \times 10^{-3}\,\text{Pa} * \text{s}$,

30. Verma, S., Novati, G. & Koumoutsakos, P. Efficient collective swimming by harnessing vortices through deep reinforcement learning. *Proceedings of the National Academy of Sciences* **115,** 5849–5854 (2018).

31. Vicsek, T., Czirók, A., Ben-Jacob, E., Cohen, I. & Shochet, O. Novel type of phase transition in a system of self-driven particles. *Physical Review Letters* **75,** 1226 (1995).

32. Hendrickx, J. & Blondel, V. *Convergence of different linear and nonlinear Vicsek models* in *MTNS 2006* (2006).

33. Chaté, H., Ginelli, F., Grégoire, G., Peruani, F. & Raynaud, F. Modeling collective motion: variations on the Vicsek model. *The European Physical Journal B* **64,** 451–456 (2008).

34. Liu, Z. & Guo, L. Connectivity and synchronization of Vicsek model. *Science in China Series F: Information Sciences* **51,** 848–858 (2008).

35. Bolley, F., Cañizo, J. A. & Carrillo, J. A. Mean-field limit for the stochastic Vicsek model. *Applied Mathematics Letters* **25,** 339–343 (2012).

36. Kellogg, O. D. *Foundations of potential theory* (Courier Corporation, 1953).

37. Pozrikidis, C. & Jankowski, D. *Introduction to theoretical and computational fluid dynamics* (Oxford University Press New York, 1997).

38. Techet, A. Potential flow theory. *Lecture notes for the course* **2** (2005).

39. Yurkovetsky, Y. & Brady, J. F. Statistical mechanics of bubbly liquids. *Physics of Fluids* **8,** 881–895 (1996).

40. Kanso, E., Marsden, J. E., Rowley, C. W. & Melli-Huber, J. B. Locomotion of articulated bodies in a perfect fluid. *Journal of Nonlinear Science* **15,** 255–289 (2005).

41. Wu, T. Hydromechanics of swimming propulsion. Part 1. Swimming of a two-dimensional flexible plate at variable forward speeds in an inviscid fluid. *Journal of Fluid Mechanics* **46,** 337–355 (1971).

42. Wu, T., Brokaw, C. J. & Brennen, C. *Swimming and flying in nature* (Springer, 1975).

43. Moore, D. The boundary layer on a spherical gas bubble. *Journal of Fluid Mechanics* **16,** 161–176 (1963).

44. Hinch, E. & Nitsche, L. C. Nonlinear drift interactions between fluctuating colloidal particles: oscillatory and stochastic motions. *Journal of Fluid Mechanics* **256,** 343–401 (1993).

45. Goldstein, H., Poole, C. & Safko, J. *Classical mechanics* (American Association of Physics Teachers, 2002).

46. Minguzzi, E. Rayleigh's dissipation function at work. *European Journal of Physics* **36,** 035014 (2015).

47. Kanso, E. & Marsden, J. E. *Optimal motion of an articulated body in a perfect fluid* in *Proceedings of the 44th IEEE Conference on Decision and Control* (2005), 2511–2516.

48. Kanso, E. Swimming in an inviscid fluid. *Theoretical and Computational Fluid Dynamics* **24,** 201–207 (2010).

49. Purcell, E. M. Life at low Reynolds number. *American Journal of Physics* **45,** 3–11 (1977).

50. Munnier, A. & Chambrion, T. Generalized scallop theorem for linear swimmers. *arXiv* (2010).

51. Munnier, A. & PinÇon, B. Locomotion of articulated bodies in an ideal fluid: 2d model with buoyancy, circulation and collisions. *Mathematical Models and Methods in Applied Sciences* **20,** 1899–1940. ISSN: 02182025 (2010).

Chapter 6

HYDRODYNAMICALLY INTERACTING SWIMMERS IN POTENTIAL FLOW

This chapter presents the theoretical foundations necessary to derive the equations of motion for solid particles in potential flow. We employ a Lagrangian framework to derive the equations of motion for a collection of solid particles in an inviscid, irrotational flow. The focus is specifically on rigid spherical particles, although the principles of both potential flow and Lagrangian mechanics apply to arbitrary particle geometry and deformation. The discussion begins by reviewing the governing differential equations and boundary conditions of potential flow. Subsequently, the Lagrangian for the fluid and particles is formulated, and key physical characteristics are emphasized. The Lagrangian framework is then further expanded to incorporate aspects such as viscous dissipation and the hydrodynamic interaction among multiple rigid bodies, each composed of a collection of particles.

6.1 System Lagrangian

In this section, we derive the Lagrangian for a system of rigid spherical particles of radius a interacting within an inviscid potential flow. Potential flow theory is a mathematical framework for describing the motion of an incompressible and irrotational flow. It is commonly employed to model the motion of fluids at high Reynolds number, where viscous forces are negligible. In an irrotational and incompressible flow, it can be shown that the fluid velocity field is the gradient of a scalar potential $\boldsymbol{u} = \nabla\phi$ [1, 2]. Substitution of ϕ into the equation of mass conservation for an incompressible fluid results in Laplace's equation at all points in the fluid domain

$$\nabla^2\phi = 0 \ . \tag{6.1}$$

The edges of the fluid domain are defined by the surfaces of a set of particles $\partial\Omega_\alpha$, where α is the particle index. No-flux boundary conditions are enforced on all particle boundaries as

$$\nabla\phi|_{\partial\Omega_\alpha} \cdot \boldsymbol{n} = \boldsymbol{U}_\alpha \cdot \boldsymbol{n} \ , \tag{6.2}$$

where $\boldsymbol{n}$ is the unitary outward pointing normal (from the particle into the fluid) and $\boldsymbol{U}_\alpha$ contains the translational and rotational velocity components of the particle. We focus on spherical particles, allowing us to neglect rotational motion about the particle center in evaluating the boundary conditions. Infinitely far from the particles, we assume the fluid is at rest such that the potential decays to an arbitrary reference value, which we set to zero: $\phi(\,|\boldsymbol{x}| \to \infty) = 0$.

The fluid potential contains the information necessary to calculate the fluid velocity field and, thus, the fluid-mediated interactions between particles. Instead of explicitly solving for the potential, we can formulate the Lagrangian for the system and derive the equations of motion for the particles from Lagrangian mechanics. The kinetic energy of the fluid can be calculated as

$$\mathcal{T}^{\mathrm{f}} = \frac{1}{2}\,\rho_{\mathrm{f}} \int_\Omega \boldsymbol{u} \cdot \boldsymbol{u}\, dV \ . \tag{6.3}$$

Substitution of the potential solution and application of the divergence theorem yields

$$\mathcal{T}^{\mathrm{f}} = -\frac{1}{2}\,\rho_{\mathrm{f}} \sum_{\alpha=1}^{N} \left(\int_{\partial\Omega_\alpha} \phi\, \boldsymbol{n}\, dS \right) \cdot \boldsymbol{U}_\alpha \ , \tag{6.4}$$

where we have defined the number of particles N and fluid mass density ρ_f [3]. The negative sign in Eq. (6.4) is due to the convention of the normal vector pointing into the fluid domain from the solid. As Laplace's equation (Eq. (6.1)) is a linear partial differential equation, the solution must be linear in the particle velocity via the no-flux boundary conditions

$$\phi(\boldsymbol{x}) = \sum_{\alpha=1}^{N} \boldsymbol{\Phi}_\alpha(\boldsymbol{x}; \{\boldsymbol{x} - \boldsymbol{R}_\alpha\}) \cdot \boldsymbol{U}_\alpha \ . \tag{6.5}$$

The center position of particle α is denoted by $\boldsymbol{R}_\alpha$. As a given particle moves, it will displace the surrounding fluid and create a potential disturbance. The disturbance decays with distance from the particle center [4, 5] and is reflected in the $\boldsymbol{\Phi}_\alpha$ configuration dependence.

The potential solution is calculated via a multipole expansion of the potential field about the particle centers. A translating sphere creates a dipolar potential disturbance $O(r^{-2})$ at leading order [2, 3], and higher order polar moments can be neglected, as shown in Bonnecaze & Brady [6, 7]. Substitution of Eq. (6.5) into Eq. (6.4) simplifies the kinetic energy into a quadratic form of the particle velocities. We simplify the vector notation by stacking the individual particle velocity vectors ($\boldsymbol{U} = [\boldsymbol{U}_1, \boldsymbol{U}_2, \ldots, \boldsymbol{U}_N]^\mathrm{T}$) and writing the fluid kinetic energy as

$$\mathcal{T}^\mathrm{f} = \frac{1}{2}\, \rho_\mathrm{f}\, V\, \boldsymbol{U} \cdot \tilde{\mathsf{M}} \cdot \boldsymbol{U} \ , \tag{6.6}$$

with spherical particle volume $V = (4/3)\,\pi\, a^3$. The remaining surface integral is grouped into the added mass matrix, denoted as $\tilde{\mathsf{M}}$. The added mass between two particles α and β is defined as

$$\tilde{\mathsf{M}}_{\alpha\beta}(\{\boldsymbol{R}_\gamma\}) \coloneqq -\frac{1}{V} \int_{\partial\Omega_\beta} \boldsymbol{\Phi}_\alpha\, \boldsymbol{n}\, dS \ , \tag{6.7}$$

and it is dependent on the configuration of all $\boldsymbol{R}_\gamma$ particles in the system. The added mass matrix physically captures the effective increase in inertia that a particle (or pair of particles) experiences due to the interactions with all other particles and is the source of the interesting phenomena we study. Note that, as defined, the added mass matrix is dimensionless. Each matrix element (i.e., $\tilde{\mathsf{M}}_{\alpha\beta}$) in general contains four substituent sub-matrices due to the velocity vector containing both linear and angular motion: translation-translation, translation-rotation, rotation-translation, and rotation-rotation coupling elements. Only translational motion affects the added mass for spherical particles,

so only the translation-translation coupling elements are non-zero in our studies. Consequently, we will only discuss the translation-translation elements of the added mass matrix.

The added mass matrix is calculated via a Taylor expansion of the potential $\boldsymbol{\Phi}$ about particle center positions and is described in detail in Sec. 6.3. The constant term in the expansion is zero by symmetry (the spherical normal is an odd function over the surface). Therefore, the added mass is proportional to the gradient of the dipolar potential at leading order, which is $O(r^{-3})$. An isolated translating spherical particle has the well-known added mass of

$$\tilde{\mathsf{M}} = \frac{1}{2}\mathbf{I} \,, \tag{6.8}$$

and the added mass that one sphere α of experiences from dipole-dipole interactions with one other sphere β is

$$\tilde{\mathsf{M}}_{\alpha\beta} = \frac{a^3}{2}\left(\frac{1}{|\boldsymbol{r}|^3}\,\mathbf{I} - \frac{3}{|\boldsymbol{r}|^5}\,\boldsymbol{r}\otimes\boldsymbol{r}\right) \,, \tag{6.9}$$

where $\boldsymbol{r} = \boldsymbol{R}_\alpha - \boldsymbol{R}_\beta$ and $\otimes$ denotes the outer (dyadic) product.

We must now add the particles' intrinsic kinetic energy to solve the Lagrangian of the entire system. We define the intrinsic particle mass tensor as $\hat{\mathsf{M}}$. The intrinsic mass tensor is diagonal with non-zero elements on the translation-translation coupling elements. The rotational kinetic energy coupling matrix is similarly defined using the intrinsic moment of inertia $\hat{\mathsf{J}}$ and is diagonal with non-zero elements on the rotation-rotation matrix elements

$$\hat{\mathsf{M}}_{\alpha\alpha} = \rho\, V \begin{pmatrix} \mathbf{I} & \mathbf{0} \\ \mathbf{0} & \mathbf{0} \end{pmatrix} \quad \Big| \quad \hat{\mathsf{J}}_{\alpha\alpha} = \frac{2}{5}\rho\, V\, a^2 \begin{pmatrix} \mathbf{0} & \mathbf{0} \\ \mathbf{0} & \mathbf{I} \end{pmatrix} \,, \tag{6.10}$$

with particle density ρ. The total mass matrix is given as the sum of the added mass, intrinsic mass, and intrinsic moment of inertia matrices as

$$\mathsf{M} \coloneqq \rho_\mathrm{f}\, V\, \tilde{\mathsf{M}} + \hat{\mathsf{M}} + \hat{\mathsf{J}} \,, \tag{6.11}$$

and the total system kinetic energy is then given by

$$\mathcal{T} = \frac{1}{2}\boldsymbol{U}\cdot\mathsf{M}\cdot\boldsymbol{U} \,. \tag{6.12}$$

We assume no external fields are acting on the fluid (i.e., constant potential energy) such that the fluid contribution to the Lagrangian is equal to the fluid kinetic energy alone. We can add an arbitrary conservative particle potential $\mathcal{V}^\mathrm{p}$, such as harmonic springs to connect particles or a WCA potential

to prevent particle overlap. Non-conservative potentials can also be included through the Rayleigh dissipation function [8, 9] and we discuss viscous dissipative forces in Sec. 6.4. The total Lagrangian is then

$$\mathcal{L} = \mathcal{T} - \mathcal{V} = \frac{1}{2}\boldsymbol{U}\cdot\mathsf{M}\cdot\boldsymbol{U} - \mathcal{V}^{\mathrm{p}} \ . \tag{6.13}$$

6.2 Unconstrained Equations of Motion

Lagrange's equation of motion conserves energy via the principle of least action, and for a set of unconstrained particles, it is given as

$$\frac{d}{dt}\left(\frac{\partial\mathcal{L}}{\partial\boldsymbol{U}}\right) - \frac{\partial\mathcal{L}}{\partial\boldsymbol{R}} = 0 \ . \tag{6.14}$$

Substitution of Eq. (6.12) into Eq. (6.14) and calculation of the partial derivatives yields the following equation of motion for each particle dimension

$$M_{kj}\,\dot{U}_j = \frac{1}{2}U_i\,\frac{\partial M_{ij}}{\partial R_k}\,U_j - \frac{\partial M_{kj}}{\partial R_i}\,U_i\,U_j - \frac{\partial\mathcal{V}^{\mathrm{p}}}{\partial R_k} \ . \tag{6.15}$$

We made use of the symmetry of the mass tensor ($M_{ij} = M_{ji}$). We also used the product rule to convert time derivatives of the mass tensor into spatial derivatives contracted with the velocity components. In this chapter, we employ Einstein summation convention, which implies summation over repeated indices. Greek indices α, β, γ account for particle number, each containing six entries (three linear and three angular coordinates). Roman indices i, j, k are the Cartesian components of the translational and angular degrees of freedom, and each index contains a single entry.

From the form of Eq. (6.15), it is clear that the configuration-dependent added mass must be the source of self-propulsion in the potential regime. If the added mass was independent of the particle configuration, the equations of motion immediately reduce to Newton's equations for constant mass particles

$$M_{kj}\,\dot{U}_j = -\frac{\partial\mathcal{V}^{\mathrm{p}}}{\partial R_k} \ , \tag{6.16}$$

and self-propulsion would not be possible by only varying the particle configuration. The importance of the configuration-dependent added mass can also be directly seen from the hydrodynamic forces. Hinch & Nitsche [5] proved that the hydrodynamic pressure forces (exerted by the fluid on the particles) could be related to the fluid kinetic energy terms in Lagrange's equation (Eq. (6.14))

$$\mathbf{F}^{\mathrm{P}} = -\frac{d}{dt}\left(\frac{\partial\mathcal{T}^{\mathrm{f}}}{\partial\boldsymbol{U}}\right) + \frac{\partial\mathcal{T}^{\mathrm{f}}}{\partial\boldsymbol{R}} \ . \tag{6.17}$$

The particles then have two ways to interact hydrodynamically; they may either accelerate their surrounding fluid ($\dot{\boldsymbol{U}} \neq \mathbf{0}$), or vary their relative configuration to modify the hydrodynamic added mass (cf. Eq. (6.6)). Notably, the terms related to acceleration are longer-ranged, as they contract the mass tensor directly, whereas terms related to configuration variation scale as the mass tensor gradient. An isolated particle traveling at constant velocity consequently experiences no net hydrodynamic force, commonly referred to as D'Alembert's paradox [10].

We finally turn to the particle momentum in order to determine all canonical coordinates and define it as

$$\mathbf{P} \coloneqq \boldsymbol{M}\,\boldsymbol{U} \ . \tag{6.18}$$

The total linear momentum of the system is then given by

$$\mathbf{P}^{\mathrm{t}} = \sum_{\alpha=1}^{N} \mathbf{P}_{\alpha} \ , \tag{6.19}$$

and can be viewed as the impulse required from the fluid to accelerate all particles from rest to their current state. If the potential energy $\mathcal{V}^{\mathrm{p}}$ is purely internal to the system, the Lagrangian will only depend on relative configuration and not absolute particle positions. This implies that the Lagrangian must be invariant to a rigid spatial translation of the entire system (i.e., $\sum_{\alpha} \frac{\partial \mathcal{L}}{\partial \boldsymbol{R}_{\alpha}} = \mathbf{0}$). Lagrange's equation of motion (Eq. (6.14)) then reduces to $\dot{\mathbf{P}}^{\mathrm{t}} = \mathbf{0}$.

We now have two conserved quantities in potential flow: total energy $\mathcal{T} + \mathcal{V}$ and total linear momentum $\mathbf{P}^{\mathrm{t}}$ [4]. The total energy is also known as the Hamiltonian $\mathcal{H} = \mathcal{T} + \mathcal{V}$, and its conservation allows the application of equilibrium statistical mechanics, as Yurkovetsky & Brady showed in bubbly liquid systems [3]. With a defined Hamiltonian, the collection of particles can be treated as a canonical ensemble, a partition function can be constructed, and thermodynamic phase behavior can be analyzed.

6.3 Calculation of the Added Mass Tensor

Before extending the equations of motion to include rigid body motion and dissipative forces, we must determine the added mass tensor for a set of spherical particles to close the hydrodynamic interactions. As shown in Eq. (6.4), the added mass tensor is given as a surface integral over the potential flow solution $\boldsymbol{\Phi}$. Calculation of $\boldsymbol{\Phi}$ is simplified by expanding the potential flow solution

in a multipole expansion of Laplace's equation (Eq. (6.1)). The monopole is identically zero for constant volume particles, and the dipole captures the no-flux boundary condition. The hydrodynamic disturbances (velocity field) scale as the gradient of the potential, indicating the interactions between particles scale as $O(r^{-3})$, where r is the distance between their centers.

A detailed derivation of the mass tensor is found in Yurkovetsky & Brady [3]. This section focuses on the critical steps in calculating the added mass tensor for analytical and numerical solutions. Following [3], the added mass tensor is decomposed into two constituent tensors, $\tilde{\mathsf{M}}^{(1)}$ and $\tilde{\mathsf{M}}^{(2)}$, as

$$\tilde{\mathsf{M}} := -\left(\mathbf{I} - \tilde{\mathsf{M}}^{(1)}\right)^{-1} \tilde{\mathsf{M}}^{(2)} \ . \tag{6.20}$$

Each 3×3 sub-tensor in $\tilde{\mathsf{M}}^{(1)}$ (i.e., $\tilde{\mathsf{M}}^{(1)}_{\alpha\beta}$) physically describes the dipole-dipole hydrodynamic interactions between a pair of isolated particles, and the inversion operation represents the scattering of all hydrodynamic interactions. The second constituent mass tensor $\tilde{\mathsf{M}}^{(2)}$ can be directly calculated from $\tilde{\mathsf{M}}^{(1)}$ by

$$\tilde{\mathsf{M}}^{(2)} = -\tilde{\mathsf{M}}^{(1)} - \frac{1}{2}\mathbf{I} \ , \tag{6.21}$$

and is defined for notational convenience. The first constituent added mass tensor is then defined as

$$\tilde{\mathsf{M}}^{(1)}_{\alpha\beta} := -\frac{a^3}{2} \nabla_{\boldsymbol{y}} \nabla_{\boldsymbol{y}} |\boldsymbol{R}_{\alpha\beta}|^{-1} \tag{6.22}$$

for particle α different from particle β, where both particles are assumed to have constant spherical radius a and be separated by a distance $|\boldsymbol{R}_{\alpha\beta}|$. Note that $|\boldsymbol{R}_{\alpha\beta}|$ is a scalar describing the distance between particles, not a second-order tensor, and the repeated $\boldsymbol{y}$ index is not summed over. The gradients are with respect to the displacement between the pair as $\boldsymbol{y} = \boldsymbol{R}_\beta - \boldsymbol{R}_\alpha$. The second-order gradient is then given explicitly by

$$\tilde{\mathsf{M}}^{(1)}_{\alpha\beta} = -\frac{a^3}{2}\left(\frac{3}{|\boldsymbol{R}_{\alpha\beta}|^5}\, \boldsymbol{R}_{\alpha\beta} \otimes \boldsymbol{R}_{\alpha\beta} - \frac{1}{|\boldsymbol{R}_{\alpha\beta}|^3}\, \mathbf{I}\right) \ , \tag{6.23}$$

where indices α and β are not summed over. All 3×3 sub-tensors on the diagonal of $\tilde{\mathsf{M}}^{(1)}$ are the zero tensor.

In order to close the particle equations of motion, the gradient of the added mass tensor with respect to the particle centers is required (cf. Eq. (6.15)). We denote gradients of a tensor with respect to a vector as a third-order

tensor, where the first two indices are the original tensor element indices and the third index is the vector (gradient) index. A comma separates the last index to indicate that the gradient is with respect to that index. The gradient introduces an anti-symmetry into the added mass tensor, as a given element is dependent on $\boldsymbol{R}_\alpha - \boldsymbol{R}_\beta$. Exploiting these symmetries yields the following simplifications to the calculation of the added mass tensor gradient

$$\tilde{\mathsf{M}}^{(1)}_{\alpha\beta,\alpha} = \tilde{\mathsf{M}}^{(1)}_{\beta\alpha,\alpha} = -\tilde{\mathsf{M}}^{(1)}_{\alpha\beta,\beta} = -\tilde{\mathsf{M}}^{(1)}_{\beta\alpha,\beta} \ . \tag{6.24}$$

The repetition of indices in Eq. (6.24) does not imply Einstein summation convention, merely making explicit the fact that the gradient particle position coordinates must be one of the two particles in the mass tensor element.

The gradient of the first constituent added mass tensor (Eq. (6.22)) with respect to the particle center $\boldsymbol{R}_\gamma$ is then given by

$$\begin{aligned}\left(M^{(1)}_{\alpha\beta,\gamma}\right)_{ijk} =& (\delta_{\alpha\gamma} - \delta_{\beta\gamma})\left(\frac{-3\,a^3}{2\,|\boldsymbol{R}_{\alpha\beta}|^5}\left(\delta_{ij}\,(\boldsymbol{R}_{\alpha\beta})_k + \delta_{ik}\,(\boldsymbol{R}_{\alpha\beta})_j + \delta_{jk}\,(\boldsymbol{R}_{\alpha\beta})_i\right)\right. \\ &\left. + \frac{15\,a^3}{2\,|\boldsymbol{R}_{\alpha\beta}|^7}\left(\boldsymbol{R}_{\alpha\beta} \otimes \boldsymbol{R}_{\alpha\beta} \otimes \boldsymbol{R}_{\alpha\beta}\right)_{ijk}\right) \ ,\end{aligned} \tag{6.25}$$

where Roman indices (i.e., i, j, k) are Cartesian components of the added mass tensor gradient between particles α and β with respect to particle γ. The calculation of the full added mass tensor (Eq. (6.20)) gradient is non-trivial, as it requires the gradient of the inverse of a tensor (i.e., $\nabla(\mathbf{I} - \tilde{\mathsf{M}}^{(1)})^{-1}$). We seek a closed-form equation for the gradient without calculating the inverse analytically. We define the inverse tensor $\boldsymbol{A}$ as

$$\boldsymbol{A} = \boldsymbol{B}^{-1} \coloneqq (\mathbf{I} - \tilde{\mathsf{M}}^{(1)})^{-1} \ . \tag{6.26}$$

Analytical calculation of the inverse tensor gradient can be simplified by using the identity tensor δ_{ij} to define $\nabla(\boldsymbol{B}^{-1})$ in terms of $\nabla\boldsymbol{B}$ and $\boldsymbol{B}^{-1}$ itself

$$\begin{aligned}
\delta_{ij} &= B_{ik}\, B^{-1}_{kj} \\
\frac{\partial}{\partial x_l}\Big(\delta_{ij}\Big) = 0 &= \frac{\partial B_{ik}}{\partial x_l}\, B^{-1}_{kj} + B_{ik}\, \frac{\partial B^{-1}_{kj}}{\partial x_l} \\
B_{ik}\, \frac{\partial B^{-1}_{kj}}{\partial x_l} &= -\frac{\partial B_{ik}}{\partial x_l}\, B^{-1}_{kj} \\
B^{-1}_{mi}\, B_{ik}\, \frac{\partial B^{-1}_{kj}}{\partial x_l} &= -B^{-1}_{mi}\, \frac{\partial B_{ik}}{\partial x_l}\, B^{-1}_{kj} \\
\delta_{mk}\, \frac{\partial B^{-1}_{kj}}{\partial x_l} &= -B^{-1}_{mi}\, \frac{\partial B_{ik}}{\partial x_l}\, B^{-1}_{kj} \\
\frac{\partial B^{-1}_{mj}}{\partial x_l} &= -B^{-1}_{mi}\, \frac{\partial B_{ik}}{\partial x_l}\, B^{-1}_{kj} \\
\nabla(\boldsymbol{B}^{-1}) &= -\boldsymbol{B}^{-1} \cdot \nabla\boldsymbol{B} \cdot \boldsymbol{B}^{-1}\ .
\end{aligned} \tag{6.27}$$

Using Eq. (6.26) and the chain rule, we can calculate the gradient of the inverse tensor $\boldsymbol{A}$ as

$$\nabla\boldsymbol{A} = \boldsymbol{A} \cdot \nabla\tilde{\mathbf{M}}^{(1)} \cdot \boldsymbol{A}\ . \tag{6.28}$$

The full added mass tensor gradient is then given by

$$\begin{aligned}
\frac{\partial \tilde{M}_{ij}}{\partial x_l} &= -\frac{\partial A_{ik}}{\partial x_l}\, \tilde{M}^{(2)}_{kj} - A_{ik}\, \frac{\partial \tilde{M}^{(2)}_{kj}}{\partial x_l} \\
&= A_{im}\, \frac{\partial B_{mn}}{\partial x_l}\, A_{nk}\, \tilde{M}^{(2)}_{kj} - A_{ik}\, \frac{\partial \tilde{M}^{(2)}_{kj}}{\partial x_l} \\
&= -A_{im}\, \frac{\partial \tilde{M}^{(1)}_{mn}}{\partial x_l} A_{nk} \tilde{M}^{(2)}_{kj} - A_{ik} \frac{\partial \tilde{M}^{(2)}_{kj}}{\partial x_l} \\
&= A_{im}\, \frac{\partial \tilde{M}^{(1)}_{mn}}{\partial x_l} \tilde{M}_{nj} + A_{ik}\, \frac{\partial \tilde{M}^{(1)}_{kj}}{\partial x_l} \\
&= A_{im} \left(\frac{\partial \tilde{M}^{(1)}_{mn}}{\partial x_l}\, \tilde{M}_{nj} + \frac{\partial \tilde{M}^{(1)}_{mj}}{\partial x_l} \right) \\
&= A_{im}\, \frac{\partial \tilde{M}^{(1)}_{mn}}{\partial x_l} \Big(\tilde{M}_{nj} + \delta_{nj} \Big)\ .
\end{aligned} \tag{6.29}$$

With the form of the Lagrangian from Sec. 6.1, and the explicit form of the added mass matrix and its gradient, we can now calculate the particle equations of motion using Lagrangian mechanics.

6.4 Viscous Dissipation

The Rayleigh dissipation theorem [8, 9] allows one to include viscous dissipation in the Lagrangian framework. This approach has the advantage of relaxing the inviscid flow assumption but still requires the flow to be incompressible and irrotational. The rate of energetic dissipation for a fluid with viscosity μ is given by

$$\dot{\mathrm{E}}^{\mathrm{v}} = 2\,\mu \int_{\Omega} \mathbf{e} : \mathbf{e}\; dV \;. \tag{6.30}$$

The symmetric rate of strain tensor $\mathbf{e}$ double contraction can be rewritten in terms of the scalar potential as

$$\dot{\mathrm{E}}^{\mathrm{v}} = 2\,\mu \int_{\Omega} \nabla\nabla\phi : \nabla\nabla\phi\; dV \;. \tag{6.31}$$

The potential is then once again expanded in a linear form of the boundary conditions (Eq. (6.5)), and the divergence theorem is applied to simplify Eq. (6.31) as

$$\dot{\mathrm{E}}^{\mathrm{v}} = -2\,\mu\, \boldsymbol{U}_{\alpha} \cdot \left(\int_{\partial\Omega_{\lambda}} (\nabla\nabla\boldsymbol{\Phi}_{\alpha}) : (\nabla\boldsymbol{\Phi}_{\beta}\, \boldsymbol{n}_{\lambda})\, dS \right) \cdot \boldsymbol{U}_{\beta} \;. \tag{6.32}$$

Note that the energetic dissipation rate is a three-body interaction between two particles integrated over the surface of the third particle. The potential field is then solved for the dipole disturbances via Faxén-type laws relating the potential at a particle center (λ) to the potential existing in at that same point in the absence of that particle

$$\boldsymbol{\Phi}_{\gamma}(\boldsymbol{x}) = \frac{a^3}{2} \left(\nabla \frac{1}{|\boldsymbol{x} - \boldsymbol{R}_{\nu}|} \right) \cdot \left[\frac{2}{3}\, \tilde{\mathsf{M}}^{(1)}_{\nu\psi} \cdot \left(\tilde{\mathsf{M}}_{\psi\gamma} + \mathbf{I}\, \delta_{\psi\gamma} \right) + \mathbf{I}\, \delta_{\nu\gamma} \right] \;. \tag{6.33}$$

The dissipation rate can be written in a quadratic form of the particle velocities as

$$\dot{\mathrm{E}}^{\mathrm{v}} = \boldsymbol{U}_{\alpha} \cdot \boldsymbol{\mathcal{R}}_{\alpha\beta} \cdot \boldsymbol{U}_{\beta} \;, \tag{6.34}$$

where we group the surface integral and constants into the Rayleigh dissipation tensor $\boldsymbol{\mathcal{R}}_{\alpha\beta}$. We further decompose the Rayleigh dissipation tensor into a sum of sub-tensors for notational convenience

$$\boldsymbol{\mathcal{R}}_{\alpha\beta} = a\,\mu \sum_{\lambda=1}^{N} \left(\boldsymbol{N}_{\alpha\nu} \cdot \boldsymbol{C}_{\nu\eta;\lambda} \cdot \boldsymbol{N}_{\eta\beta} \right) \;. \tag{6.35}$$

The semicolon denotes that the sub-tensor $\boldsymbol{C}_{\nu\eta}$ is parametrically dependent on the integration surface of particle λ. Constant terms with respect to the integration surface are removed from the integral and denoted via tensor $\boldsymbol{N}$

as

$$\boldsymbol{N}_{\nu\gamma} = \frac{2}{3}\,\tilde{\mathbf{M}}^{(1)}_{\nu\psi} \cdot \left(\tilde{\mathbf{M}}_{\psi\gamma} + \mathbf{I}\,\delta_{\psi\gamma}\right) + \mathbf{I}\,\delta_{\nu\gamma}\ . \tag{6.36}$$

The analytic solution of the remaining surface integral requires a Taylor expansion of the potential fields for a given particle pair ν and η of interest over the surface of particle λ. In general, λ can be either ν, η, or all three can be identical. The leading order expansions yield different analytical forms for each set of $\{\eta,\, \nu,\, \lambda\}$ particles depending on their relationship and is summarized in tensor form as

$$\boldsymbol{C}_{\nu\eta;\lambda} = \begin{cases} -12\,\pi\,\mathbf{I} & \lambda = \eta,\ \nu = \eta \\ \mathbf{0} & \lambda = \eta,\ \nu \neq \eta \\ 8\,\pi\,\tilde{\mathbf{M}}^{(1)}_{\eta\nu} & \lambda = \nu,\ \nu \neq \eta \\ \frac{8\,\pi}{3}\,\nabla\tilde{\mathbf{M}}^{(1)}_{\lambda\nu} : \nabla\tilde{\mathbf{M}}^{(1)}_{\lambda\eta} & \lambda \neq \nu,\ \nu \neq \eta \quad (\lambda \text{ not summed over}) \end{cases} . \tag{6.37}$$

By the Rayleigh dissipation theorem, the viscous dissipative force can then be calculated via the velocity derivative as

$$\mathbf{F}^{\mathrm{v}} = -\frac{1}{2}\frac{\partial \dot{\mathrm{E}}^{\mathrm{v}}}{\partial \boldsymbol{U}} = -\boldsymbol{\mathcal{R}} \cdot \boldsymbol{U}\ . \tag{6.38}$$

We recover the well-known isolated sphere viscous drag of $\mathbf{F}^{\mathrm{v}} = -12\,\pi\,a\,\mu\,\boldsymbol{U}$ in potential flow. The viscous forces can then be added to the right-hand side of the particle equations of motion in Eq. (6.15) to add viscous dissipation to the system. Note that this will destroy the conservation of total energy in the system.

6.5 Many Rigid Bodies

The unconstrained equations of motion in Sec. 6.2 can be extended to account for multiple rigid bodies consisting of connected spheres. Each body is defined by a "locater" point $\boldsymbol{R}_{\mathrm{C}}$ about which the body rotates and translates. The motion of each particle is then decomposed into rigid body motion and constrained articulation relative to the locater point as

$$\boldsymbol{U}_{\alpha} = \boldsymbol{\mathcal{U}}_{\mathrm{C}} + \boldsymbol{\Omega}_{\mathrm{C}} \times \boldsymbol{r}_{\alpha} + \dot{\boldsymbol{r}}_{\alpha}\ , \tag{6.39}$$

where we have defined the rigid body linear $\boldsymbol{\mathcal{U}}_{\mathrm{C}}$ and angular $\boldsymbol{\Omega}_{\mathrm{C}}$ velocities and moment arm about the body's locater point $\boldsymbol{r}_{\alpha} = \boldsymbol{R}_{\alpha} - \boldsymbol{R}_{\mathrm{C}}$. The rigid body motion terms are simplified with the rigid body motion tensor $\boldsymbol{\Sigma}$, and the particle velocity vectors are stacked into

$$\boldsymbol{U} = \boldsymbol{\Sigma}^{\mathrm{T}} \cdot \dot{\boldsymbol{\xi}} + \dot{\boldsymbol{r}}\ , \tag{6.40}$$

where we have grouped the rigid motion into a single vector

$$\dot{\boldsymbol{\xi}} = [\boldsymbol{\mathcal{U}}_{\mathrm{C1}}, \boldsymbol{\Omega}_{\mathrm{C1}}, \ldots \boldsymbol{\mathcal{U}}_{\mathrm{C2}}, \boldsymbol{\Omega}_{\mathrm{C3}}, \ldots \boldsymbol{\mathcal{U}}_{\mathrm{CM}}, \boldsymbol{\Omega}_{\mathrm{CM}}]^{\mathrm{T}} \tag{6.41}$$

for M bodies. The rigid motion tensor for a particle α connected to a single body L is defined as

$$\boldsymbol{\Sigma}_{\alpha L} \coloneqq \begin{pmatrix} 1 & 0 & 0 & 0 & 0 & 0 \\ 0 & 1 & 0 & 0 & 0 & 0 \\ 0 & 0 & 1 & 0 & 0 & 0 \\ 0 & -r_{\alpha,3} & r_{\alpha,2} & 1 & 0 & 0 \\ r_{\alpha,3} & 0 & -r_{\alpha,1} & 0 & 1 & 0 \\ -r_{\alpha,2} & r_{\alpha,1} & 0 & 0 & 0 & 1 \end{pmatrix} . \tag{6.42}$$

Subscript numbers denote the spatial dimension coordinate and are with respect to the locater point $\boldsymbol{R}_{\mathrm{C}}$ for body L. The full rigid body motion tensor $\boldsymbol{\Sigma}$ is constructed by stacking the rigid motion tensors $\boldsymbol{\Sigma}_{\alpha L}$ for each particle α connected to body each body L as

$$\boldsymbol{\Sigma} \coloneqq \left(\begin{array}{cccc|ccc|c|ccc} \boldsymbol{\Sigma}_{11} & \boldsymbol{\Sigma}_{12} & \cdots & \boldsymbol{\Sigma}_{1\mathrm{N}_1} & 0 & 0 & \cdots & 0 & \cdots & 0 & 0 & \cdots & 0 \\ 0 & 0 & \cdots & 0 & \boldsymbol{\Sigma}_{2(\mathrm{N}_1+1)} & \boldsymbol{\Sigma}_{2(\mathrm{N}_1+2)} & \cdots & \boldsymbol{\Sigma}_{2(\mathrm{N}_1+\mathrm{N}_2)} & \cdots & 0 & 0 & \cdots & 0 \\ & & \vdots & & & & \vdots & & \vdots & 0 & 0 & \vdots & 0 \\ 0 & 0 & \cdots & 0 & 0 & 0 & \cdots & 0 & \cdots & \boldsymbol{\Sigma}_{\mathrm{M}(\mathrm{N}-\mathrm{N}_{\mathrm{M}}+1)} & \boldsymbol{\Sigma}_{\mathrm{M}(\mathrm{N}-\mathrm{N}_{\mathrm{M}}+2)} & \cdots & \boldsymbol{\Sigma}_{\mathrm{MN}} \end{array}\right) , \tag{6.43}$$

We now turn to Lagrange's equation of motion in order to determine the rigid body motion with generalized coordinates $\boldsymbol{\xi}$ as

$$\frac{d}{dt}\left(\frac{\partial \mathcal{L}}{\partial \dot{\boldsymbol{\xi}}}\right) - \frac{\partial \mathcal{L}}{\partial \boldsymbol{\xi}} = 0 . \tag{6.44}$$

Substituting the rigid body motion decomposition (Eq. (6.40)) into the total Lagrangian (Eq. (6.12)) results in the equation of motion of

$$\boldsymbol{\mathcal{M}}\,\ddot{\boldsymbol{\xi}} = \boldsymbol{F}^{\mathrm{C}} + \boldsymbol{F}^{\mathrm{I}} + \boldsymbol{F}^{\mathrm{C-I}} . \tag{6.45}$$

The generalized Lagrangian forces are separated into three distinct groups: locater kinematics (C), internal kinematics (I), and the coupling between the two (C – I)

$$\begin{aligned} F_i^{\mathrm{C}} &= \frac{1}{2}\,\dot{\xi}_j\,\frac{\partial}{\partial \xi_i}(\Sigma_{jl}\,M_{lm}\,\Sigma_{km})\,\dot{\xi}_k - \dot{\xi}_j\,\frac{\partial}{\partial \xi_n}(\Sigma_{jl}\,M_{lm}\,\Sigma_{im})\,\dot{\xi}_n \\ F_i^{\mathrm{I}} &= \frac{1}{2}\,\dot{r}_j\,\frac{\partial}{\partial \xi_i}(M_{jk})\,\dot{r}_k - \Sigma_{il}\,M_{lk}\,\dot{V}_k \\ F_i^{\mathrm{C-I}} &= \dot{\xi}_j\,\frac{\partial}{\partial \xi_i}(\Sigma_{jl}\,M_{lk})\,\dot{r}_k - \frac{\partial}{\partial \xi_n}(\Sigma_{il}\,M_{lk})\,\dot{r}_k\,\dot{\xi}_n \end{aligned} \tag{6.46}$$

with an effective mass matrix

$$\mathcal{M}_{ij} = \Sigma_{jl}\, M_{lm}\, \Sigma_{im} \ . \tag{6.47}$$

Evaluation of the partial derivatives in Eq. (6.46) follows from the chain rule and the derivation of the added mass tensor gradient discussed previously. We now have a mathematical framework for solving the equations of motion for a system of particles connected to rigid bodies with arbitrary kinematics.

References

1. Techet, A. Potential flow theory. *Lecture notes for the course* **2** (2005).
2. Batchelor, C. K. & Batchelor, G. *An introduction to fluid dynamics* (Cambridge University Press, 2000).
3. Yurkovetsky, Y. & Brady, J. F. Statistical mechanics of bubbly liquids. *Physics of Fluids* **8,** 881–895 (1996).
4. Lamb, H. *Hydrodynamics* (University Press, 1924).
5. Hinch, E. & Nitsche, L. C. Nonlinear drift interactions between fluctuating colloidal particles: oscillatory and stochastic motions. *Journal of Fluid Mechanics* **256,** 343–401 (1993).
6. Bonnecaze, R. & Brady, J. A method for determining the effective conductivity of dispersions of particles. *Proceedings of the Royal Society of London. Series A: Mathematical and Physical Sciences* **430,** 285–313 (1990).
7. Bonnecaze, R. & Brady, J. The effective conductivity of random suspensions of spherical particles. *Proceedings of the Royal Society of London. Series A: Mathematical and Physical Sciences* **432,** 445–465 (1991).
8. Goldstein, H., Poole, C. & Safko, J. *Classical mechanics* (American Association of Physics Teachers, 2002).
9. Minguzzi, E. Rayleigh's dissipation function at work. *European Journal of Physics* **36,** 035014 (2015).
10. d'Alembert, J. L. R. *Essai d'une nouvelle théorie de la résistance des fluides* (David l'Ainé, 1752).

Chapter 7

CONNECTION BETWEEN SWIMMING IN STOKES AND POTENTIAL FLOW

The well-known self-propulsion, or swimming, of a deformable body in Stokes flow (i.e., at low Reynolds number) can be understood and modeled from the variation in the configuration-dependent hydrodynamic resistance tensor throughout the period of deformation. Remarkably, at the other extreme of high Reynolds number, a deformable body may also self-propel without doing any net work on the fluid in potential flow. As a body deforms, the mass of fluid displaced—the so-called added mass—depends on the instantaneous body configuration, and a net displacement is possible over a period of deformation. This potential swimming takes a form identical to that for Stokes swimmers with the configuration-dependent added mass replacing the hydrodynamic resistance tensor. Analytical insight into the swimming of a deformable body is obtained through an expansion of the non-linear spatial dependence of the hydrodynamic interactions and connections between previous studies of swimming in Stokes flow to those in potential flow are made.

This chapter includes content from our previously published article:

1. Glisman, A. & Brady, J. F. Swimming in potential flow. *Journal of Fluid Mechanics* **962,** 11. `https://doi.org/10.1017/jfm.2022.946` (Nov. 2022).

7.1 Introduction

Self-propulsion is a vital element for life, from microscopic bacteria to large mammals. Swimming and flying organisms often deform their bodies to propel via hydrodynamic interactions with the surrounding fluid [1–4]. The essential fluid mechanics of propulsion varies between microscopic and macroscopic regimes as measured by the Reynolds number, $Re = \rho_f \, U \, L/\mu$, which quantifies the relative importance of inertial to viscous forces. The mass density ρ_f and viscosity μ of the fluid are material parameters, while the body's size and average swim speed set the characteristic length L and velocity U scales, respectively. Microorganisms self-propel at low Reynolds numbers, while larger bodies, such as birds and fish, self-propel at high Reynolds numbers [5].

The simplest model of fluid motion at large Reynolds numbers is potential flow, which approximates the flow field as irrotational and incompressible [6]. Irrotational flow cannot model the process of vortex shedding as a means of self-propulsion, which has often been considered an essential element [2, 7].

This raises the question: can a body self-propel in potential flow? The answer is yes, as first demonstrated by Saffman [1] (see also [8, 9]). The result is especially interesting, as the net motion occurs without dissipation and without the body doing net work on the fluid. Saffman argued that by breaking the natural time-reversal symmetry inherent in an irrotational flow, propulsion was generated from the configuration-dependent hydrodynamic (pressure) forces. [10] revealed a more general requirement of self-propulsion based on geometric arguments of the system phase space showing that the same principle holds in both flow regimes.

In this paper we explore the connection between these two regimes by presenting the equations of motion governing swimming in both Stokes and potential flow. The equations of motion for self-propulsion are derived for a general particle-based swimmer and then analyzed for a simple swimmer design called the collinear swimmer. We then "race" the swimmer in both flow regimes for small and large amplitude body deformations. It is analytically predicted—and numerically confirmed—that for the given swimmer design, the Stokes swimmer translates farther due to its longer ranged leading order hydrodynamic interactions. The analytical predictions for net translation at small oscillation are found to remain accurate even as the oscillation becomes large.

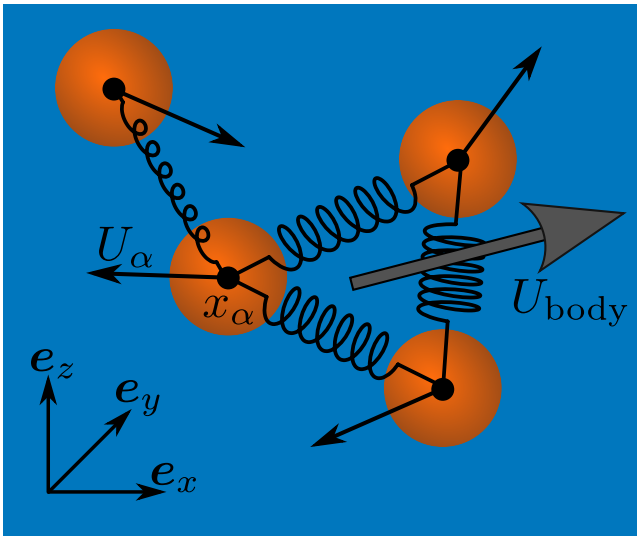

Figure 7.1: N spherical particles connected together to form a deformable body. Each particle α is parametrized by its position $\boldsymbol{x}_\alpha$ and velocity $\boldsymbol{U}_\alpha$. In general, the particle motion results in a net body velocity $\boldsymbol{U}_{\text{body}}$.

We conclude with a physically motivated discussion on how the results might be further generalized to study dissipative potential flows as well as understanding the role of hydrodynamic interactions in many swimmer systems.

7.2 Theory

To demonstrate the similarities between potential and Stokes flow, we first review then well-known theory and expressions for self-propulsion in Stokes flow [4, 11–13]. For convenience, we model the deformable body as a collection of N spherical particles connected together via non-hydrodynamic interparticle forces, e.g., springs, as illustrated in Figure 7.1. The force balance on particle α is

$$0 = -\sum_{\beta=1}^{N} \mathbf{R}_{\alpha\beta} \cdot \boldsymbol{U}_\beta + \boldsymbol{F}_\alpha^C \,, \tag{7.1}$$

where $\boldsymbol{U}_\beta$ is the translational velocity of particle β, $\mathbf{R}_{\alpha\beta}(\{\boldsymbol{X}\})$ is the configuration-dependent hydrodynamic resistance tensor that couples force to velocity and $\boldsymbol{F}_\alpha^C$ is the interparticle connector force. Here, $\{\boldsymbol{X}\} = (\boldsymbol{x}_1, \ldots, \boldsymbol{x}_N)$ denotes the configuration of all N particles. To most clearly illustrate the behavior, we consider only translational motion and forces.

Self-propulsion is a force-free motion: there is no external force and the sum over all particles of the internal connector forces is zero, $\sum_\alpha \boldsymbol{F}^C_\alpha = 0$, thus

$$0 = -\sum_{\alpha,\beta=1}^{N} \mathbf{R}_{\alpha\beta} \cdot \boldsymbol{U}_\beta \,. \tag{7.2}$$

Selection of the spatial origin is arbitrary, and so we choose particle 1 for convenience as the body locator point and refer all motion relative to it. Alternatively, one could use the center of mass or center of resistance. We define a new set of relative coordinates and translational velocities

$$\boldsymbol{r}_\alpha = \boldsymbol{x}_\alpha - \boldsymbol{x}_1 \quad , \quad \boldsymbol{V}_\alpha = \boldsymbol{U}_\alpha - \boldsymbol{U}_1 \,, \tag{7.3}$$

and the total force balance becomes

$$0 = -\mathbf{R}_{\text{body}} \cdot \boldsymbol{U}_1 - \sum_{\alpha,\beta=1}^{N} \mathbf{R}_{\alpha\beta} \cdot \boldsymbol{V}_\beta \,, \tag{7.4}$$

where the resistance tensor of the entire body is $\mathbf{R}_{\text{body}} = \sum_{\alpha,\beta=1}^{N} \mathbf{R}_{\alpha\beta}$. The translation of the body follows as

$$\boldsymbol{U}_1 = -\mathbf{R}^{-1}_{\text{body}} \cdot \sum_{\alpha,\beta=1}^{N} \mathbf{R}_{\alpha\beta} \cdot \boldsymbol{V}_\beta \,. \tag{7.5}$$

Since the absolute position in space for an isolated body does not matter, the resistance tensors are functions of the relative coordinates $\{\boldsymbol{r}_\alpha\}$ only.

We are interested in *sustained* motion of the body as it executes periodic deformation with period T. The net displacement of the body in one period is

$$\Delta\boldsymbol{x}_1 = -\int_0^T \mathbf{R}^{-1}_{\text{body}}(t) \cdot \sum_{\alpha,\beta=1}^{N} \mathbf{R}_{\alpha\beta}(t) \cdot \boldsymbol{V}_\beta(t)\, dt \,, \tag{7.6}$$

where we emphasize that both the relative velocities $\boldsymbol{V}_\beta(t)$ and the resistance tensors are functions of time, the latter through the changing configuration $\{\boldsymbol{r}_\alpha(t)\}$. Since the articulation velocities $\boldsymbol{V}_\beta(t)$ are periodic in time, there will only be net displacement if the body configuration resistance tensors also change in time. This can be made more transparent by noting that $\boldsymbol{V}_\beta = d\boldsymbol{r}_\beta/dt = \dot{\boldsymbol{r}}_\beta$ and integrating (7.6) by parts

$$\Delta\boldsymbol{x}_1 = \int_0^T \sum_{\alpha,\beta,\gamma} \nabla_{\boldsymbol{r}_\gamma} \cdot \left(\mathbf{R}^{-1}_{\text{body}} \cdot\ \mathbf{R}_{\alpha\beta}\right) : \boldsymbol{r}_\beta \dot{\boldsymbol{r}}_\gamma \, dt \,, \tag{7.7}$$

showing that it is *necessary* for the resistance tensors to change with the internal configuration of the body to achieve net motion.

Turning now to potential flow, the absence of vorticity allows the fluid velocity $\boldsymbol{u}$ to be determined from the velocity potential $\boldsymbol{u} = \nabla\phi$, which satisfies Laplace's equation $\nabla^2\phi = 0$ subject to no flux conditions on the particle surfaces $\boldsymbol{n}\cdot\nabla\phi = \boldsymbol{n}\cdot\boldsymbol{U}_\alpha$. The kinetic energy of the fluid $\mathcal{T}^{\mathrm{f}} = \frac{1}{2}\rho_{\mathrm{f}}\int \boldsymbol{u}\cdot\boldsymbol{u}dV$ can be written in terms of the velocity potential and use of the divergence theorem gives

$$\mathcal{T}^{\mathrm{f}} = \frac{1}{2}\sum_{\alpha,\beta}\boldsymbol{U}_\alpha\cdot\tilde{\mathsf{M}}_{\alpha\beta}(\{\boldsymbol{X}\})\cdot\boldsymbol{U}_\beta\,, \tag{7.8}$$

where the configuration-dependent $\tilde{\mathsf{M}}_{\alpha\beta}$ is known as the added mass. For example, the added mass of an isolated spherical particle is $\frac{1}{2}\rho_{\mathrm{f}}V$, where V is the volume of the particle, and expresses the fact that a certain amount of fluid must be set into motion as the particle accelerates [6]. How much fluid needs to be accelerated depends on the relative configuration of all N particles. To obtain the total kinetic energy $\mathcal{T}$ of the system, we add the kinetic energy of the individual particles $\frac{1}{2}m_\alpha U_\alpha^2$ to the that of the fluid

$$\mathcal{T} = \frac{1}{2}\sum_{\alpha,\beta}\boldsymbol{U}_\alpha\cdot\mathsf{M}_{\alpha\beta}(\{\boldsymbol{X}\})\cdot\boldsymbol{U}_\beta \quad , \quad \mathsf{M}_{\alpha\beta}(\{\boldsymbol{X}\}) = \tilde{\mathsf{M}}_{\alpha\beta}(\{\boldsymbol{X}\}) + m_\alpha\boldsymbol{I}_{\alpha\beta}, \tag{7.9}$$

where $\boldsymbol{I}_{\alpha\beta}$ is the identity tensor.

The equations of motion for particles in potential flow follow from Lagrangian mechanics, where the Lagrangian is the difference between the kinetic and potential energies $\mathcal{L} = \mathcal{T} - \mathcal{V}$. For particle α

$$\frac{d}{dt}\frac{\partial\mathcal{L}}{\partial\boldsymbol{U}_\alpha} - \frac{\partial\mathcal{L}}{\partial\boldsymbol{x}_\alpha} = \boldsymbol{F}_\alpha^C\,, \tag{7.10}$$

where we have not assumed that the connector forces are derivable from a potential (although they may be). We have assumed that the flow field is inviscid, such that viscous forces are negligible, but this assumption can be relaxed (see §7.5). The kinetic energy term on the LHS of (7.10) can be shown to give the net pressure force integrated over the body [6]. From the Lagrangian, the generalized momentum of particle α is

$$\boldsymbol{P}_\alpha = \sum_{\beta=1}^{N}\mathsf{M}_{\alpha\beta}\cdot\boldsymbol{U}_\beta\,, \tag{7.11}$$

and $d\boldsymbol{P}_\alpha/dt$ gives the LHS of (7.10) (without the potential $\mathcal{V}$). The generalized momentum accounts for both the intrinsic momentum of the particle and the added momentum resulting from the motion of the fluid.

The total momentum of the body (and fluid) composed of N particles is the sum over the individual generalized momenta: $\boldsymbol{P}_{\text{body}} = \sum_\alpha \boldsymbol{P}_\alpha$, and since the internal connector forces sum to zero, we have $d\boldsymbol{P}_{\text{body}}/dt = 0$ or

$$\boldsymbol{P}_{\text{body}} = \sum_{\alpha,\beta=1}^{N} \mathsf{M}_{\alpha\beta} \cdot \boldsymbol{U}_\beta = \boldsymbol{C}\,, \tag{7.12}$$

where $\boldsymbol{C}$ is a constant vector. Our interest is in motion due to the deformation of the body, and therefore we set any constant momentum to zero. From (7.12) it is easy to see that if we define the relative coordinates and velocities as in (7.3) then the net displacement in one period is *identical* to (7.6) for Stokes flow with the resistance tensor replaced by the added mass matrix:

$$\Delta\boldsymbol{x}_1 = -\int_0^T \mathsf{M}^{-1}_{\text{body}}(t) \cdot \sum_{\alpha,\beta=1}^{N} \mathsf{M}_{\alpha\beta}(t) \cdot \boldsymbol{V}_\beta(t)\, dt\,, \tag{7.13}$$

where, as before, the body's added mass is $\mathsf{M}_{\text{body}} = \sum_{\alpha,\beta=1}^{N} \mathsf{M}_{\alpha\beta}$. The integration by parts (7.7) also follows by simple replacement.

Thus, as first shown by Chambrion *et al.* [10], we see that self-propulsion in potential flow takes a form *identical* to that for Stokes flow with the added mass matrix replacing the resistance matrix. This equivalence follows directly from the zero net force balance and the fact that the viscous hydrodynamic force in Stokes flow and the linear momentum in potential flow are linear in the particle velocities. While the structure is the same, this does not mean the net displacement is the same in the two flows, as the magnitude and form of the interactions, and thus the values of the components of resistance and added mass matrices, are different.

The forms of the net motion given above apply for any "gate" of the swimmer, i.e., any $\boldsymbol{V}_\beta(t)$. The details of how the body articulates its component parts are not needed. A swimmer can have a fixed gate and then the internal forces $\boldsymbol{F}^C$ necessary to achieve that gate can be found from the individual force balances once the locator point motion is known. Alternatively, the activation of the internal forces could be prescribed and then the articulation

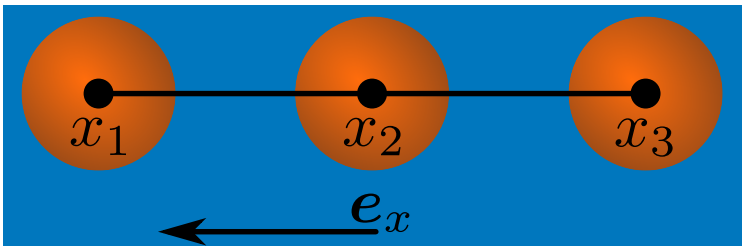

Figure 7.2: Three spheres of equal radii a are connected by thin arms with prescribed kinematics. The swimmer is collinear and translates along one spatial dimension.

and net displacement of the body can be found. It is also possible to have more complex dynamics in terms of control functions or swimming with a fixed power consumption. They each follow the above analysis.

7.3 Collinear Swimmer

As an illustration of swimming in potential flow and how it compares to that in Stokes flow, we consider the prototypical Stokes swimmer design analogous to that of Najafi & Golestanian [3], which distills the hydrodynamic mechanism of self-propulsion into a minimal model. The swimmer consists of three identical spheres connected via two "arms" (Figure 7.2). The arms are thin, such that we can neglect them hydrodynamically. The body is collinear and its locater point and kinematic constraints are relative to the central particle 2, such that

$$\boldsymbol{r}_1 = \left(\bar{R} + \frac{U_0}{\omega}\sin\left(\omega\, t\right)\right)\boldsymbol{e}_x \ , \quad \text{and} \quad \boldsymbol{r}_3 = -\left(\bar{R} + \frac{U_0}{\omega}\sin\left(\omega\, t + \delta\right)\right)\boldsymbol{e}_x \ . \tag{7.14}$$

The constrained particles oscillate with amplitude U_0/ω, frequency ω, and phase shift δ. The time-averaged moment arm $\bar{R}$ over the articulation period is identical for both oscillators. One may alter the constraints' functional form and the discussion will not change significantly. The key aspects are that the motion is periodic and there is an out-of-phase component between at least two degrees of freedom.

The body is initially collinear along the x-axis, and all articulation occurs along this axis. By symmetry the swimmer will remain along this axis for all time and the spatial degrees of freedom are reduced to one. For potential flow, we have set the particle densities equal to that of the fluid $\rho_\mathrm{p} = \rho_\mathrm{f}$. To gain further analytical insight into the structure of self-propulsion, we calculate the leading order Taylor expansion of the body equations of motions in both flow

regimes (Eqs. (7.6), (7.13)). The expansion accuracy is captured by the small parameter $\varepsilon = (U_0/\omega)/\bar{R}$, which is the ratio of the oscillation amplitude to the time-averaged interparticle separation. In this limit, the hydrodynamic interactions during the articulation are well-approximated by their values at the time-averaged separation, and the leading order results for Stokes and potential flow are

$$\Delta x_2 = 2\,\pi \sin\delta \left(\frac{U_0}{\omega}\right)^2 \left.\frac{\partial \mathcal{R}_{B3}}{\partial r_3}\right|_{r_1=\bar{R},r_3=-\bar{R}} \tag{7.15}$$

and

$$\Delta x_2 = 2\,\pi \sin\delta \left(\frac{U_0}{\omega}\right)^2 \left.\frac{\partial \mathcal{M}_{B3}}{\partial r_3}\right|_{r_1=\bar{R},r_3=-\bar{R}}\,, \tag{7.16}$$

respectively. The subscript B reflects that the quantities contain information about the body's overall configuration. The effective resistance tensor is given as $\mathcal{R}_{B3} = R_{\text{body}}^{-1} \sum_{\alpha=1}^{3} R_{\alpha 3}$, while the effective mass tensor $\mathcal{M}_{B3}$ is identical in form with R replaced by $\tilde{\mathcal{M}}$. Detailed calculation of specific tensor elements can be found in Durlofsky *et al.* [14] for Stokes flow and Yurkovetsky & Brady [15] for potential flow. The leading order effective mass matrix is given as

$$\mathcal{M}_{B3} = \frac{3 - 2\left(\frac{1}{r_{23}^3} - \frac{1}{r_{13}^3}\right)}{9 - 4\left(\frac{1}{r_{13}^3} - \frac{1}{r_{23}^3} - \frac{1}{r_{12}^3}\right)}\,, \tag{7.17}$$

where r_{ij} is the distance between particles i and j. The effective resistance matrix was evaluated numerically using Stokesian dynamics without lubrication forces.

The Stokes swimmer translates farther after an articulation period when the particles are well-separated, as seen in Fig. 7.3a. This behavior arises from the stronger hydrodynamic interactions in Stokes flow at large separations. From (7.7) self-propulsion scales with the gradient of the configuration-dependent hydrodynamic tensors. A translating sphere in Stokes flow creates a monopolar disturbance [14], giving a leading order net translation scaling of $O(\bar{R}^{-2})$. In potential flow, the longest ranged hydrodynamic interaction scales as a dipolar gradient [15], which gives an $O(\bar{R}^{-4})$ scaling for net translation. Full numerical simulation of the equations of motion (Eqs. (7.7), (7.13)) matches the analytical predictions very well. At narrow separations, the higher-order moments accounted for in Stokesian dynamics dominate and reduce the net translation [14]. Simulations and analysis did not account for the singular Stokes flow lubrication forces at narrow separation.

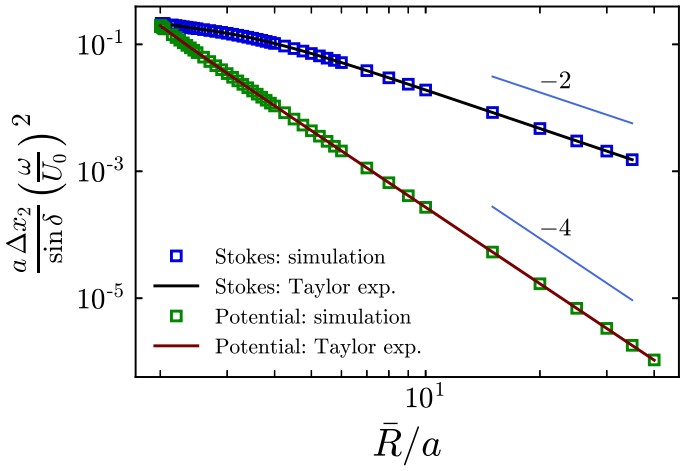

(a)

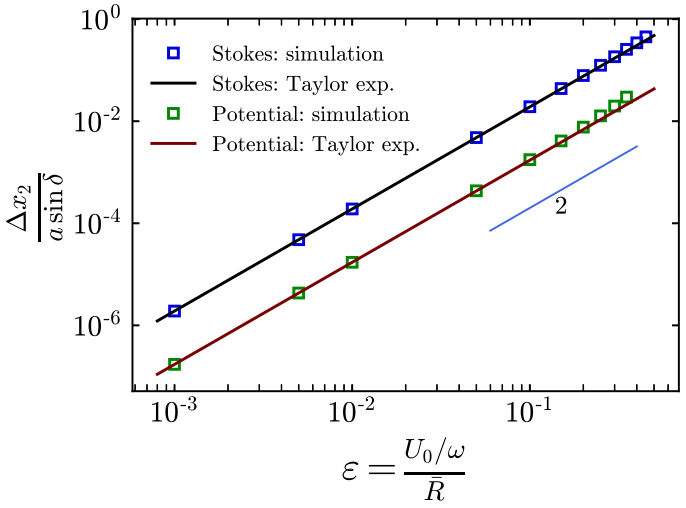

(b)

Figure 7.3: The self-propulsion of the collinear swimmer after one period of articulation. Particles were neutrally buoyant, and simulated with phase angle $\delta = \pi/2$. Self-propulsion is inversely proportional to the average inter-particle spacing (a) with $U_0/(a\omega) = 0.01$ and proportional to relative dimensionless oscillation (b).

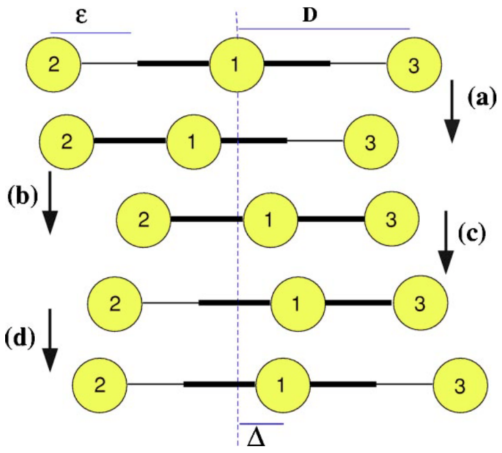

Figure 7.4: Golestanian swimmer articulation over one period. The articulating particles (2 and 3) are initially extended. In steps (a)–(b), a single particle contracts. The particles extend in the same order they contracted during steps (c)–(d), breaking time-reversal symmetry. Both particles have identical oscillation amplitudes, just as the collinear swimmer. Najafi & Golestanian define the oscillation amplitude ε, which is U_0/ω for the collinear swimmer. Analogously, $\mathrm{D} = \bar{R} + U_0/\omega$ and Δ is the net translation after one period. Figure from Najafi & Golestanian [3, Fig. 2].

When the amplitude of articulation ε grows, the Taylor expansion is less accurate as the particles become closer at minimum separation. The inverse power-law scaling of the hydrodynamic interactions causes the closer interactions to overcompensate for the weaker interactions when the particles are at maximum separation and lead to a non-linear increase in displacement after one period. This results in a deviation between the analytic and numeric results for large amplitude in Figure 7.3b. Nevertheless, the $O(\varepsilon^2)$ scaling of the amplitude of self-propulsion holds even as the oscillation amplitude becomes large compared to average separation and the particles nearly overlap. Note that $\varepsilon \leq \frac{1}{2}$ to prevent particle overlap.

7.4 Comparison to Golestanian Swimmer

We also compare the collinear swimmer to the Golestanian swimmer [3], which is a three-particle swimmer that also breaks time-reversal symmetry. By analyzing different articulation patterns, we can better understand how different swimmer designs affect swimming performance.

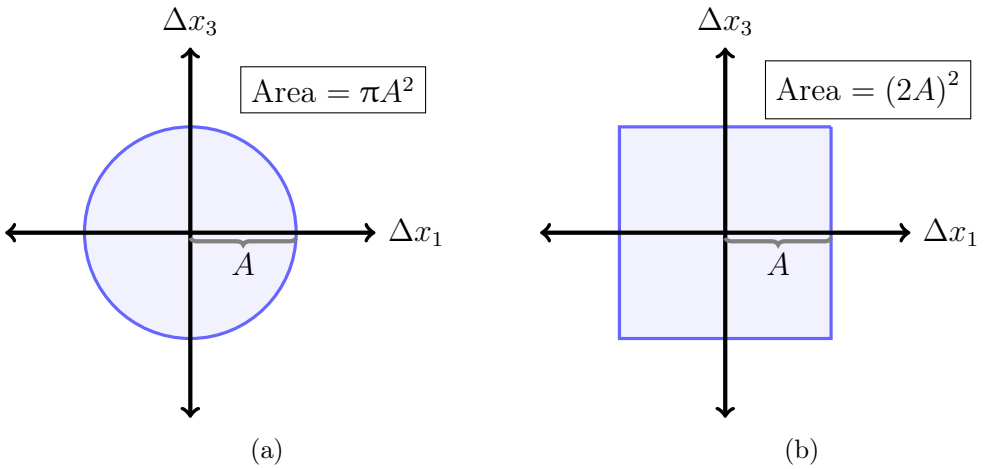

Figure 7.5: Phase space schematic for the internal degrees of freedom of the collinear swimmer (a) and Golestanian swimmer (b). Articulation (positional) amplitudes for all degrees of freedom are identical for ease of comparison.

Najafi & Golestanian [3] proposed a similar three-sphere, collinear swimmer model in the Stokes flow regime (Fig. 7.4). The kinematic constraints are separated into four discrete steps, rather than a continuous oscillation. In each step, one of the outer particles articulates at a constant velocity, and the other particle remains stationary with respect to the locater point (i.e., $\dot{r}_1 = U_0 \;\; \dot{r}_3 = 0$ in the notation of the collinear swimmer).

The swimmer begins in an equispaced configuration, extending both particles to their maximum articulation length. During the first two steps, one articulating particle contracts at a time to the same contracted length. The pairs then extend to their original length over the last two steps in the same order they contracted. The overall articulation is non-reciprocal and therefore self-propels via breaking time-reversal symmetry. Najafi & Golestanian similarly predicted a quadratic self-propulsion Δx_2 scaling with the relative oscillation amplitude ϵ for their three-link swimmer.

Golestanian & Ajdari [16] later proved that the magnitude of net translation for their swimmer designs was directly proportional to the area traced over a cycle in configuration phase space. The degrees of freedom in phase space are the internal degrees of freedom, which are the lengths of the articulating arms for the swimmers we present in this work. The two swimmer designs trace out different shapes in configuration phase space and allows us to compare the expected net translation of both models analytically (Fig. 7.5).

The Golestanian swimmer deforms a single particle at a time, thereby tracing out a square over the articulation period (assuming the pairs deform identical lengths). The collinear swimmer traces out an ellipse in general as both particles deform continuously. If the phase difference is an integer multiple of π, the ellipse collapses to a line, which encloses zero area and predicts no net translation. Conversely, when the phase difference is maximized at $\delta = \pi/2$, the ellipse becomes a circle with the maximum enclosed area.

As the swimming structure is identical in the Stokes and potential regimes, we predict that the ratio of net translations for swimmers in the potential regime is the same as that of areas traced out in configuration phase space. The ratio of the area enclosed for the Golestanian swimmer to the collinear swimmer is

$$\frac{\Delta\, x_{2,\,\text{collinear}}}{\Delta\, x_{2,\,\text{Golestanian}}} = \frac{\text{Area collinear}}{\text{Area Golestanian}} = \frac{\pi A^2}{(2A)^2} = \frac{\pi}{4}\,, \tag{7.18}$$

for identical oscillation amplitudes A. Full numerical simulations of the equations of motion recover this ratio for small relative oscillation amplitudes ε in both flow regimes (Fig. 7.6). As expected, the net translation ratio shrinks as ε grows. The phase space argument assumes that the hydrodynamic interactions are equivalent throughout the articulation period such that the net translation is governed by the integral of articulation amplitudes. As the oscillation amplitude grows, the hydrodynamic interactions at average separation become a worse approximation over the articulation period due to their non-linear character. The longer-ranged Stokes flow interactions are more accurately represented by the hydrodynamic interactions at average separation, which explains the better agreement between the two flow regimes for larger ε.

The phase space argument for net translation is powerful, as it makes a comparison between alternative swimmer designs easy for small amplitude oscillations. This allows for more rapid prototyping of swimmer models as all one must know is the shape enclosed in configuration space. The swimmer can then be optimized with respect to a desired quantity, such as net translation, quite easily. The Golestanian swimmer is the most "efficient" one-dimensional swimmer design as a square encloses the most area for a given oscillation amplitude (edge length).

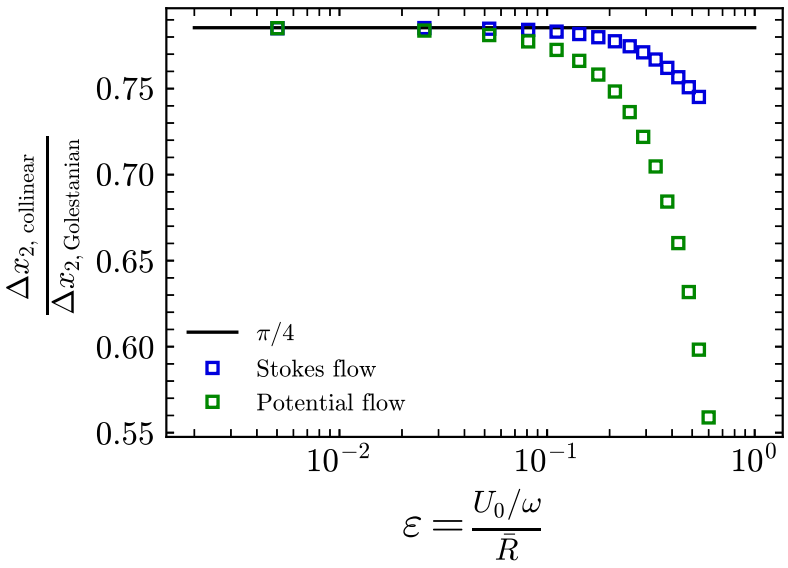

Figure 7.6: The ratio of net translation of collinear to Golestanian swimmer after one period of articulation for varying relative oscillation amplitude ε. Data asymptotes to the expected value of $\pi/4$ as $\epsilon \to 0$, as predicted by Golestanian & Ajdari [16].

7.5 Discussion

Self-propulsion in Stokes and potential flow follow an identical structure where time-reversal symmetry is broken through configuration-dependent hydrodynamics, in accord with prior studies [1, 9, 10, 16, 17]. In potential flow, the kinetic energy is a quadratic function of the velocities, $\mathcal{T} = \frac{1}{2}\boldsymbol{U} \cdot \tilde{\mathsf{M}}(\{\boldsymbol{X}\}) \cdot \boldsymbol{U}$, from which it follows that the generalized momentum $\boldsymbol{P} = \partial\mathcal{T}/\partial\boldsymbol{U}$ is linear in the velocities. Stokes flow can be cast into the same form with the Rayleigh dissipation function replacing the kinetic energy: $\dot{\Phi} = \frac{1}{2}\boldsymbol{U} \cdot \mathbf{R}(\{\boldsymbol{X}\}) \cdot \boldsymbol{U}$, and the viscous hydrodynamic forces are given by $\boldsymbol{F}^{\text{vis}} = -\partial\dot{\Phi}/\partial\boldsymbol{U}$. The quadratic forms show that the mass and resistance tensors are symmetric and positive definite.

It is also possible to combine the two approaches and add the viscous forces to the RHS of (7.10) to allow a continuous transition as the Reynolds number increases between self-propulsion in Stokes flow to that in potential flow. Such an approach neglects the non-linear convection of vorticity, of course, but it may provide a simple way to model the transition between the two regimes. In fact, potential flow can itself generate viscous forces which can be found from the point-wise energy dissipation $\dot{\Phi} = \mu \int \boldsymbol{e} : \boldsymbol{e} dV = \mu \int |\nabla\nabla\phi|^2 dV$, where $\boldsymbol{e}$

is the velocity gradient tensor and the integration is over the fluid volume. A translating sphere in potential flow experiences a viscous drag force of $\boldsymbol{F}^{\text{vis}} = -12\pi\mu a\boldsymbol{U}$, which is twice that in Stokes flow. It would be interesting to see what insight this combined approach can give to self-propulsion at finite Reynolds numbers.

Despite the geometric similarity, it is still surprising that self-propulsion is possible in potential flow where the motion is fully conservative and the deforming body does no net work on the fluid after each period of articulation. At the end of one period the body shape and the kinetic (and potential) energies return to their original values, but the body has achieved a net displacement. Furthermore, when the body stops deforming, all motion in the fluid ceases instantaneously—there is no time in Laplace's equation—just as it does in Stokes flow.

The three-sphere collinear swimmer was chosen to illustrate the essential features of self-propulsion and shows that the potential swimmer is "slower" due to the stronger hydrodynamic interactions in Stokes flow. A perhaps even simpler system is to have just two spherical particles, but now allow the radius of one (or both) particles grow and shrink in time. The separation between the two spheres can be varied in such a way so that the hydrodynamics on inflation differs from that upon deflation which will lead to net motion, as shown by Avron *et al.* [18]. In this case, both the Stokes and potential flow disturbances decay as one over separation, and it is not obvious which swimmer is faster, or if this type of deformation can lead to faster translation in general.

We modeled the self-propelling body as a collection of spherical particles, but this was done for simplicity. The individual particles can be of any size, shape and distribution. In the limit where the articulating particles are all small and located along the surface of the body we can achieve a body with surface activation, which is called a squirmer in the Stokes regime. Squirmers have proved to be a simple model and a work horse for the study of active matter systems at low Reynolds number [4, 19–21]. Indeed, the so-called "neutral" Stokes squirmer, like a classical phoretic particle, generates a potential-dipole flow field (it has no stresslet); although technically the fluid satisfies the no-slip condition at the particle surface rather than the no-flux condition of potential flow, but that may be just a detail in relating the strength of the potential flow to the nature of the body deformation.

We discussed a single articulating body in this work, but it should be clear from the general formulation that there is no restriction on the number of self-propelled bodies. The study of many interacting self-propelled bodies has become a very vibrant area of research in the active matter community [22–26]. Active Stokes flow swimmers form the basis of the Active Brownian particle (ABP) model for active matter, which has been shown to display very interesting collective dynamics such as motility-induced phase separation (MIPS) and coherent flocking motion. It would be interesting to see if potential swimmers can also display similar collective motion. Two bodies translating parallel to each other may attract due to the Bernoulli effect—to conserve mass the fluid velocity between the two bodies is faster than on the outside—leading to a reduced pressure there and an attractive force. Two bodies moving towards each other along their line of centers will experience a repulsive force as there is a stagnation point between the two bodies and a larger pressure. This simple observation may point to a fluid mechanical origin for flocking structure.

Modeling the fluid motion as potential flow is, of course, a very bold approximation, but it may help give insight into behavior in situations in which the vorticity is confined to thin regions. This occurs for small amplitude oscillations (see squirmers above) where the vorticity is confined to the body surface, and for streamlined bodies where the vorticity is confined to a thin wake. Outside these thin regions of vorticity the fluid motion at high Reynolds numbers can be modeled as inviscid potential flow [27]. If two bodies are swimming side-by-side, when one body changes its speeds or direction, the second body will sense this change via the the potential-flow interactions before vorticity has time to evolve. Thus, potential flow might prove to be a fruitful starting point.

As a final note, since potential flow is conservative, the system has a Hamiltonian and therefore can have a well-defined statistical mechanics and thermodynamics. This was shown to be the case for bubbly liquids by Yurkovetsky & Brady [15], and used to predict an actual phase transition in a bubbly flow. The study of swimmers in potential flow has a well-founded and developed mechanics and may offer insight into the beautiful and striking collective behavior often observed in the natural world.

7.6 Appendix: Force and Torque Balance

Here we extend the treatment to include rotary motion of the particles and the body along with the associated torque and angular momentum balances. We group the force ($\boldsymbol{F}$) and torque ($\boldsymbol{L}$) on particle α into a single vector $\mathcal{F}_\alpha = (\boldsymbol{F}_\alpha, \boldsymbol{L}_\alpha)$, and likewise for the translational and rotational velocities $\mathcal{U}_\alpha = (\boldsymbol{U}_\alpha, \boldsymbol{\Omega}_\alpha)$, where the angular velocity $\boldsymbol{\Omega}_\alpha$ is about the center of particle α. In Stokes flow, the viscous hydrodynamic drag force/torque on particle α is

$$\mathcal{F}_\alpha^{\text{vis}} = -\mathcal{R}_{\alpha\beta} \cdot \mathcal{U}_\beta \,, \tag{7.19}$$

with an implied sum over all particles β and the "grand" resistance matrix $\mathcal{R}_{\alpha\beta}$ is a function of the positions and orientations of all N particles.

Denoting the translational and rotational velocity of the body by $\mathcal{U}_B = (\boldsymbol{U}_B, \boldsymbol{\Omega}_B)$, and following Swan *et al.* [4] we define the relative velocities $\mathcal{V}_\beta$ of each particle by

$$\mathcal{U}_\beta = \boldsymbol{\Sigma}^T \cdot \mathcal{U}_B + \mathcal{V}_\beta \,, \tag{7.20}$$

where the tensor $\boldsymbol{\Sigma}$ is composed of 6×6 sub-matrices connecting the body locator point B to each particle of the form

$$\boldsymbol{\Sigma}_{B\alpha} = \begin{pmatrix} 1 & 0 & 0 & 0 & 0 & 0 \\ 0 & 1 & 0 & 0 & 0 & 0 \\ 0 & 0 & 1 & 0 & 0 & 0 \\ 0 & \Delta r_3^{\alpha B} & -\Delta r_2^{\alpha B} & 1 & 0 & 0 \\ -\Delta r_3^{\alpha B} & 0 & \Delta r_1^{\alpha B} & 0 & 1 & 0 \\ \Delta r_2^{\alpha B} & -\Delta r_1^{\alpha B} & 0 & 0 & 0 & 1 \end{pmatrix} , \tag{7.21}$$

where $\Delta \boldsymbol{r}^{\alpha B} = \boldsymbol{x}_\alpha - \boldsymbol{x}_B$. These sub-matrices connecting each of the N particles to the locator point are assembled into the rigid body connectivity matrix $\boldsymbol{\Sigma}$.

The connectivity matrix $\boldsymbol{\Sigma}$ sums the forces and torques on all the particles, and since the net internal forces and torques are zero, $\boldsymbol{\Sigma} \cdot \mathcal{F}^C = 0$, summing (7.19) along with the relative velocities (7.20) gives the motion of the body in Stokes flow

$$\mathcal{U}_B^{Stokes} = -\left(\boldsymbol{\Sigma} \cdot \mathcal{R} \cdot \boldsymbol{\Sigma}^T\right)^{-1} \cdot \boldsymbol{\Sigma} \cdot \mathcal{R} \cdot \mathcal{V} \,, \tag{7.22}$$

where we have suppressed the subscripts and the implied sum is over all particles. Eq. (7.22) is the generalization of (7.5) to include the torque balance. The form is the same and therefore the net displacement over a period follows by integration in time.

In potential flow the total kinetic energy of the N particle system including the angular velocities has the quadratic form $\mathcal{T} = \frac{1}{2}\sum_{\alpha\beta}\mathcal{U}_\alpha \cdot \tilde{\mathcal{M}}_{\alpha\beta} \cdot \mathcal{U}_\beta$, where the added mass matrix now also contains the individual particles' moments of inertia. The generalized momentum (linear and angular) of particle α is $\mathcal{P}_\alpha = \sum_\beta \tilde{\mathcal{M}}_{\alpha\beta} \cdot \mathcal{U}_\beta$. The total linear and angular momentum is a constant, which we take to be zero, and using $\mathbf{\Sigma}$ and the relative velocities we have (7.22), but with the added mass matrix replacing the grand resistance matrix for potential flow

$$\mathcal{U}_B^{Potential} = -\left(\mathbf{\Sigma} \cdot \tilde{\mathcal{M}} \cdot \mathbf{\Sigma}^T\right)^{-1} \cdot \mathbf{\Sigma} \cdot \tilde{\mathcal{M}} \cdot \mathcal{V}\,; \tag{7.23}$$

integration over a period, gives the analog of (7.13).

References

1. Saffman, P. The self-propulsion of a deformable body in a perfect fluid. *Journal of Fluid Mechanics* **28,** 385–389 (1967).
2. Lighthill, S. J. *Mathematical biofluiddynamics* (SIAM, 1975).
3. Najafi, A. & Golestanian, R. Simple swimmer at low Reynolds number: Three linked spheres. *Physical Review E* **69,** 062901 (2004).
4. Swan, J. W., Brady, J. F., Moore, R. S. & ChE 174. Modeling hydrodynamic self-propulsion with Stokesian Dynamics. Or teaching Stokesian Dynamics to swim. *Physics of Fluids* **23,** 071901 (2011).
5. Klotsa, D. As above, so below, and also in between: Mesoscale active matter in fluids. *Soft Matter* **15,** 8946–8950 (2019).
6. Lamb, H. *Hydrodynamics* (University Press, 1924).
7. Wu, T., Brokaw, C. J. & Brennen, C. *Swimming and flying in nature* (Springer, 1975).
8. Wu, T. Hydromechanics of swimming propulsion. Part 1. Swimming of a two-dimensional flexible plate at variable forward speeds in an inviscid fluid. *Journal of Fluid Mechanics* **46,** 337–355 (1971).
9. Kanso, E., Marsden, J. E., Rowley, C. W. & Melli-Huber, J. B. Locomotion of articulated bodies in a perfect fluid. *Journal of Nonlinear Science* **15,** 255–289 (2005).
10. Chambrion, T., Giraldi, L. & Munnier, A. Optimal strokes for driftless swimmers: A general geometric approach. *ESAIM: Control, Optimisation and Calculus of Variations* **25,** 6 (2019).
11. Stone, H. A. & Samuel, A. D. Propulsion of microorganisms by surface distortions. *Physical Review Letters* **77,** 4102 (1996).
12. Lauga, E. & Powers, T. R. The hydrodynamics of swimming microorganisms. *Reports on Progress in Physics* **72,** 096601 (2009).
13. Masoud, H. & Stone, H. A. The reciprocal theorem in fluid dynamics and transport phenomena. *Journal of Fluid Mechanics* **879** (2019).
14. Durlofsky, L., Brady, J. F. & Bossis, G. Dynamic simulation of hydrodynamically interacting particles. *Journal of Fluid Mechanics* **180,** 21–49 (1987).
15. Yurkovetsky, Y. & Brady, J. F. Statistical mechanics of bubbly liquids. *Physics of Fluids* **8,** 881–895 (1996).
16. Golestanian, R. & Ajdari, A. Analytic results for the three-sphere swimmer at low Reynolds number. *Physical Review E* **77,** 036308 (2008).

17. Purcell, E. M. Life at low Reynolds number. *American Journal of Physics* **45,** 3–11 (1977).

18. Avron, J., Kenneth, O. & Oaknin, D. Pushmepullyou: An efficient micro-swimmer. *New Journal of Physics* **7,** 234 (2005).

19. Lighthill, M. On the squirming motion of nearly spherical deformable bodies through liquids at very small Reynolds numbers. *Communications on Pure and Applied Mathematics* **5,** 109–118 (1952).

20. Theers, M., Westphal, E., Qi, K., Winkler, R. G. & Gompper, G. Clustering of microswimmers: interplay of shape and hydrodynamics. *Soft Matter* **14,** 8590–8603 (2018).

21. Datt, C. & Elfring, G. J. Active particles in viscosity gradients. *Physical Review Letters* **123,** 158006 (2019).

22. Pooley, C., Alexander, G. & Yeomans, J. Hydrodynamic interaction between two swimmers at low Reynolds number. *Physical Review Letters* **99,** 228103 (2007).

23. Lauga, E. & Bartolo, D. No many-scallop theorem: Collective locomotion of reciprocal swimmers. *Physical Review E* **78,** 030901 (2008).

24. Cates, M. E. & Tailleur, J. Motility-induced phase separation. *Annual Review of Condensed Matter Physics* **6,** 219–244 (2015).

25. Dulaney, A. R. & Brady, J. F. Machine learning for phase behavior in active matter systems. *Soft Matter* **17,** 6808–6816 (2021).

26. Mallory, S. A., Omar, A. K. & Brady, J. F. Dynamic overlap concentration scale of active colloids. *Physical Review E* **104,** 044612 (2021).

27. Saffman, P. *Vortex Dynamics* (Cambridge University Press, 1992).